MONITEQ

STARTRACKER FINAL REPORT

DOC CONTRACTOR REPORT - DOC-CR-SP-83-015

The evaluation of charge transfer device (CTD) technology and the development of a conceptual design for a CTD-based spacecraft stellar sensor

MONITEQ

Monitoring Environmental Quality
Moniteq Ltd., 630 Rivermede Road, Concord, Ontario, Canada L4K 1B6 (416) 669-5334 Telex: 06-964776

STARTRACKER FINAL REPORT

DOC CONTRACTOR REPORT - DOC-CR-SP-83-015

Prepared for

Department of Communications
Shirley Bay
Ottawa, Ontario

Prepared by

MONITEQ Ltd.
630 Rivermede Road
Concord, Ontario L4K 1B6

MTR 83-58
March 1983

Government of Canada / Gouvernement du Canada

Department of Communications

DOC CONTRACTOR REPORT

DOC-CR-SP - 83-015

DEPARTMENT OF COMMUNICATIONS - OTTAWA - CANADA

SPACE PROGRAM

TITLE: The Evaluation of Charge Transfer Device (CTD) Technology and the Development of a Conceptual Design for a CTD-Based Spacecraft Stellar Sensor

AUTHOR(S): Allan B. Hollinger (Moniteq Ltd.)
Norman T. O'Neill (Moniteq Ltd.)
Dipak Roy (Interactive Circuits and Systems Ltd.)

ISSUED BY CONTRACTOR AS REPORT NO: MTR 83-58

PREPARED BY: Moniteq Ltd.
630 Rivermede Road
Concord, Ontario
L4K 1B6

DEPARTMENT OF SUPPLY AND SERVICES CONTRACT NO: 06ST.36001-2-2723

DOC SCIENTIFIC AUTHORITY: W.S. McMath

CLASSIFICATION: Unclassified

DATE: April 1983

TABLE OF CONTENTS

1.0 INTRODUCTION

Spacecraft stellar sensors have been used for attitude determination as an adjunct to an inertial reference unit. The star sensor updates the absolute attitude of a spacecraft platform relative to the known celestial coordinates of distant stars thereby correcting for long term drift. Solid state star trackers, based on charge transfer devices, improve the reliability and lifetime because of the high quantum efficiency of solid state devices and the geometrical registration inherent in their manufacture. Another advantage is the ability to track more than one star at a time so that attitude information is provided on a continuous basis once the star tracker has acquired its first star.

This report summarizes the methodology and design options involved in developing a stellar sensor based on a charge transfer device. Astronomical and orbital considerations affect the choice of field of view, the orientation of cameras as well as the computational algorithms. A system concept is presented and the characteristics of various charge transfer devices are reviewed. Both systematic and random measurement errors are discussed and a suitable balance is suggested. The last chapter serves as a design document setting out estimates of system power and weight. In general, the examples given in the text are intended to illustrate the various design options and do not necessarily use a consistent set of assumptions. The design document, however, uses a consistent set of assumptions to estimate system performance.

2.0 ASTRONOMICAL CONSIDERATIONS

2.1 Optimum FOV vs Limiting Magnitude

Utilizing the Skymap star catalogue (stellar magnitude < 9.0) we have reviewed the problem of determining the minimum field of view with respect to the probability of finding one or more stars of appropriate magnitude in the startracker field of view. In addition, it is convincingly demonstrated that at least three stars are required in order to unambiguously correlate a given image with corresponding data in the star catalogue. Since the onboard star catalogue will necessarily be restricted to only the brightest stars, the problem of replacing the radiance contribution due to the weaker stars by effective star centres was addressed. We have shown that this procedure must be utilized for stars weaker than those in the bright star catalogue (magnitude < 6.5) or errors of the order of a sizeable fraction of the blur circle would result.

Table 2.1 gives the numbers of stars per magnitude interval in m (= visual magnitude, effective wavelength of 550 nm). The data has been extracted from SKYMAP by Hirshfeld and Sinnott (Ref. 1).

It is convenient to note that the cumulative star density down to magnitude 8.0 gives about 1 star per square degree. Using a Poisson distribution as a first approximation one obtains the probabilities for there being n stars in a given field of view (Table 2.2).

It must be noted that these values are whole-sky probabilities whereas the actual distribution of stars is a strong function of galactic latitude. The preferential occurrence near the galactic equator (0 degrees) becomes stronger as the stars become fainter. No recent literature was found on the distribution of bright stars (but this could be derived from the SKYMAP tape) Going back to Pannekoek's 1924 paper (Ref.2), we derive sample star densities (Table 2.3) for various magnitudes, m, and galactic latitudes in star/(degree**2).

Table 2.1 Star Distribution versus Magnitude

m interval	Total over sky	Cumulative total
-1.5 to -.51	2	2
-.50 to .49	7	9
.50 to 1.49	13	22
1.50 to 2.49	71	93
2.50	192	285
3.50	625	910
4.50	1963	2873
5.50 to 6.49	5606	8479
6.50 to 7.49	15565	24044
7.50 to 8.05	21225	45269
to 9.0		240000

Table 2.2 Probability of Finding Stars versus Field of View

Magnitude limit 5.5 (2873 stars)

Field of View (Square degrees)	Number of stars in the Field of View: 0	1	2	3	4
10	.498	.347	.121	.028	.005
36	.982	.204	.256	.214	.134
64	.012	.052	.115	.171	.191
100	.001	.007	.023	.053	.093

Magnitude limit 6.5 (8479 stars)

Field of View (Square degrees)	0	1	2	3	4
10	.128	.263	.270	.185	.095
36	.0006	.005	.017	.041	.076
64	1.9E-6	2.5E-5	.0002	.0007	.002
100	1.2E-9	2.4E-8	2.5E-7	1.7E-6	8.8E-6

Table 2.3 Star Density versus Galactic Latitude

	Galactic Latitude		
m	0	+20	+90
3	.004	.004	.003
4	.014	.013	.010
5	.054	.047	.034
6	.191	.161	.102
7	.652	.520	.290
8	2.11	1.57	.769

His numbers will not agree exactly with the SKYMAP totals because of small systematic difference in the old and modern magnitude scales, but it can be seen that a magnitude limit of 6+ and FOV of 64 square degrees gives a 99% confidence level of at least one star detected in the field of view.

o Figure of Merit

The star counts above can likewise be used to assess the likelihood of error in a starfield identification. If only two stars are in the FOV, we have only two magnitudes and an angular separation. If the spacecraft attitude is already fairly well known, we have in addition some information on the orientation of the arc separating the two stars. Initially, let us neglect that option. Then the problem is: given one star, what is the probability of finding a second with magnitude $m \pm \mathcal{E}(m)$ within an annulus of width 2δ at a mean radius p, where $\mathcal{E}$ and δ are the magnitude and separation errors. The area of the annulus is then $4\pi\rho\delta$ and the probability is computed from the Poisson distribution as above. This is illustrated in Figure 2.1.

With a magnitude error $\mathcal{E} = 0.5$ and a positional error $\delta = 0.01^\circ$ with, say, an arc $\rho = 8$ degrees, the annulus is 1.0 square degree. If we're searching for a 6th magnitude star, the probability of a random coincidence is 0.17. As soon as three stars are in the field, the situation improves greatly since the third star must lie in a circular patch of radius , and the probability becomes, with the same circumstances 6.4E-5 x 0.17 = 1.10E-5.

Consequently, a minimum of three stars will be needed for position identification.

2.2 Effective Centres of Light

The first part of this problem - frequency of contamination within the point spread function by fainter stars - is just another version of the random star distribution problem, except for the problem of double stars which add a non-random component.

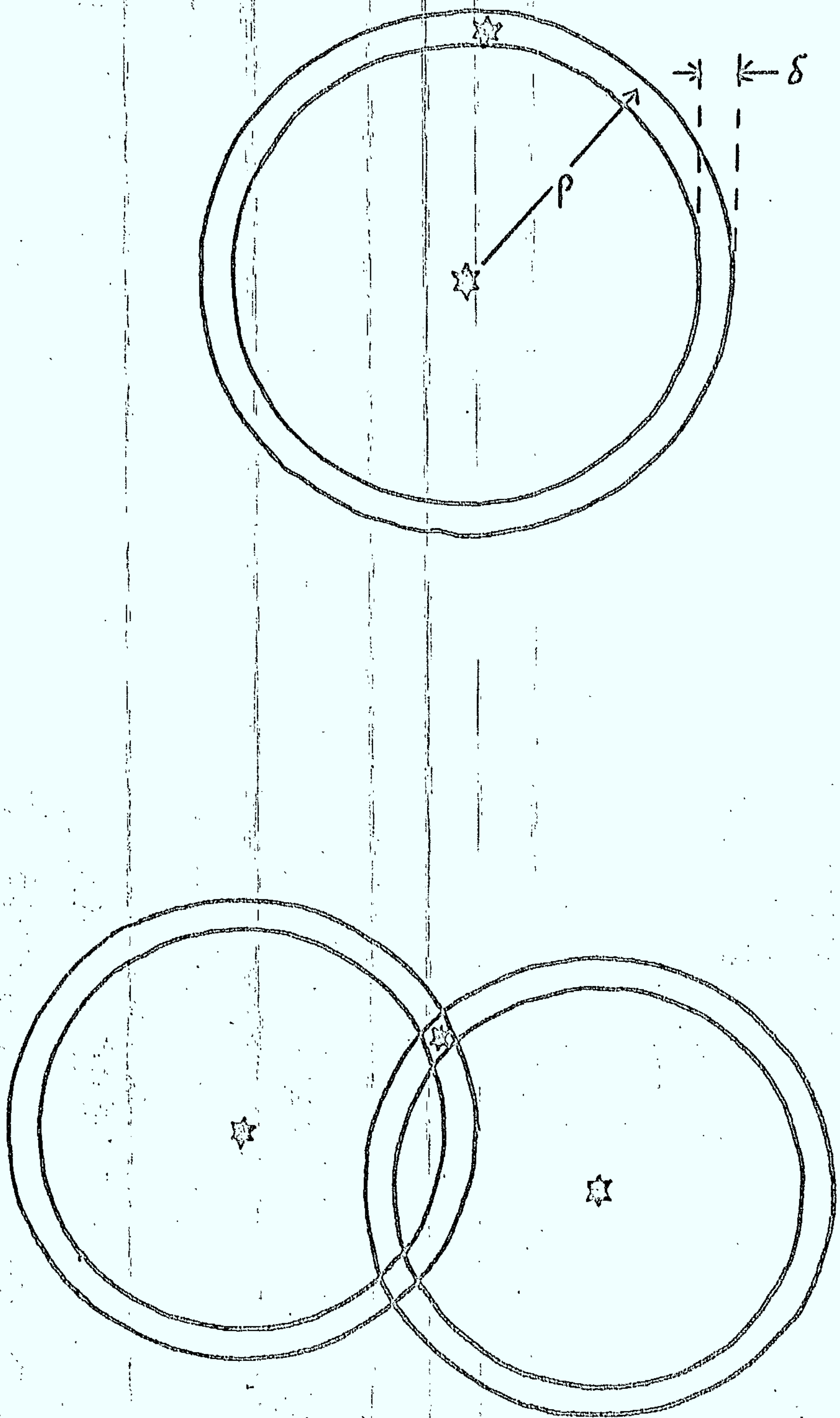

Figure 2.1 Angular Rings of Uncertainty about 2 & 3 Stars

Consider first the double-star problem. It is likely that most of the stars are multiple, but the separations are too small to be resolvable with conventional instrumentation, so, in fact, the positional catalogues gives an effective centre of light for these. The bulk of bright star physical pairs have separations of less than 30 seconds of arc (their magnitude differences and separations are available in machine readable form). Because of these small separations any errors in the formation of a centre-of-light are likely to be negligible. For a very few pairs (like Alpha Centauri) rapid orbital motion presents another problem since photocentre and barycentre do not coincide. These could simply be excluded.

A more serious problem is the clutter from fainter field stars. Given that a star of magnitude 9.0 has 0.10 the luminosity of one of magnitude 6.5 from the relation

$$m_2 - m_1 = 2.5 \log (l_1/l_2)$$

where l is the luminosity and m the magnitude, then a shift of the photocentre by 0.1 x the separation is expected. If the blur circle has a radius of 6', then given 244000 stars with m less than 9.0, the probability of one falling within this circle is 0.15. In the galactic plane, this probability would be more than twice as large. The expected shift due to the interloper would be 0.10 x 6' x 1.414 " 1'. Fainter background stars - for which no machine - readable information is available would be more numerous but the shifts would be smaller - however still obviously in excess of 1". Ultimately, the faintest stars contribute a fairly uniform background level.

If the point spread function is radially symmetric, photocentres could be precomputed for contaminants down to 9.0, but probably one would exclude stars whose effective profiles become too dissimilar from single stars. This depends on the centering algorithm used. Note also that if the point spread is not radially symmetric, the effective blending depends on camera orientation and cannot be precomputed.

2.3 Undesired Images

Double stars were discussed in the previous section. A rough estimate is that less than 15% of the stars would have to be excluded due to orbital motion or wide bright companions that would render their profile too unlike a single star.

Proper motions are known for all of the stars with magnitude less than 6.5 and almost all of those with magnitude less than 9.0. To the arc second level a simple linear change of position vector with time is quite adequate for time periods of a few decades, i.e.

$$\alpha = \alpha_0 + \dot{\alpha}(t - t_0)$$

Almost all of the stars in the primary catalogue have such small motions (less than 0.1"/year) that for short missions they can be ignored completely. The total number of known stars with large proper motion (Ref. 3) are:

greater than 2"/year	73 stars
1"- 2"/year	453 stars
.5"- 1"/year	3061 stars

Note however that about 85% of these are fainter than 10th magnitude

Planets can be recognized by brightness alone only for Venus and Jupiter (m = -4 and -2.5). Mercury, Mars, Saturn and Uranus would require positional prediction also. Except for Uranus (m = 5 .6), the planets are bright enough that a check needs to be made only if a "star" with magnitude less than 3 is in the field (which reduces the amount of checking to be done). Moreover, for missions which stay near the Earth's orbital plane (the ecliptic) as almost all do, a check has to be made only when the field is within 10 degrees of the ecliptic. Since the catalogue might logically be stored in ecliptic coordinates (orbital computations usually being done in same), this would be a very quick check.

For a computation of planetary positions, the usual formulae would be

$$E - e\sin E = \frac{2\pi}{P}(t-T)$$

where P=period, T=time of perihelion, and e=eccentricity. This is Kepler's equation, solved iteratively for E. The coordinates in the planets' orbit plane are

$$X_0 = a(\cos E - e)$$
$$Y_0 = a\sqrt{1-e^2}\sin E \qquad (a = \text{semi major axis})$$

A rotation to the final coordinate system will be of the form

$$X = BX_0 + GY_0$$
$$Y = AX_0 + FY_0$$
$$Z = CX_0 + HY_0$$

where the constants A-H are functions of the three orientation angles

i = inclination angle (angle between orbital and ecliptic planes)
w = mean longitude of perihelion
Ω = longitude of ascending node

All of the parameters P,e,T and A-H are functions of time but they vary slowly enough to present only a slight additional computational load for modest precision requirements (a few arc minutes).

Occultations present a continuing problem except for a satellite orbit lying nearly in the earth's equatorial plane when a camera pointing toward the orbit poles will always be unobstructed. The Sun is excluded by the Sun sensor. The moon will always be recognizable by brightness plus angular size (it is only faint, that is magnitude greater than -5, when it is very near the Sun and excluded for that reason). The daylight hemisphere of the Earth can likewise be rejected by brightness, but the night hemisphere is a problem. Since the orbit of the satellite is known approximately at all times, the portion of the sky covered by the Earth is computable, with equations similar to those above for the planets but the orientational elements vary quite rapidly.

2.4 Correction to Star Catalogue Positions

o Proper Motion

In the SKYMAP catalogue, proper motions are given as μ_α, μ_δ where α and δ are the star's spherical coordinates (right ascension and declination). In spherical coordinates, the positions updated to a time t from a time t_0 are then

$$\alpha = \alpha_0 + \mu_\alpha (t - t_0)$$
$$\delta = \delta_0 + \mu_\delta (t - t_0)$$

If the positions are stored as rectangular coordinates x,y,z with proper motion components μ_x, μ_y, μ_z the updated positions would be

$$x = x_0 + \mu_x (t - t_0) - \frac{1}{2} \left[\mu (t - t_0) \right]^2 x_0$$
$$y = y_0 + \mu_y (t - t_0) - \frac{1}{2} \left[\mu (t - t_0) \right]^2 y_0$$
$$z = z_0 + \mu_z (t - t_0) - \frac{1}{2} \left[\mu (t - t_0) \right]^2 z_0$$

where $\mu = \sqrt{\mu_x^2 + \mu_y^2 + \mu_z^2}$

If the rectangular coordinates are equatorial rectangular coordinates, they are related to α, δ by,

$$x = \cos\delta \cos\alpha$$
$$y = \cos\delta \sin\alpha$$
$$z = \sin\delta$$

o Aberration of Starlight

Here the corrections are

$$dx = \frac{1}{c} \left[\dot{X}(1 - x^2) + \dot{Y} xy + \dot{Z} xz \right]$$
$$dy = \frac{1}{c} \left[\dot{X} xy + \dot{Y}(1 - y^2) + \dot{Z} yz \right]$$
$$dz = \frac{1}{c} \left[\dot{X} xz + \dot{Y} yz + \dot{Z}(1 - z^2) \right]$$

where $\dot{X}, \dot{Y}, \dot{Z}$ are the spacecrafts velocity components relative to the centre of mass of the solar system (essentially relative to the sun). This will be mostly - for an earth satellite - the earth's orbital motion, which is approximately 30 km/sec. Hence v/c, where c is the velocity of light, is about 1.E-4 radians or 20 arc seconds.

The velocity, V, of the Earth is given by

$$V = \frac{na}{\sqrt{1-e^2}} (1 + e \cos f)$$

where a = mean distance of earth from sun = 149.6 E06 km
n = mean angular motion of earth
= 1.991E-7 radians/second
(hence na = 29.79 km/sec)
e = eccentricity of earths orbit = 0.016750
f = "true anomaly" of earth, which is the angle, measured at the sun, between the earth and the perihelion of its orbit.

Therefore, the maximum deviation from a constant velocity is of the order

$$na \left(\frac{1+e}{\sqrt{1-e^2}} \right) - na \sim 0.0169\, na = 0.5 \text{ km/sec}$$

which produces an error of 0.35". It is possible, in most cases then, to regard the earth's orbit as circular, with at most a small correction. In equatorial rectangular coordinates, the velocity components become (Ref.4, p114)

$$\dot{X} = k(\sin \odot + e \sin \Pi)$$

$$\dot{Y} = -k(\cos \odot + e \cos \Pi) \cos \varepsilon$$

$$\dot{Z} = -k(\cos \odot + e \cos \Pi) \sin \varepsilon$$

$\odot$ = true ecliptic longitude of sun
Π = longitude of perigee of "solar orbit" relative to Earth
ε = obliquity of ecliptic (tilt of earth's axis)

$\odot$, Π may be obtained from simple power series in time

Table 2.4 summarizes the problems and suggested solutions associated with the usage of stellar positions as attitude reference points.

2.5 Secular Perturbations of Satellite Orbit

The major changes in a near earth orbit are caused by the earth's oblateness. Except when the orbit is in terminal decay, these dominate the effect of residual atmospheric drag.

Given the usual orbital elements for the satellite:

- a = semi-major axis
- e = eccentricity
- i = inclination of orbit plane to equator (0 degrees when motion is parallel to rotational motion of an equatorial point, 180 degrees when antiparallel)
- Ω = right ascension of ascending node, (i.e. point where the satellite crosses the equator proceeding northward)
- ω = argument of perigee (angle between equator and perigee, measured at the centre of the earth,

The leading terms in the variations are given by Sterne (Ref.5, p122) where the constant $B=JR^2/3$ where R is the equatorial radius of the earth and J is the leading harmonic in the gravitational potential, i.e. the coefficient of the $P_2(\sin \phi)$ legendre polynomial. Naturally, there are higher order terms, but the largest are about 1.E-3*J.

Table 2.4 Ambiguous Images

	Occurrence	Solution
Proper Motion	c. 100 > 1" per year (mag. < 6)	* simple linear expression to periodically update
Aberration of Starlight	all stars	simple analytical corrections, periodic update
Double Stars	c. 15% of star catalogue	* recognize in coarse search
Planets	8	Venus and Jupiter - mag. rest m < 3 except for Pluto - m = 5.6
Star Clutter	m > star catalog limits	effective centres of light from star catalog - otherwise weak stars form uniform background
Variable mag.	c. 1% amp. > .5 mag.	* recognize in coarse search
Sun, Moon, Earth		brightness threshold

* star catalog flag and data

Most of the variations are periodic and of limited amplitude. Generally, for close ($a<1.3R$) orbits, the following statements can be made (Ref. 6):

1) Long Periodic (greater than 5 hours) perturbations average about ± 500 m along track, ±150m radial and ± 50 m across the track;

2) Short periodic terms (less than 2 hours) average about one-tenth as much in amplitude as the long-periodic terms.

However, the nonperiodic (secular) terms (those with the true anomaly, as argument, in Sterne's notation) cause continuous changes in and . These are, roughly,

$$\dot{\Omega} \approx -9.97\left(\frac{R}{a}\right)^{3.5}(1-e^2)^{-2}\cos i \qquad \text{(degrees/day)}$$

$$\dot{\omega} \approx 4.98\left(\frac{R}{a}\right)^{3.5}(1-e^2)^{-2}(5\cos^2 i-1) \qquad \text{(degrees/day)}$$

R = 6378 km, so that if, for example, we insert the numbers from the RADARSAT example, with i = 99.49 degrees and altitude = 1001.3 km, e=o, we have $\dot{\Omega}$ = 0.986 degrees/day = 360 degrees/year. Consequently, the orbit plane precesses about the earth's axis at 1 rev/year so that the orbit plane is, on average, fixed relative to the sun. ($\dot{\omega}$ is, by the way, undefined since the orbit is effectively circular).

Effects of the orbit and orbit variations on camera position and star catalogue:

o Geosynchronous Case

Generally, the orbit will be selected, and actively corrected if necessary, to maintain a position near a point in the equatorial plane fixed relative to earth stations. Slow librations (quasi- periodic displacements) about the corotating point are expected even in the most naturally stable orbits with amplitudes, mostly in longitude, of a few degrees (Ref.7).

The most obvious selections for camera axes are the pitch direction and either the roll axis or the yaw axis in the anti-earth direction. The pitch axis points toward the celestial poles, neither of which is a particularly rich star field, and the other axes lie in the equatorial plane with consequent frequent occultations by the moon and sun, so this is not necessarily the ideal choice. Assuming, however, a 10 degree field of view for the cameras, it does reduce the star catalogue to a 100 square degree patch at the chosen pole (pitch camera) plus a 360 x 10 square degree belt (roll or yaw camera). Allowing a $\pm$ 2 degree safety margin, the total area of the sky seen during one day is 5200 square degrees or about 13% of the sphere. In the extreme case of a magnitude limit of 6.5, this yields 1080 stars. Field motion for the equatorial camera would be 15 arc sec/second.

Placing the cameras at 45 degrees to the pitch axis would have both cameras share the same catalogue of about 730 stars for the same 6.5 limit (i.e. for a sky fraction of approximately 14 degrees x 360 degrees x cos(45 degrees)/41253 square degrees = .09). Occultations by the sun and moon would be eliminated although the sun would still be a problem if the baffling is less than 100% efficient.

o Precessing Polar Orbit - Sun Synchronous

Once again, the pitch axis is nearly fixed, with a motion on the order of 1 degree/day, hence update frequency for the catalogue would be slow. On the other hand, if the field is void, the camera would be inoperative for several days until orbit precession brought a new field into view. Presuming that the satellite rotates once/revolution so that it is earth oriented, a camera in the yaw/roll plane will sweep the sky once/revolution or about every 100 min. so that image motion will be 200 arc sec/second.

The slow change of field for the pitch axis camera need not be a fatal flaw if integration times can be arbitrarily increased (a reasonable option given the slow field rotation of the pitch camera). In consequence a fainter catalogue limit could be set. Moreover, if the orbit plane passes near the Sun, the pitch axis camera would always be free of solar obscuration.

Placing two cameras 90 degrees apart with both 45 degrees to the pitch axis would allow both to sweep the same zone in the sky with image motions of 150 arc sec/seocnd. A void field would be by passed in 10 /360 x 100 min = 3 minutes and the required star catalogue storage would be 730 stars on average, as in the geosynch. case. Here, however, the precession of 1 degree/day would require updates every day or two (less frequent if the stored band of sky is widened).

Placing the cameras 45 degrees from the pitch axis toward the leading and following roll axis would keep both free of earth occultation and (for RADARSAT) free of solar occultation. The moon could not be eliminated.

3.0 SYSTEM DESCRIPTION

3.1 The Attitude Imager Monitor (AIM)

Figure 3.1 shows a block diagram of the Attitude Image Monitor. The AIM can handle more than one smart camera. The AIM microprocessor selects the proper camera, defines the track window within which a star image will be found, and determines the camera integration time. The AIM has primary responsibility for extracting a copy of a camera video buffer and processing this information to determine the centroid of the stellar image. A comparison of the estimated and measured positions of the stellar images allows determination of the satellite attitude.

A serial interface supports communication between the different smart cameras, the other spacecraft systems and the Attitude Image Monitor. This interface is functionally equivalent to the serial interface in the Programmable Image Controller. The ROM ,RAM and video buffer are essentially the same as for the Programmable Image Controller differing only in the memory size that need be allocated for program and variable storage.

A star catalogue consists of CMOS PROM (up to 70 kbytes); it will contain a reference to all stars that are of importance for the satellite attitude determination. The organization and memory requirements are described more fully in section 6 .

A watchdog timer will contain simple sensing circuitry to check for the presence of the camera clocking and timing signals in order to allow the AIM microprocessor to take the appropriate action whenever one or more signals are missing. The watchdog timer also determines if an attitude image monitor is malfunctioning and reports to the central status processor on the satellite.

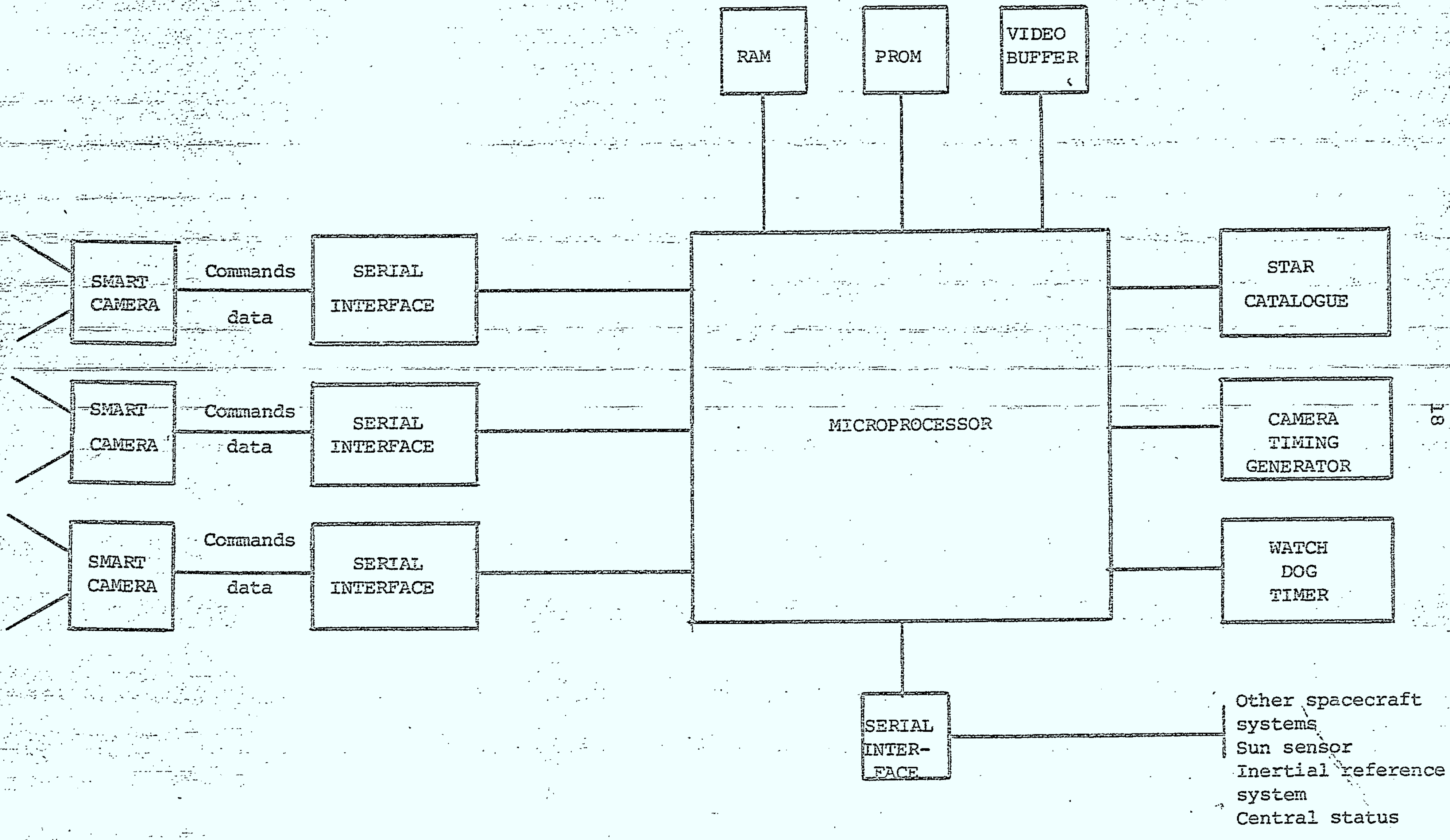

Figure 3.1 BLOCK DIAGRAM A.I.M. (Attitude Image Monitor)

3.2 Programmable Imager Controller

Figure 3.2 is a schematic diagram of the programmable image controller. The heart of the Programmable Image Controller is the microprocessor; under control of a software program that is stored in PROM, the microprocessor routes all control signals for data acquisition, data storage as well as providing an interface to the Attitude Image Monitor. The other system components include an analog signal processing board, an analog to digital converter, and a synchronization and timing generator. The charge transfer device is operated by a series of clocking waveforms which are generated by the microprocessor and amplified by driver cicuitry. The system also performs such housekeeping functions as temperature and shutter control. An eight or sixteen bit CMOS microprocessor will be selected to minimize power consumption.

o Analog Signal Processing

The output of the image sensor is amplified and filtered by an analog signal processing chain. The preamplifier consists of an operational amplifier, which is selected for its noise and bandwidth characteristics. A maximally flat elliptic filter ensures that any noise, with a frequency spectrum above half the sample frequency of the correlated double sampler, will be attenuated to an acceptable level. This prevents the foldback of unwanted signals into the signal passband. The zeros of the filter should be positioned at the sample frequency and multiples thereof.

The correlated double sampler consists of a discrete time differentiator followed by a discrete time integrator and a sample and hold. This circuit will remove reset and clocking noise of the image sensor. In addition it will attenuate the uncorrelated low frequency 1/f noise of the output transistor of the array. The sample and hold ensures that the video data is stable during the conversion period of the A/D converter.

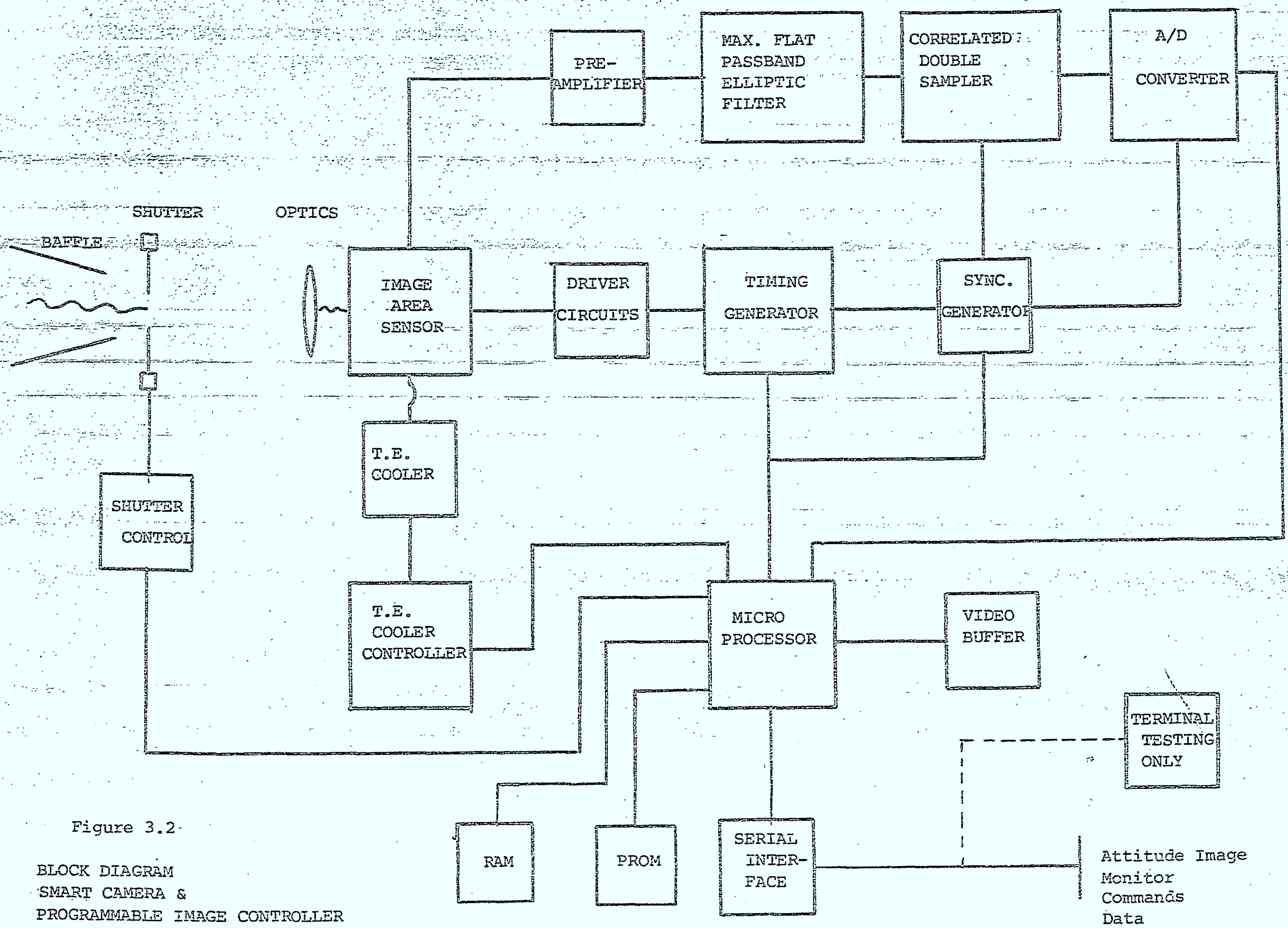

Figure 3.2

BLOCK DIAGRAM
SMART CAMERA &
PROGRAMMABLE IMAGE CONTROLLER

The A/D converter digitizes the analog signal levels with sufficient resolution and conversion speed. A converter must be chosen which minimizes power consumption while maintaining the desired resolution and conversion speed.

The timing generator is controlled by the microprocessor; it generates the necessary waveforms to operate the image sensor. The clocking circuits must be capable of driving the array's clocking lines despite their relatively large capacitance.

The sync generator coordinates the timing generator, the correlated double sampler, the A/D converter and the microprocessor. In other words, it is a hardware interface between the aforementioned subsystems.

o Other Subsystems

The shutter control consists of a current amplifier that converts a control signal from the microprocessor into a latching action on an electro- mechanical shutter. It also provides the microprocessor with information on the actual status of the shutter (open or closed).

The PROM memory will contain the microprogram that operates the programmable image controller. The RAM memory will be of sufficient size for stack, accumulator and variable storage. Power consumption will be smaller if byte wide CMOS RAM is used.

The video buffer is approximately 1 Kbyte in size; it is used to provide temporary storage for all the video information about a star image. Upon command of the Attitude Image Monitor, data will be collected and stored in the buffer; at the appropriate time the contents of the buffer are transferred to the Attitude Image Monitor for further processing.

The serial interface will send and receive all command and data that is transferred between the Programmable Image Controller and the Attitude Image Monitor. It could consist of an RS-422 interface that is capable of sending and receiving data rates up to 1Mbit/sec. This data rate should be more than sufficient to handle the communication between the P.I.C. and the A.I.M.

3.3 Charge Transfer Devices

The two types of solid-state imaging devices of interest, the CCD and the CID, are similar in their basic sensing mechanism, which involves the collection and storage of photon-generated charge under MOS capacitor plates on a silicon substrate. They differ mainly in the manner of charge detection. In the CCD the signal charge is transferred across the array to charge amplifiers for detection; in the CID, the charge is detected in place at each sensing site by an intrasite transfer.

The circuitry used to select and provide readout of image sensors contains a number of Johnson noise sources. The distributed resistance of the array lines used for signal sensing, the line selection switch, and the first preamplifier stage each contribute temporal noise to the video signal. In addition capacitor reset noise (kTC noise) can be significant when certain readout methods are used. Shot noise in the dark current and or junction leakage current in the MOS line select multiplexers can be significant under certain conditions. The Johnson noise sources usually are dominant in large arrays operating at high video rates. The level of kTC noise referred to the array can be made arbitrarily small, however, since gain can be used between the array output and the clamp capacitor. The parallel injection technique does not allow complete elimination of kTC noise. The column reset transistors introduce kTC noise that is not rejected. Voltage noise at the input of the preamplifier results in an equivalent input charge that is directly proportional to the array output capacitance (q=cv). Theoretical preamplifier noise levels of a few hundred carriers result from array output capacitance levels in the 10pF region. kTC noise can be either negligible or the predominant temporal noise source, depending upon the specific array design and readout method.

Under low video rate readout conditions, Johnson noise can be minimized by restricting the noise bandwidth of the video amplifier. Shot noise originating in array dark current and line select multiplexer junction leakage can be limiting under these conditions. Reduction in array operating temperature can be used to control these thermally generated currents and consequently the resultant shot noise.

Solid state imaging sensors can exhibit a fixed nonuniform spatial background in the reproduced image. The major sources of fixed pattern noise in image sensors are transistor switching interference, array photolithographic variations, and bias charge variations. In the case of CID's, nonuniform coupling of the MOS transistor scanner output voltage to the video signal results in a component of fixed pattern noise that repeats from scan to scan. For CCD's, there is a similar component arising from the multiphase clocks which transfer charge between wells of the CCD. Variations in row to column crossover capacitance arising from either insulator thickness or photolithographic variations cause a two dimensional component of fixed pattern noise. Variations in bias charge from site to site, caused by differences in storage capacitance or threshold voltage, also result in a two dimensional component of fixed pattern noise.

Dark current nonuniformity can be an important source of pattern noise, particularly at room temperature. Low dark current performance can be an advantage under these conditions.

The organization and nondestructive readout capability of the CID imager gives rise to a number of specialized functions. The X-Y addressable organization allows random access to array pixels. The non destructive readout feature combined with X-Y access allows linear combinations of pixel signals to be sensed giving rise to spatial transform readout. Signals can be repeatedly read and summed to improve dynamic range. While CCD's do not allow nondestructive readout, they do permit on chip averaging over the rows and columns by varying the order of the horizontal and vertical clocking pulses.

3.4 The Charge Injection Device

The major features of the CID imagers are summarized below:

o An X-Y addressing capability which provides exceptional flexibility in array readout. This capability significantly reduces clock frequency, peripheral electronics, and data handling rates. This feature also makes the device compatible with microprocessors and A/D converters.

- o A high effective active area on the image plane. There are no opaque areas and the electrodes can be made of very thin polysilicon because of the low clock frequency. This allows a broad spectral response and high sensitivity without loss of signal to noise capability.

- o No charge transfer loss. In the CID the signal is read directly at the sensing site.

- o Tolerance to optical overloads without complicating the basic array architecture. In the CID the charge is contained at the storage location, and the tendency for excess charge to migrate to adjacent sites is greatly reduced.

- o A non-destructive readout capability allows more flexibility. This feature has been used effectively to reduce noise.

- o Cooling requirements are minimal. Dark current is generated only in the depletion region of the device and the depleted area is much smaller than the photosensitive area.

3.4.1 Operation of CID Imagers

The charge injection approach to solid state imaging employs MOS capacitor structures to collect and store photon generated charge signals. Charge is injected from the MOS storage (inversion) region into the substrate to clear the storage region and, in some cases, to provide signal readout. For an area imager, X-Y addressing is achieved by using two MOS capacitors at each sensing site. The capacitors are coupled such that stored charge can be transferred from one capacitor to the next by creating a potential difference. Injection occurs when both electrodes are switched off.

Various methods can be used to couple surface charge between adjacent electrodes. Fringing fields are created by using a narrow interelectrode gap, by overlapping insulated electrodes, or by the use of a conductive diffusion. The last method is compatible with standard MOS process. Figure 3.3 shows a cross-section of a sensing site, fabricated with conductive diffusion, under various gate voltage

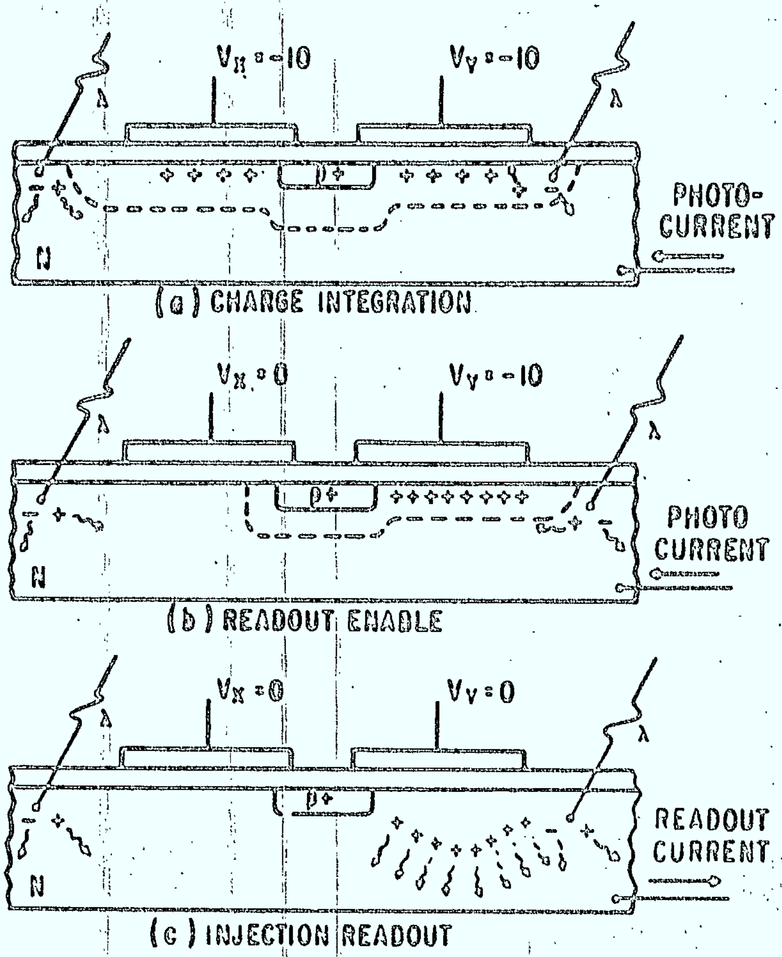

Figure 3.3 Cross-section of X-Y addressable sensing site showing location of stored charge under (a) integration, (b) read-out enable, and (c) injection conditions.

conditions. Use of overlapping gates can reduce cell size. The structure reported by G.E. contains a first level of polysilicon electrodes and a second level of transparent metal oxide electrodes. Figure 3.4 shows the cross-section of a CID imager cell fabricated with overlapping electrode structures.

The charge stored in the inversion region can be injected into the substrate and removal of charge takes place by recombination. If the spacing between sensing sites is much less than the diffusion length, a portion of the charge injected at one site will be collected by adjacent sites with a resulting loss of resolution. In addition, the injection pulsewidth cannot be much shorter than carrier lifetime or else part of the injected charge will be recollected and result in image lag. The solution to these problems has been to fabricate CID imagers on epitaxial wafers. The epitaxial junction, which underlies the imaging array, acts as a buried collector for the injected charge. If the thickness of the epitaxial layer is less than, or comparable to the spacing between sensing sites, the injected charge will be collected by the reverse biased epi-junction and injection cross talk is avoided. Figure 3.4 shows the cross-section of a sensing site fabricated on a epitaxial layer. The introduction of the epitaxial collector, however, affects imager sensitivity. Part of the charge generated in the silicon between sensing sites can be collected by the epi-junction instead of the storage capacitors. This is particularly true for long wavelength radiation.

3.4.2 Readout Methods

The signal charge stored in CID imaging arrays can be sensed by measuring either the charge that flows upon injection or the voltage change induced by charge transfer between the two storage capacitors that comprise the X-Y addressable storage site. Different readout methods are briefly discussed below:

o Sequential Injection (Drive Line Readout)

The displacement current that flows in the substrate upon charge injection also flows in the driven array line. An array designed for drive line readout is

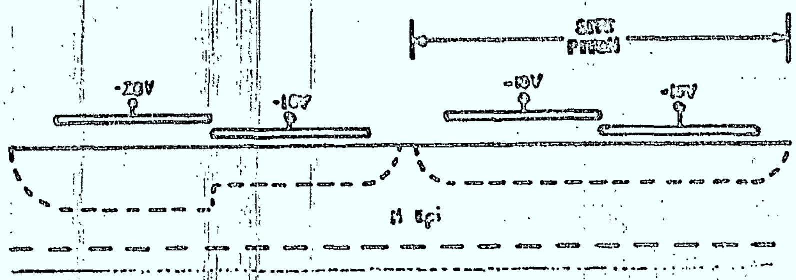

Figure 3.4 Sensing Site Cross Section of an overlapping gate CID structure fabricated on an epitaxial layer.

shown in Figure 3.5. A larger voltage is applied to the row of electrodes than to the column electrodes so that photon generated charge collected at each site is stored under the row electrode. A line is selected for readout by setting its voltage to zero by means of the vertical scan register (ROW ENABLE condition of Figure 3.5) The charge is then injected by driving each column voltage to zero, in sequence, by means of the horizontal scan register and the signal line. The net injected charge is measured by integrating the displacement current in the signal line over the injection interval. Charge in the unselected lines remains under the row connected electrodes during the injection pulse (HALF SELECT condition of Figure 3.5).

o Preinjection

The preinjection readout technique is based on the measurement of the change in charge that occurs at each addressed sensing site when a complete row of sites is cleared (injected) simultaneously. The schematic diagram of an array configured for preinjection readout is shown in Figure 3.6. Equal row and column bias levels are normally used with this readout method. A low input impedance (transconductance) amplifier is used so that, during each scan of the array columns, the column potentials are reset to the reference voltage. Prior to each scan of the array columns, during the horizontal retrace interval, voltage is removed from the selected row to clear the row of sites to a bias charge level, and then reset to its original value. The potential of all columns had been reset to the column reference potential during the previous scan interval. Since signal charge was present under the addressed row electrodes when the column potential was reset, the removal of the signal charge by the injection operation results in a voltage being induced on the floating column electrodes proportional to the injected signal charge. The induced video signal is then read out by the column scanner.

This preinjection readout method has a number of advantages and some limitations. Array fixed pattern noise is automatically rejected since the only net change in array charge levels prior to each video line

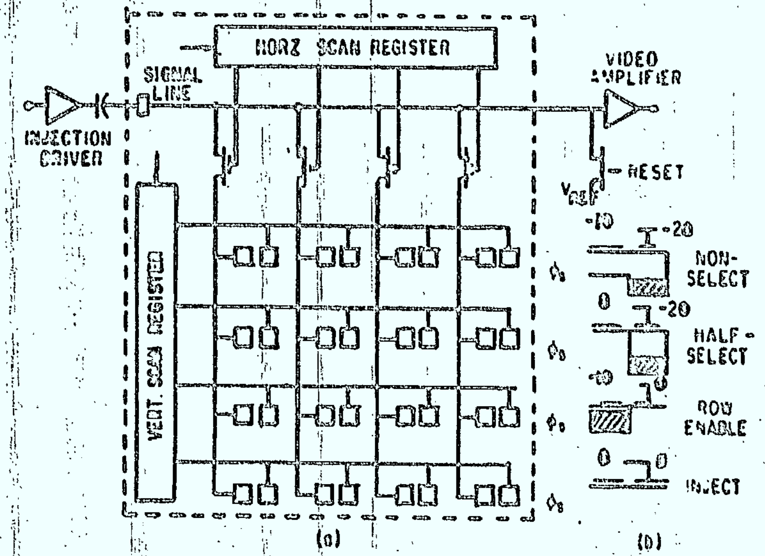

Figure 3.5: (a) X-Y accessing scheme for a CID imager; (b) Silicon surface potentials illustrating Drive line read-out.

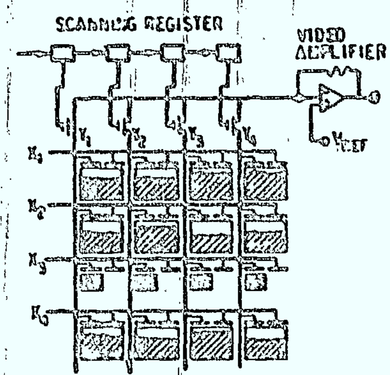

Figure 3.6: Schematic diagram of a 4 x 4 CID array designed for pre-injection read-out. Silicon surface potentials and signal charge locations are indicated schematically.

scan is the injection of signal charge. The technique is compatible with high speed sampling of the induced column signals as required for TV compatible operations. The main disadvantage with this readout technique is the switching noise coupled into the video signal by the column scanner. This component of the fixed pattern noise repeats for each video line and can be rejected if one line of video storage is provided.

o Parallel Injection

The parallel injection technique allows the functions of charge injection and charge detection to be separated. Signal charge levels can be sensed at high speed during a line scan and during the line retrace time interval all of the charge in the selected line can be injected in parallel. If injection is deferred, nondestructive readout results. The parallel injection technique is well adapted to TV scan formats in that the signal is read out line by line. It is not adapted to random scan applications.

In an array of MOS coupled capacitor pairs, as is used in the present charge injection imagers, all of the signal charge will be stored under the row connected electrodes if the row voltages are larger than the column voltages. This condition is illustrated in Figure 3.7 for rows X1, X2, and X4. This method of biasing effectively prevents the charge stored under the row connected electrodes from affecting column voltages. The voltage on all array columns, Y1 through Y4, can be set to a reference value either by means of a previous column scan readout, or through the use of the column switches, S1 through S4.

If the voltage on a row electrode is then switched to zero, signal charge will transfer from the row connected electrodes to the column connected electrodes in the selected row of sensing sites. This is diagrammed in Figure 3.7, for row X3. The voltage on each of the column lines will then be reduced by an amount equal to the signal charge divided by the column capacitance.

The signal can be sensed by sequentially connecting each column line to a video amplifier by the use of a

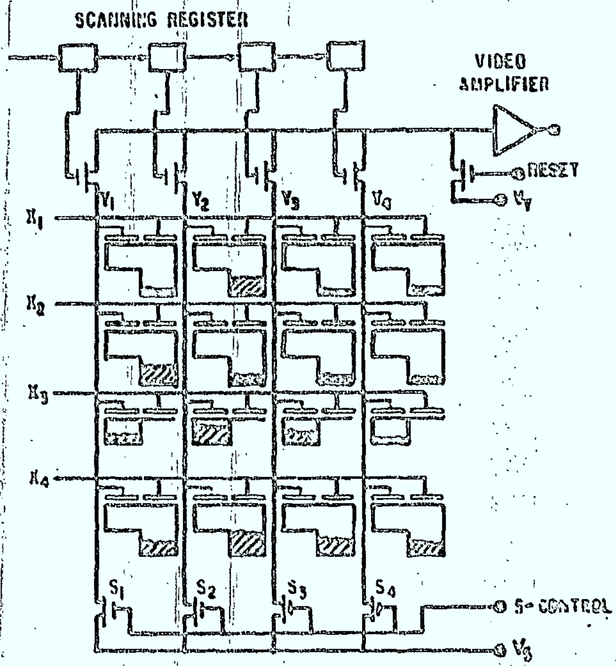

Figure 3.7 Schematic diagram of a 4 x 4 CID array designed for parallel-injection read-out. Silicon surface potentials and signal charge locations are indicated schematically.

scanning register and MOS switches. The readout operation consists of resetting the video amplifier input to the reference voltage, and then stepping the scanning register to the next column line. After all columns of the array have been scanned, charge can be returned to the row connected electrodes by reapplying voltage to the previously selected row. This action retains the signal charge for future processing, and constitutes a non-destructive readout (NDRO) operation.

Alternately, at the end of readout of the selected row, while the row voltage is maintained at zero volts, the signal charge can be injected from the selected row to the substrate, all sites in parallel, by switching all column voltages to zero simultaneously. This action clears the sensing sites of charge and allows the start of a new signal integration time interval for that row.

o Row Readout

A second charge transfer readout method is diagrammed in Figure 3.8. Readout is effected by driving the column connected electrodes to cause charge to transfer to the row connected electrodes. The condition diagrammed in the figure is with the third row connected to the video amplifier by the vertical scanning register. The horizontal scanning register is operated at the video element rate to sequentially connect the column drive voltage to the array columns. Each element of signal charge is transferred to the row electrode, externally sampled, and then transferred back to the column electrode.

At the end of each line scan, the selected row and all array columns can be driven to cause injection. For nondestructive readout of this array, the injection operation can be deferred.

The advantages of this readout method over previously described techniques is that the horizontal scanner is isolated from the video signal, kTC noise can be easily rejected, and nondestructive readout can be readily mechanized.

3.4.3 Dark Current and Blooming

The CID approach permits significantly more silicon area to be used for photon charge generation than for charge storage. This results in an advantageous dark current situation because the thermal charge generation

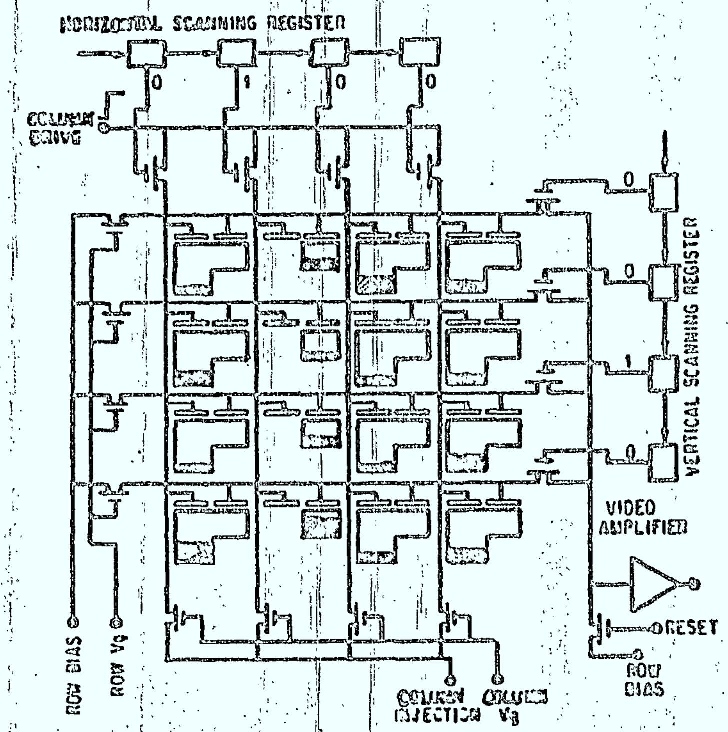

Figure 3.8 Row read-out array diagram illustrating sensing of the third row, second column.

rate in nondepleted bulk silicon is orders of magnitude less than in the depleted storage region.

Consequently, each image sensing site collects and stores photon generated charge from essentially the total site area but generates dark current only in the storage area. Also, no separate storage area is required for image readout, so that a dark current contribution from this source is avoided. The use of bias charge in the storage area results in an additional reduction of dark current since the surface thermal generation rate in MOS structures is much smaller under inversion conditions than under depletion conditions.

The epitaxial CID structure is resistant to image blooming since each sensing site is electrically isolated from its neighbours. Charge spreading in the substrate is minimized (relative to devices without an epitaxial layer) by the underlying charge collector.

3.5 CCD Technology

There are essentially three different types of CCD frame transfer imagers all of which function with a buried channel. These are a front side illuminated device (e.g. EEV 8600), a thin backside illuminated device (RCA SID) and a virtual phase device (T.I. TC 201). Although other designs have been completed using surface channels they perform more poorly than the buried channel devices.

The virtual phase concept (Figure 3.9) simplifies the manufacturing process by eliminating the overlapping gate electrode structure common to all other CCD processing methods. This gives many added advantages of simplified clocking (one clock versus two to four clocks), lower dark current which is an order of magnitude lower than other CCD technologies, high quantum efficiency with improved blue response and a potentially much lower cost because of a minimum amount of masking operations during production.

Because the number of deposited clock levels on the devices surface has been reduced to one, the occurrence of surface damage and shorts is reduced to the same high degree of reliability as in the standard MOS technology. This reduces the number of column defects.

Figure 3.9

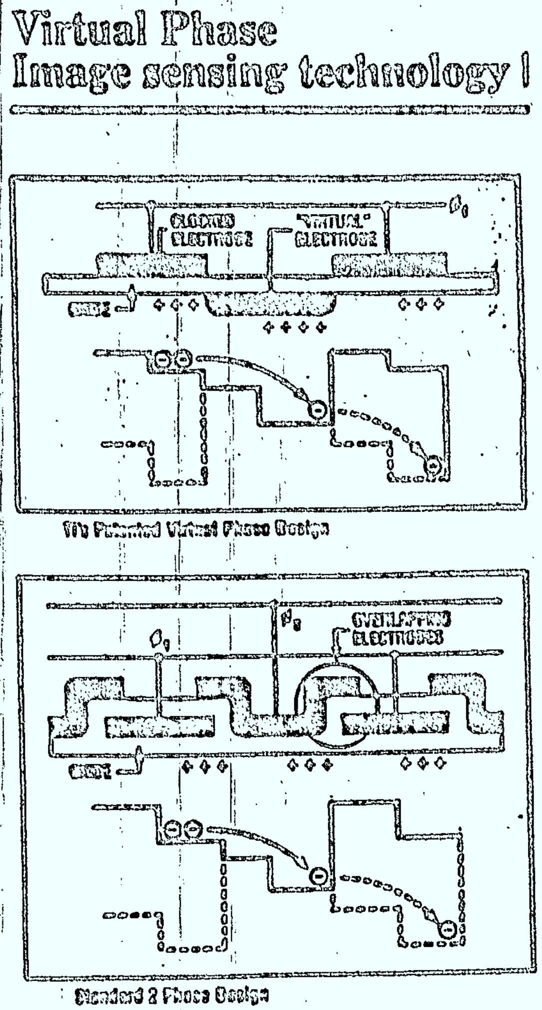

A very important feature of the virtual phase technology in our application is the very low dark current. There are three major components in the total dark current in a CCD imager; a surface component due to the interface states; a depletion region component due to the current supplied by the bulk generation recombination centres;and , a diffusion component due to the minority carriers from the neutral undepleted bulk of the silicon.

Of the three, the surface component is the most important one in normal CCD image sensors. However, in the V.P. technology, the contribution of this surface component is negligible because the SiO2 -Si interface states are filled with holes. In addition it is also possible to bias the clocked phase during the integration period at a negative gate potential. This will force holes to the surface over the entire imager area, further reducing the total dark current.Under these circumstances the dark current is reduced to .4nA/cm**2 an order of magnitude lower than for other CCD image sensors.

3.6 Operation of CCD Frame Transfer Imagers

A frame transfer CCD image sensor (Figure 3.10) consists of an image integrate area, an image storage area and a horizontal transport register that clocks single pixel information on a line by line basis to an output amplifier.

A typical operational sequence is described below. Initially the photocharge is integrated within the image area. Next the entire image area is quickly dumped into the image storage area where the data is read out line by line by dumping one line at a time into the horizontal shift register. An integral output amplifier converts the charge packet associated with each pixel into a discrete voltage. The next image is simultaneously collected in the image area.

Figure 3.10 CCD FRAME TRANSFER ARRAY SCHEMATIC

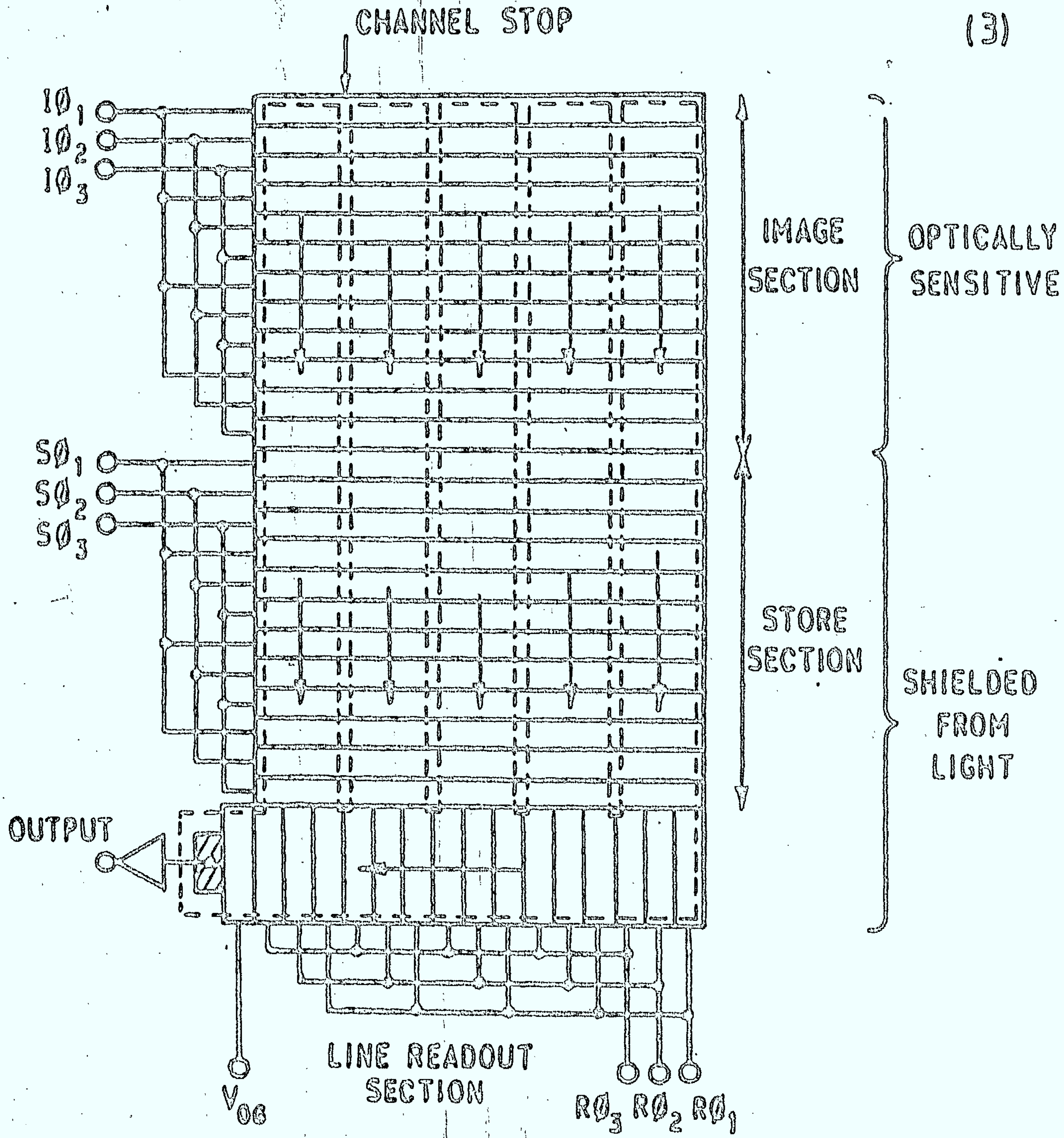

The timing constraints for a CCD image sensor are far more complicated than those for a CID imager, because the CID can be accessed randomly in groups of 4*4 pixels whereas the CCD image has to be read out completely at all times. For a star tracker, therefore, a CID sensor would have a definite advantage because at any given time we are only interested in a maximum of four stars in our field of view. Translated into CID terms, this would mean an access of 4 groups of 4*4 pixels (in tracking mode).

However, we can generate a similar sequence for a CCD imager. To facilitate comparison we have to translate our requirement to 4 groups of 4 lines and select 4 pixels in each line. The worst case timing requirement for each pixel is determined by the minimum integration time, the time that is required to dump the entire image section into the storage section and the time that is necessary for the 4 top lines in the storage section to be clocked through into the serial register. This can all be done at maximum allowable vertical clock frequency. Once a line is dumped into the serial register, it is clocked out at the maximum horizontal clock frequency until the first pixel of interest is reached. The horizontal clock is then slowed down to a value that is determined by the total number of pixels of interest (4*4*4 = 64) and the minimum integration time (10 msec).

This concept minimizes the required video bandwidth for the analog signal processing chain and therefore reduces associated Johnson noise.

3.7 Analog Signal Processing

To assess the performance of the analog signal chain, we have to determine which noise sources are present and their contribution to the total system noise

The circuitry used in any array to provide readout of the individual pixels contains several Johnson noise sources. The distributed resistance of the array electrodes, the line selection switches and the first preamplifier stage will all contribute noise to the video signal. Furthermore, capacitor reset switch noise (kTC noise), shot noise in the dark current and leakage current in the line multiplex switches can be significant.

o Reset Noise

When a switch is used to set the voltage across the capacitor, the final voltage on the capacitor has an uncertainty due to the finite resistance of the switch. The magnitude of this uncertainty is determined by the following equation:

Vn = (kT/C)**.5 (Volts)
where k = 1.38 E-23 (J/K) (Boltzmann's constant)
and T = temperature in degree Kelvin
and C = output capacitance

The reset noise, N(kTC), measured as an r.m.s fluctuation inthe number of carriers is given by:

N(kTC) = ((kTC)**0.5)/q (rms carriers)
where q = 1.6 E-19 (Electronic charge in Coulombs)

With a typical array output capacitance of 10 pF this generates at room temperature:

N(kTC) = 1261 (rms carriers)

This noise however can be suppressed by means of the correlated double sampling technique. The amount of suppression that can be achieved is determined by the degree to which the first sample is a measure of the kTC voltage. For a video system whose bandwidth is determined by a first order roll off frequency of fc(Hz) , the sample voltage can be determined as:

Vsample = Vsignal (1 - exp(-2*pi*fc*ts)) (Volt)
where ts = sample interval time

if the sample interval is chosen in such a way that 2*pi*fc*ts=5 , then

Vsample/Vsignal = .993

In this case, kTC noise would be suppressed by a factor of 1/(1-Vsample/Vsignal) = 150. This would reduce the equivalent noise contribution to 1261/180 = 8.4 (rms carriers).

o Preamplifier Noise

Using an ultra low noise dual matched N channel field effect transistor like the CD860 from Crystalonics, we could achieve the following equivalent noise level:

Na = Vn(rms) * Cin/q (rms carriers/(Hz**.5))

where Vn = spot noise figure of amplifier
Cin = input capacitance of amplifier (Farad)

In case of the CD860, these figures are:

Vn(rms) = 1.4 nV/(Hz**.5) (at 1 kHz)
Cin = 30 pF

Therefore:

Na = .26 (rms carriers/(Hz**.5)

If we assume a video bandwidth of e.g. 10 kHz, than the total contribution of the preamplifier would be:

Na = 26 (rms carriers)

3.8 Availability of CID's

Although CID technology has matured during 10 years of development at General Electric (GE) under various U.S. Defense and NASA contracts, the devices are not offered commercially. However, detailed discussions have taken place with various people at GE regarding procurement of up-to-date CID imagers. The company has now expressed willingness to sell sample devices for important scientific applications in order to establish an edge over the competing CCD technology. Out of a wide variety of CID imagers that have been developed, the ST-256 device, developed for NASA, appears to be most suitable for the specific application. An improved version of ST-256 is expected to be available shortly. A preliminary specification is given below (Table 3.1).

Table 3.1 Characteristics of the ST-256 Array

Array Size	256 x 256
Pixel Size	20 x 20 micrometers
Full Well	1.3 e06
Dark Current (/pixel)	<1e04 electrons/sec at 0 C
Fixed Pattern Noise	0.5% Full well
Response Variation	less than 1%
Dark Current Variation	less than 1.5%
Quantum Yield	0.4
Response Point Spread	Trapezoidal
Radiation Tolerance	greater than 1E04 Rad
Readout Option	4 x 4 Pixel Subblock with increments of 2 pixel
Responsivity	See Figure 3.11

o Device Architecture

The architectural details of the ST-256 device is not yet available however, the device is very similar to a 128 x 128 array developed previously. Figure 3.12 shows the sensor layout of the 128 x 128 array. The array can be selected by groups of four on both horizontal and vertical axes. The array is designed for sequential readout of image subblocks selected by means of scanning registers. In operation, a logical "one" can be entered into each scanning register and shifted, as required, to select the desired subgroup. The column drive lines, E through E can then be driven to obtain four parallel outputs. In addition to 128 active rows, another row is available to provide differential cancellation of column drive interference. This compensation row is selected for every row address and is cleared when every row is cleared. A typical readout sequence change the row and column voltage bias and consists of:

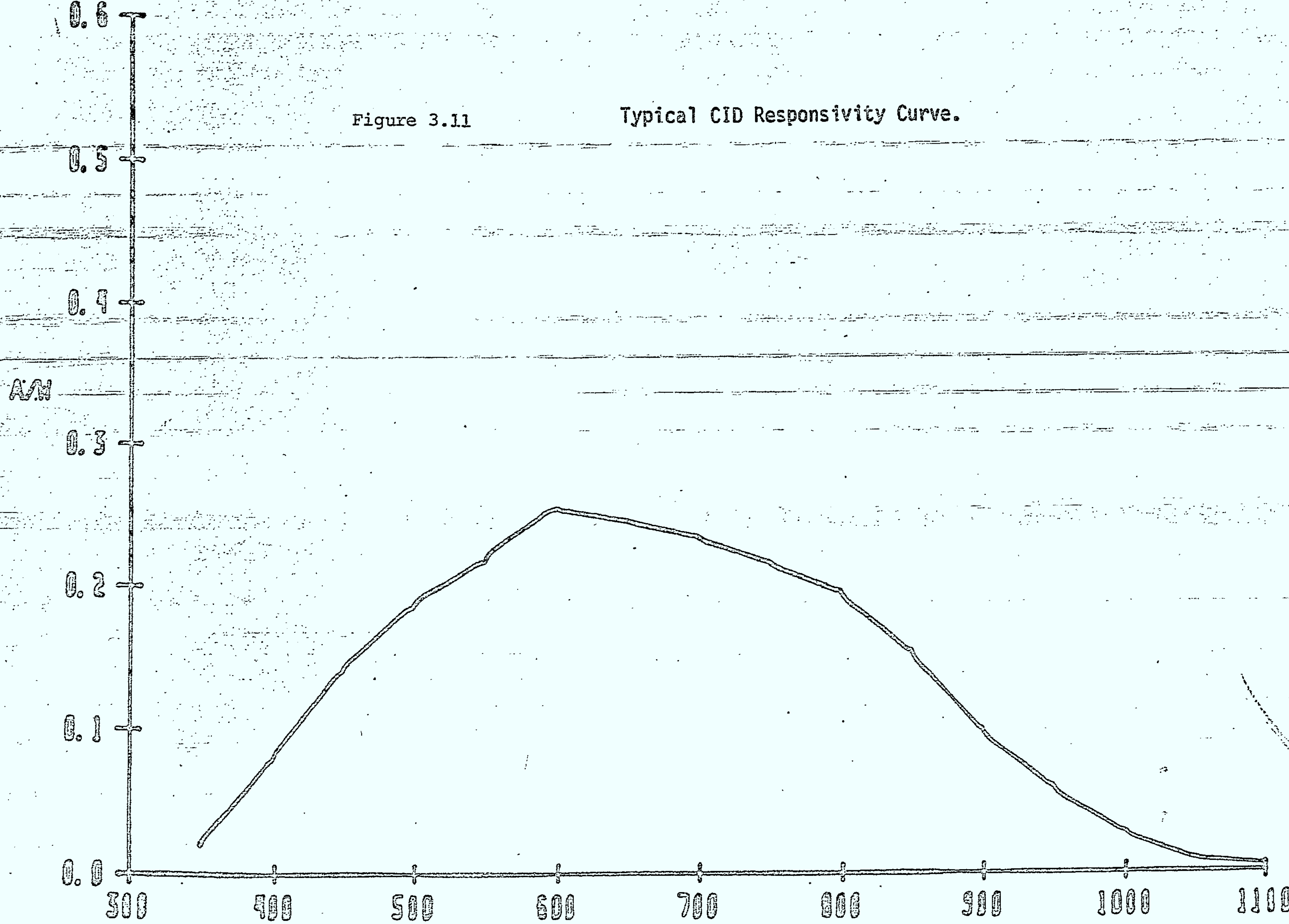

Figure 3.11 Typical CID Responsivity Curve.

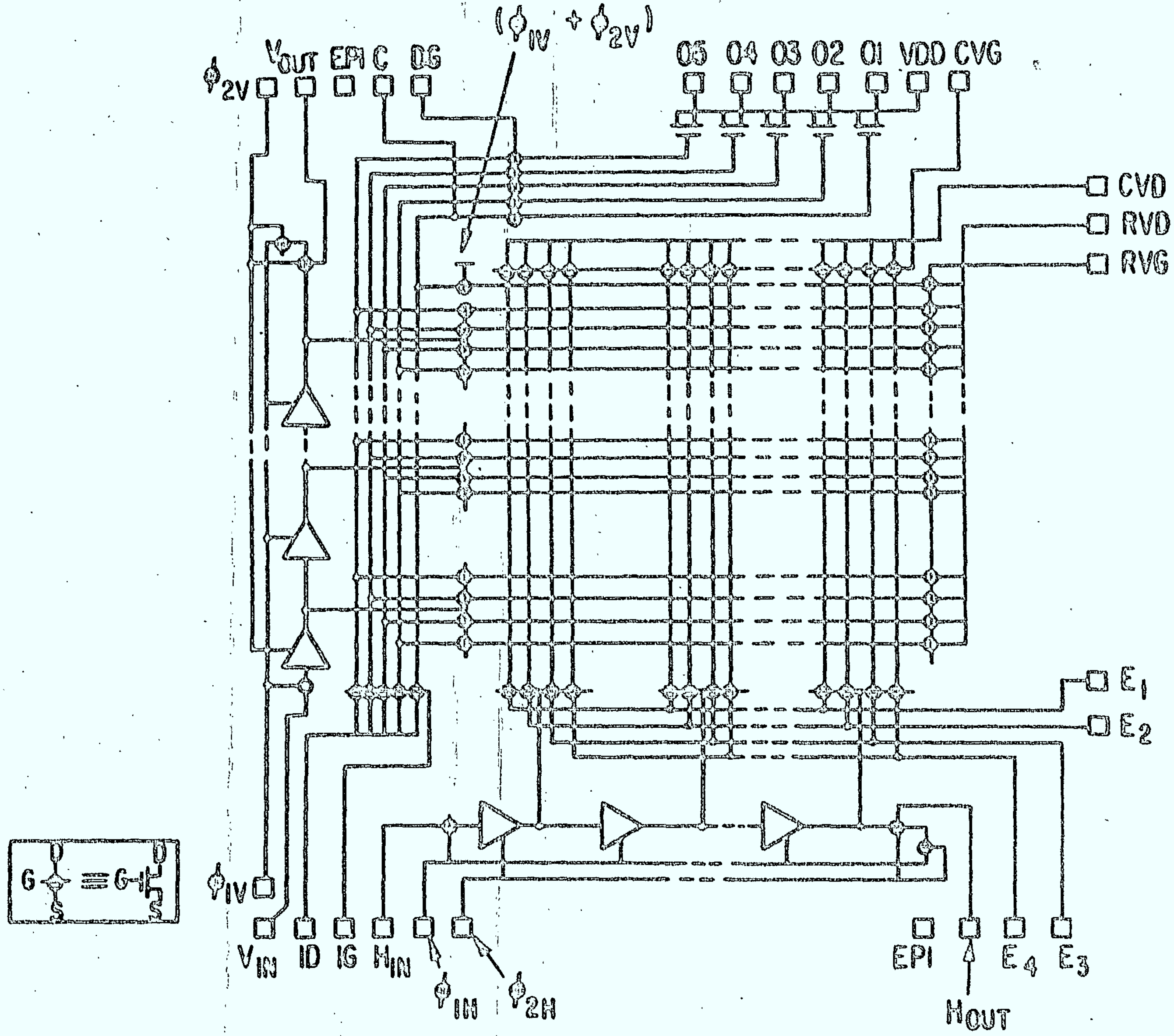

Figure 3.12 Sensor Layout of 128 x 128 array.

- The column and row biases are brought to zero to clear the entire array of stored changes by injection.

- The row bias is set at -8V and the column to -14V for a read enable. The photon generated minority carriers are stored under the column electrode.

- The column and row biases are then floated and the column brought to zero via the E-lines. The collected charge is transferred to the row capacitor, and the displacement current causes a proportional row potential change that is sampled and held for processing.

Returning the column bias to -14V and the row bias to -8V transfers the charge back to the column capacitor and another read cycle can be made. The accumulated charge is not lost and repeating the read process would produce the same output, plus the signal that had been collected during the first read period. This is referred to as the NDRO cycle.

3.9 Availability of CCD's

Texas Instruments has developed two CCD image sensors. These are currently only available as engineering samples, but according to T.I. will be available commercially during 1983. TI will select devices for their customers and are currently developing an integrated clock driver circuit for these image sensors. T.I.'s array are notable because of the virtual phase technology, which enhances the blue responsivity and lowers the dark current.

RCA has the best device as far as quantum efficiency and blue response is concerned. However, RCA has changed their production process and are currently experiencing manufacturing problems. Therefore, there are no devices available at the moment.

EEV (English Electron Valve) is a British manufacturer of commercial devices designed for television use. The biggest drawbacks of these sensors are their 3 phase clocking structure and their poor quantum efficiency in the blue.

3.10 Comparison of CID vs CCD Readout Speed

As an example we can calculate the maximum required video bandwidth for a CID device and a virtual phase CCD image sensor of 390*292 pixels.

For the CCD imager, the maximum vertical clock frequency equals 1.2 MHz and the maximum horizontal clock frequency equals 15 MHz.

The required minimal video bandwidth depends on the minimum integration time and the maximally achieveable vertical and horizontal clock frequencies and can be calculated as follows:

f video(min) =
64/(Tint(min)-292/f0v(max)-(292*390-64)/f0h(max))

where: Tint(min) = minimum integration time
f0v(max) = maximum vertical clock frequency
f0h(max) = maximum horizontal clock frequency.

In the above case:

f video(min) = 29,508 Hz

If we compare this with the required minimum video bandwidth for a CID image sensor, we only would have to examine a total of 64 pixels instead of the complete array. The minimum bandwidth therefore would be:

f video(min) = 64/Tint(min)

In our case:

f video(min) = 6,400 Hz

The CID technology therefore would need a factor of approximately 5 less video bandwidth and therefore generate less Johnson noise in the amplifier. The power consumption in the sensor drive circuitry would have similar constraints. In case of the CCD virtual phase image sensor the maximum power dissipated in the drivers caused by the charging and discharging of the horizontal and vertical clock line capacitances of the image sensor clock times can be calculated as follows:

P = C*fclock*(V**2)

where P = dissipated power
      C = clock line capacitance
      V = clock drive voltage pk-pk amplitude
fclock = clock freqency

In case of the virtual phase CCD imager:

Pvert = Cvert*(Vvert**2)* 2*292/Tint(min)

where Pvert = dissipated power of vertical clock driver
      Cvert = capacitance of vertical clock line
      Vvert = vertical drive voltage pk-pk amplitude
Tint(min) = minimum integration time.

Similar for the horizontal drivers:

Phor = Chor*(Vhor**2)* 292*390/Tint(min)

where Phor = dissipated power of horizontal clock driver
      Chor = capacitance of horizontal clock line
      Vhor = horizontal drive voltage pk-pk amplitude
Tint(min) = minimum integration time

If we look at the total dissipated power in the drivers and assume that the vertical and horizontal drive voltages are the same, then we can calculate the total dissipated power as:

Ptot =(Vdrive**2)*292/Tint(min)*(2*Cvert+390*Chor)

For the virtual phase CCD where Vdrive = 17 volt and Cvert = 7000 pF and Chor = 64 pF and for a minimum integration time of Tint(min) = 10 msec we can calculate the total driver power as:

Ptot = 329 mW.

We cannot do a similar calculation for the CID device, because we do not have the necessary information for the clock line capacitances. Because of the random accessibility of the CID, the effective clock frequency is lower as only 4 groups of 4*4 pixels have to be addressed. Based on this fact the total worst case power dissipation in the drivers is probably less than in the CCD arrangement.

o Readout Mode

The fixed pattern noise can be eliminated by taking two sets of measurements (with different integration characteristics)and subtracting the first from the second.

A typical read process for the CID is illustrated in Figure 3.13. The method employs non-destructive readout; in this case charge continues to integrate while it is sampled N times and is summed to create the first set. Charge is allowed to continue integrating and once again sampled and summed to create a second set. This results in a difference signal that is proportional to N**2. The temporal noise will sum incoherently so that the readout noise contribution for each update is proportional to N . The signal-to-noise ratio is, therefore, proportional to N**1.5.

The overall diagram for operation in the above mode is shown in Figure 3.14 . The double read, subtraction process effectively cancels the unwanted pattern noise. However, the integration time is halved which results in a factor of two signal loss; although this loss is more than recovered by summing the non-destructive readout.

A similar procedure can be used with a CCD by forming two sets of measurements: the first with integration time T and the second with integration time 2T. In this case no improvement in temporal noise results and the integration time is effectively halved.

The subtraction process can be eliminated in applications where the pattern noise is lower than allowed or where system time and processing constraints allows premeasuring and storing the pattern noise for compensation during operation. The second approach is of particular interest in applications where only a small area of the sensor requires high accuracy, since pattern noise from only a few pixels would need to be measured and stored.

3.11 Device Recommendation

Table 3.2 summarizes the important characteristics of CCD's and CID's. We recommend the use of the CID ST-256 because of its demonstrated performance whereas the other devices have performance characteristics which

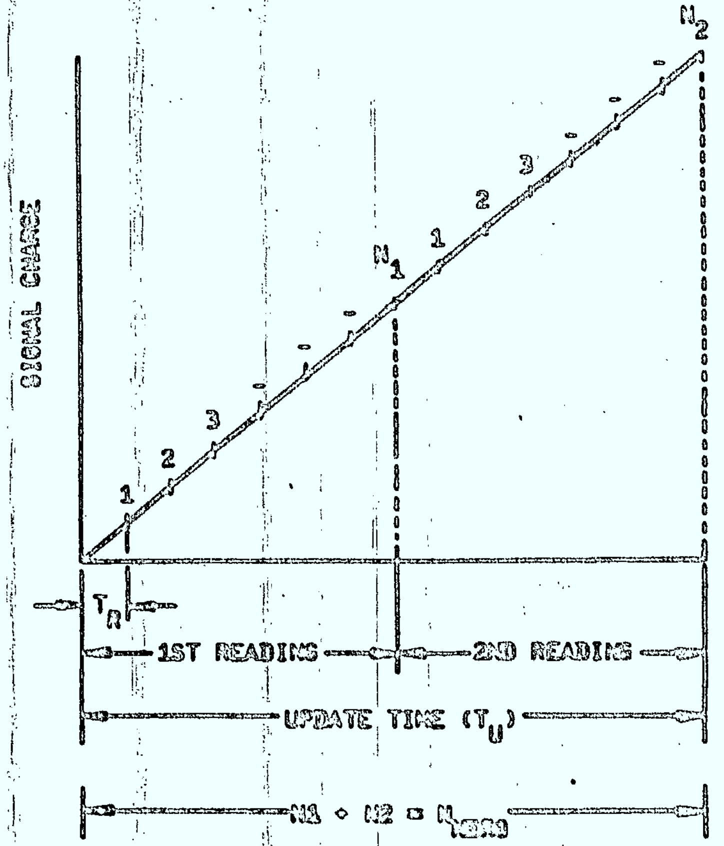

Figure 3.13 Illustration of multiple NDRO process.

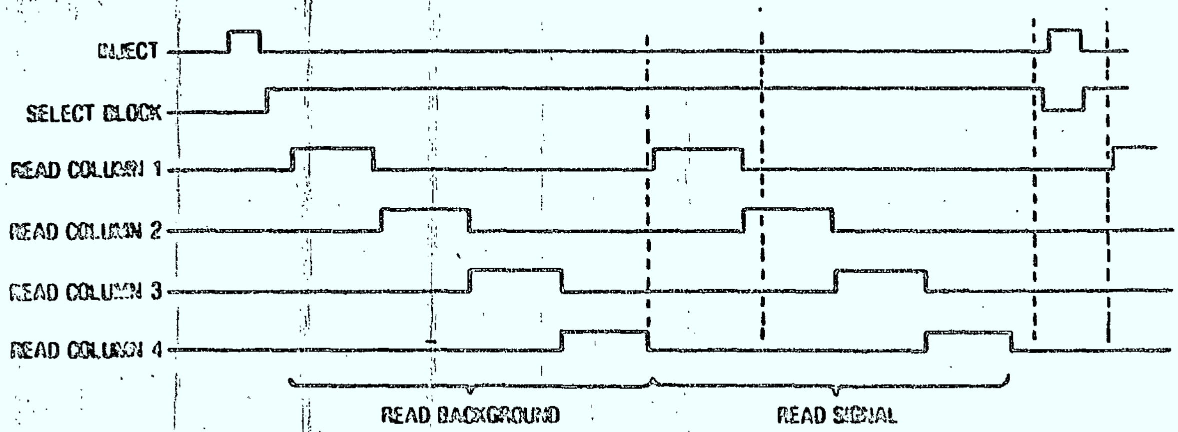

Figure 3.14 Overall Timing Diagram for multiple NDRO process.

Table 3.2 Qualitative Comparison Between CCD & CID Technology

No.	Item	CID	CCD
1	Addressing scheme	Direct x-y access to data pixel	Serial (bucket brigade) access to data pixel
2	Operational Flexibility	Destructive or non-destructive readout	Destructive full frame readout
3	Fabrication	3 masking process	5-12 masking process
4	Charge Storage Capacity	1E6 carriers, typical	5E5 carriers, typical
5	Quantum Efficiency (.4 - 1 micron)	.15 A/W, typical	.36 A/W (RCA) .185 A/W (TI)
6	Dark Current	1 nA/cm2, typical	.4-5 nA/cm2
7	Temporal Noise	30-300 carriers typical	50-200 carriers typical
8	Read Noise	200 carriers, typical (at 10 fr/sec)	60 carriers, typical (at 10 fr/sec)
9	Local Response Uniformity	.5%	1%
	Local Dark Current Uniformity	1%	1%

10	Clock Feed Through	5000 carriers typical	7000 Carriers typical
11	Array Size	256 x 256 typical	328 x 245 typical
12	Pixel Size	20 microns square	24.4 microns square
13	Transfer Inefficiency	One transfer	Full array transferred
14	Optical Overload Tolerance	Blooming confined to local area (10,000:1)	Blooming propagates down column (50:1)
15	Defect Tolerance	Defects confined to adjacent pixel	Defects propagate down column
16	Crosstalk Sensitivity	Confined to adjacent pixel	Occurs over several pixels
17	Radiation Effects	Efficiency of only one transfer is affected	Effects on transfer efficiency propagates down columns
18	Power & Video Bandwidth	Only required pixels are read at required update rate	Full array is read at required update rate
19	Maturity	Implemented in tracker and tested	Implemented in tracker and tested
20	Availability	Custom made	Engineering and commercial samples

are not as well documented. The major characteristic that must be established is the pattern noise. Only limited data however is available. The outstanding difference between the two devices is the anti-blooming characteristic.

3.12 Availability of Integrated Circuits

o Processors

Because of power restrictions in satellite operations it is important to look for low power microprocessors. Therefore, CMOS processors should be our first choice and compatibility with existing NMOS processors would be an asset. The choice between an 8-bit or a 16-bit processor has to be determined by the complexity, speed and the number of calculations that have to be performed.

A prime candidate for the control oriented P.I.C. would be a NSC 800 8-bit processor. This is a CMOS CHIP, manufactured by National Semiconductor which has a typical active power consumption of 50 mW. It has an instruction set of 158 instructions, 10 addressing modes and 22 internal resisters and is available with 1.6 microsec and 1 microsec instruction cycle. Because its instruction set is compatible with the popular 81085 and Z80 processors, it is an ideal candidate. The necessary peripheral circuitry such as RAM, ROM, bidirectional transceivers, bus drivers, etc., are also available in CMOS. This will make it possible to build a full microprocessor system that will consume about 500 mW when running at maximum speed.

A prime candidate for the A.I.M. would be 80C86 16-bit processor. This is a CMOS chip, manufactured by Harris, which has a typical power consumption of 150 mW when running at a maximum clock frequency of 8MHz. The basic instruction set consists of 117 instruction including bit, byte, word and block operations and binary/decimal multiply and divide. A variety of support devices like latching bus drivers, clock generators, bus controllers, programmable interval timers, priority interrupt controllers, programmable peripheral interfaces etc. are also available in CMOS. Because of its compatibility with the NMOS counterpart of Intel (but at 10% of the power consumption), this processor is also an ideal candidate.

The NSC-800 is available in a commercial (0 C to +70 C) and an industrial grade (-40 C to +85 C) and a military version will be announced.

The 80C86 is available in an industrial grade and in the military grade (-55 C to +125 C). Because of the CMOS structure of both processors (and peripheral chips) it should be possible to get radiation hardened versions. Harris (unlike National) is currently a supplier of radiation hardened products (RAM, ROM and linear I.C.s) and it is more probable that they will develop a radiation hardened version microprocessor.

o RAM and ROM

Currently, there is a variety of CMOS RAM, ROM and EPROM available on the market. The Harris HM-6516, e.g. a 2k x 8 CMOS RAM consumes typically 50 mW/MHz and has standby power of 250 microwatts. The Harris HM-6616, e.g. a 2k x 8 CMOS fuse link PROM consumes typically 65 mW/MHz and has a standby power of 500microwatts. It is pin compatible with the industry standard 2716 EPROM. The National Semiconductor NMC 27C32 e.g., a 4k x 8 UV Erasable CMOS PROM consumes typically 5 mW/MHz. It is pin compatible with the industry standard 2732 EPROM.

o Other Digital Circuitry

Currently, there are several manufacturers, (National Semiconductor, Motorola, Fairchild, SPI) delivering LSTTL speed and pin compatible CMOS logic circuitry. This will allow us to build a complete CMOS logic system, that will emphasize the low power requirements of the total system. Again, because it is CMOS, it should be possible to get radiation hardened chips.

o Linear Circuitry

Generally, there is a trade-off between speed and power consumption; linear amplifiers are available with power consumptions from a few milliwatts to several hundred milliwatts. Within this range we expect to find many that can be used in the analog signal processing chain. Harris has several amplifiers of latch up free design that can stand high radiation doses. From a power consumption standpoint of view, it therefore would be preferable to operate the image sensor at the lowest possible readout speed.

o A/D Converters

There is an enormous variety of A/D converters currently on the market. Although there is not a very strong correlation, one could generally make the statement that the better the resolution and the higher the conversion speed, the more the power consumption of the circuit will be. For our requirements, a 12-bit A/D converter looks like the best solution. If we limit ourselves to a 25 microsec conversion time then the power consumption could be held down to about 400 mW.

Increasing the conversion speed to about 3 microsec would double the power consumption. At this stage, we don't have information on radiation hardening possibilities, but because most converters are hybrids, built with bipolar and CMOS circuitry, we do not expect any particular difficulties.

4.0 POSITIONAL AND ANGULAR ERRORS

4.1 Location Estimator

Three different techniques for locating star position across the blur circle (or point spread function) were considered for investigation. The mean and median locators are integral formulations which use all of the data in the blur spot image to define a weighted centroid. The least squares estimator compares the blur spot distribution with an expected distribution and subsequently deduces star position to be some well defined point on the expected distribution when it is aligned with the measured blur spot data.

The mean and median techniques require no apriori knowledge of the blur spot distribution but are dependent on the assumption that the true star position is coincident with the defined centroid. If this assumption were not true then the least squares estimator would be required in order to obtain realistic estimates of star position. However, when the point spread function is reasonably symmetric (as one would expect for star images produced by optical blurring techniques) then the added effort involved in implementing the least squres methodology is not justified.

There is no compelling reason to preferentially select one or the other of the two centroid locators and indeed they both yield the same result for a symmetric function. In addition, one would not expect the least squares locator to be any more precise than the centroids for a simple nearly symmetric point spread function (its advantages would be more evident in the case of a structured function with location information stored in characteristic features such as secondary peaks). We have therefore concentrated our studies on the mean locator under the assumption that this technique is a suitable indicator of location estimator precision. This choice allows for the study of locator sensitivity to the CTD variables and its relation to the noise equivalent angle. It is not expected that these investigations will be significantly affected by more refined information on the point spread function.

4.2 Mean Locator

The mean locator is analogous to the centre of mass calculation in particle system dynamics with the signal induced charge density (point spread function) acting as the weighting function viz,

$$\bar{x} = \int_{-\infty}^{\infty}\int_{-\infty}^{\infty} x\, w(x,y)\, dx\, dy \qquad (4.1a)$$

$$\bar{y} = \int_{-\infty}^{\infty}\int_{-\infty}^{\infty} y\, w(x,y)\, dx\, dy \qquad (4.1b)$$

where w(x,y) is the normalized point spread function whose integral over x and y is unity(if Q is the total induced charge then the charge per unit area or point spread function is simply Q*w(x,y)). Appropriately the mean if taken over the complete point spread function is independent of the origin location and the orientation of the coordinate system. For a symmetric pointspread function the mean occurs at the centre of symmetry.

If the integration over y in the x computation is carried out we obtain

$$\bar{x} = \int_{-\infty}^{\infty} x\, L(x)\, dx \,/\, Q \qquad (4.2)$$

where L(x) (line spread function LSF) represents the cumulative charge in the y direction per unit length in the x direction (for brevity we consider only the x coordinate of the mean, the y coordinate expressions are clearly identical in form). If the sampling intervals are finite the mean calculation becomes the quadrature approximation

$$\begin{aligned} \bar{x}' &= \sum_i x_i \int_{(i-\frac{1}{2})d}^{(i+\frac{1}{2})d} L(x)\, dx \,/\, Q \\ &= d \sum_i i\, q_i \,/\, Q \end{aligned} \qquad (4.3)$$

where d is the pixel width, x = d (pixel centres), and q is the integrated charge in a column of pixels straddling x .

o Interpolation Error

If the translated coordinate X is measured from x then the interpolation error is simply

$$\begin{aligned} E &= \bar{x}' - \bar{x} \\ &= \sum_i X_i \int_{(i-\frac{1}{2})d-\bar{x}}^{(i+\frac{1}{2})d-\bar{x}} L(X)\, dX \,/\, Q \end{aligned}$$

where $$X_i = x_i - \bar{x} = d \cdot i - \bar{x}$$

Letting $$I = i - i_o \qquad (4.4a)$$

and $$\delta = \frac{\bar{x}}{d} - i_o \qquad (4.4b)$$

where i_o is the pixel column containing $\bar{x}$, yields

$$E/d = \sum_I (I-\delta) \int_{\{(I-\frac{1}{2})-\delta\}d}^{\{I+\frac{1}{2}-\delta\}d} L(X)\,dX / Q$$

$$= \sum_I \int_{\{I-\frac{1}{2}-\delta\}d}^{\{I+\frac{1}{2}-\delta\}d} L(X)\,dX/Q - \delta \qquad (4.5)$$

If L(X) is symmetrical then the integrals in can be folded about X=0 on to the positive half of the X axis. Furthermore the overlapping of the resulting integrals reduces the error expression to

$$E/d = \sum_{i>0} \int_{(i-\frac{1}{2}-\delta)d}^{(i-\frac{1}{2}+\delta)d} L(X)\,dX/Q \qquad (4.6)$$

This function satisfies certain basic properties of the interpolation error. If x is at the centre or edge of a pixel (δ =0 or $\pm$ 1/2) then the symmetry of L(X) ensures x will be located at the same point. Since there is no distinction (except sign) between the cases when x is a distance / δ / from the pixel centre it is expected that the function is odd in δ = [-1/2,1/2]. Lastly the periodicity of the pixel structure requires that the function be periodic from pixel to pixel. Note that the error is not necessarily peaked or symmetric about δ = 1/4. For example a point spread function which tends towards a delta function (the case of non blurring Gaussian optics) produces a sawtooth error curve versus (vertices at $\delta = \pm 1/2$).

An alternate and useful form of equation 4.6 is the Taylor series expansion

$$E/d = \left(\frac{Q^*}{Q}-1\right)\delta + \frac{Q^*_{(2)}}{Q}\frac{\delta^3}{3!} + \frac{Q^*_{(4)}}{Q}\frac{\delta^5}{5!} + \ldots \qquad (4.7)$$

where $$Q^* = 2d \sum_{k>0} L[(2k-1)d/2]$$

and $Q^*_{(n)}$ is the nth derivative of Q*(dz) with respect to z.

o Interpolation Error and Truncation Error

The results of the previous section were based on the assumption that the entire area of the point spread function was sampled. In practical applications this will not be so and hence additional error will result because of truncation in the mean computation. The combination of interpolation plus truncation error can be written as (for a symmetric point spread function)

$$E/d = \frac{1}{Q'} \sum_{i=1}^{(N-1)/2} \int_{(i-\frac{1}{2}-\delta)d}^{(i-\frac{1}{2}+\delta)d} L'(x)dx - \frac{(N-1)}{2Q'} \int_{(\frac{N}{2}-\delta)d}^{(\frac{N}{2}+\delta)d} L'(x)dx - \delta \qquad (4.8a)\ (N\ \text{odd})$$

$$= \frac{1}{Q'} \sum_{i=1}^{N/2} \int_{(i-\frac{1}{2}-\delta)d}^{(i-\frac{1}{2}+\delta)d} L'(x)dx + \frac{N}{2Q'} \int_{(\frac{N+1}{2}+\delta)d}^{(\frac{N+3}{2}-\delta)d} L'(x)dx - \delta \qquad (4.8b)\ (N\ \text{even})$$

where it is assumed that x is within 1/2 pixel of the truncated point spread function. Q and L'(x) represent the truncated integrations for total charge and line spread function respectively and N is the total number of pixel columns in the x direction. (See Fig.4.1). We are again only providing derivations for the x direction, the y coordinate derivations being similar in form. It is also noted that if L(x) is symmetric then L'(x) will also be symmetric. In the case where the point spread function is separable into product functions of x and y the error computations in each direction are independent of truncation in the perpendicular direction.

Equations (4.8a) and (4.8b) were analyzed for the specific case of a Gaussian point spread function given by

$$P(X,Y) = e^{-Y^2/2\sigma_Y^2} \cdot e^{-X^2/2\sigma_X^2} \qquad (4.9)$$

The relevant parameterization is in terms of the standard deviation σ, of the Gaussian point spread function and d the pixel dimension. The blur diameter (full width at half maximum) of the point spread function is ~ 2.35*σ.

The results for 2 and 3 pixel columns in the x direction are plotted in Figure 4.2 and Figure 4.3 (note that δ is taken from the geometric centre in the

Figure 4.1 Point spread function and the sampling window (eq. 4.8)

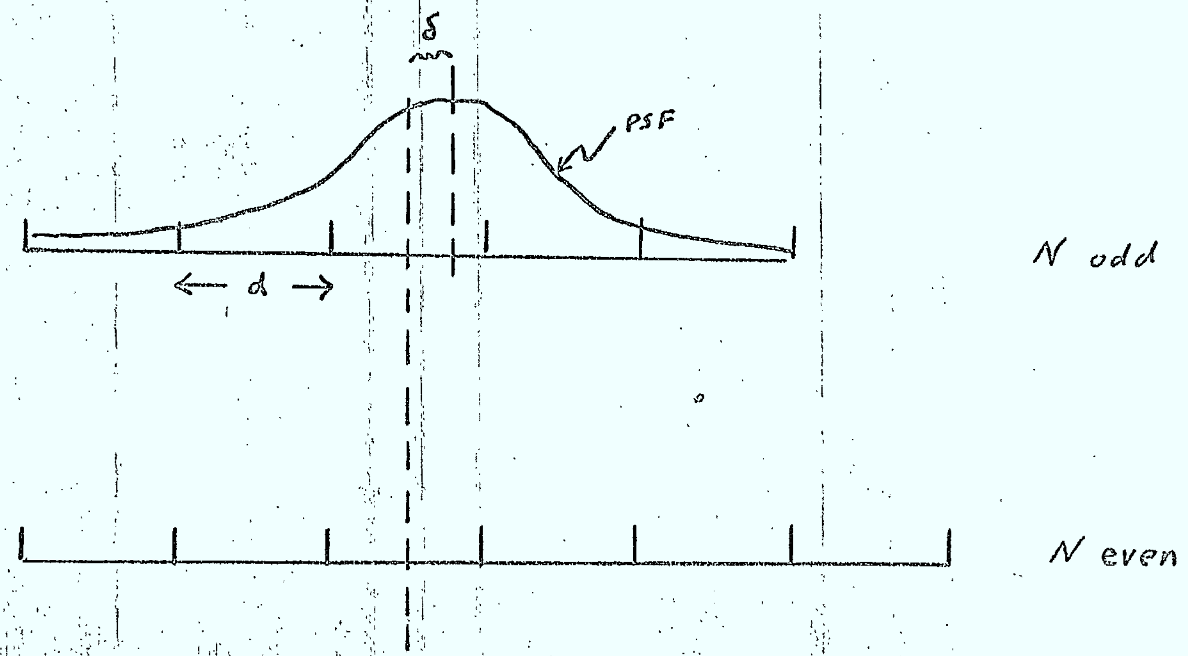

case N=2 as opposed to the definition given in equation 4.4b. The function is odd about the origin and has the periodicity of the array. The figure can, therefore, be confined to the range 0 to 0.5. Implicit in the calculation is the assumption that the centre of the image can be estimated within a given pixel by other techniques (e.g. a priori knowledge, thresholding, or by finding the pixel with the largest signal).

Two limiting cases can be distinguished which are typical of the error variation in general. If the pixel diameter d is not large compared to the width of the line spread function (measured as the standard deviation σ) then the mean calculation becomes somewhat insensitive to the position of the centre of symmetry. This lack of sensitivity implies that the calculated mean lags behind the true mean as the true mean is moved in a particular direction. Thus for small d/σ the sign of the error in Figures 4.2 and 4.3 is positive or negative depending on whether the true mean is on the positive or negative side of the geometric centre. In the limit as d becomes very small the fraction of the point spread function which is actually sampled appears flat so that the computed mean is the geometric centre of the sampling window and the error is simply the displacement between the centre of symmetry and the sampling window centre ($E/d \rightarrow -\delta$).

At large pixel diameters truncation is no longer a problem (i.e. the sampling window collects charge from that region of the point spread function which dominates the mean calculation) and the antisymmetric interpolation error discussed above dominates.

The error will always decrease as the number of pixels in the sampling window are increased. However, an increase above a sampling window diameter of 2 or 3 pixels is unacceptable given the rapid increase of noise equivalent angle with pixel number in CCD arrays. One must therefore look to optimizing d/σ (i.e. varying the point spread function width in the optical design stage) in order to reduce the combined interpolation/truncation error. Figure 4.4 shows the dependency of the error on d/σ for a 3 pixel column wide sampling window at $\delta = 1/4$. It is evident that a minimum in the neighbourhood of d/σ = 2.5 exists intermediate to the truncation and interpolation

Figure 4.2 Interpolation/Truncation Error for 2 Pixel Wide Sampling Window

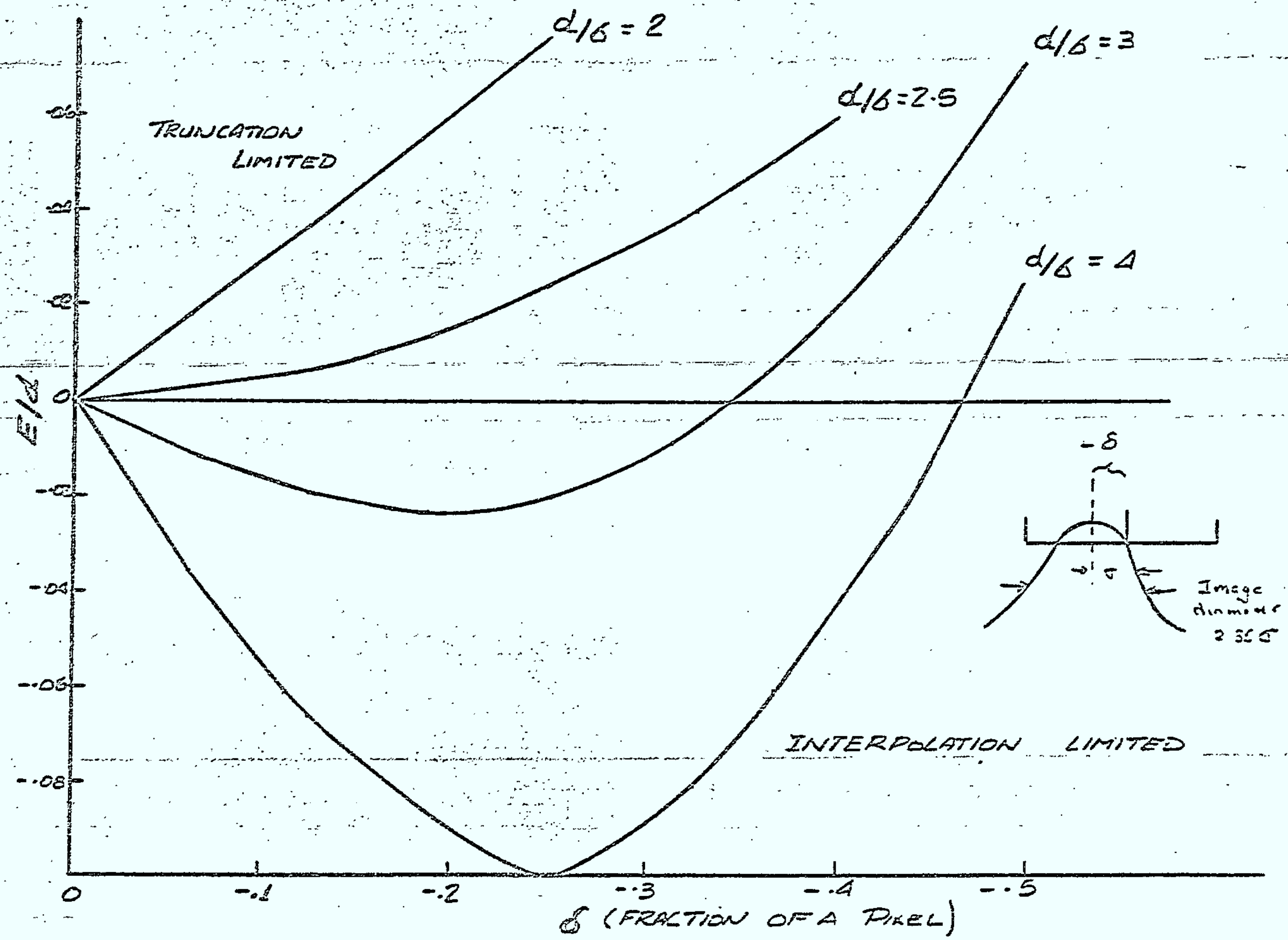

Figure 4.3 INTERPOLATION/TRUNCATION ERROR FOR 3 PIXEL WIDE INTERPOLATION WINDOW

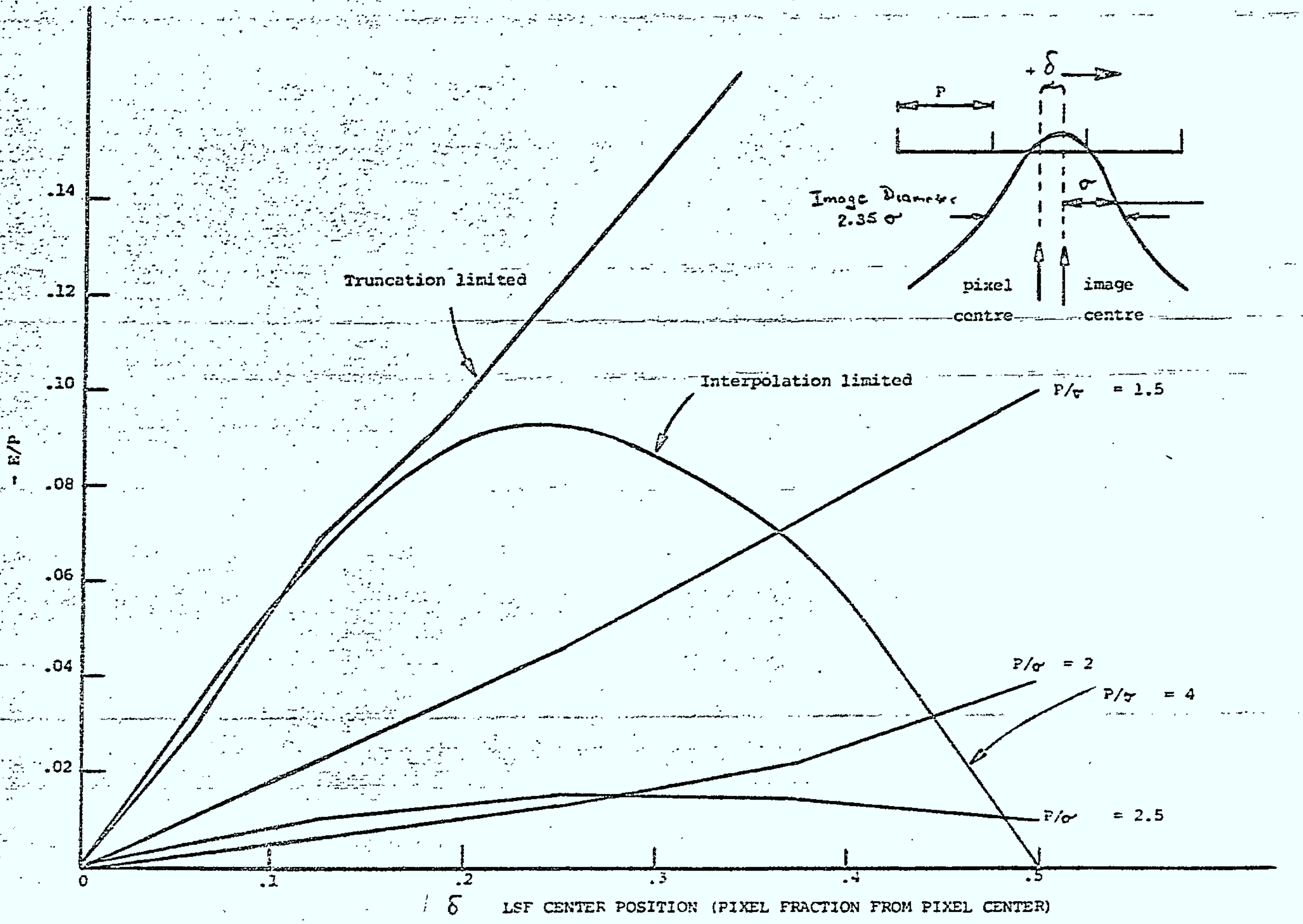

Figure 4.4

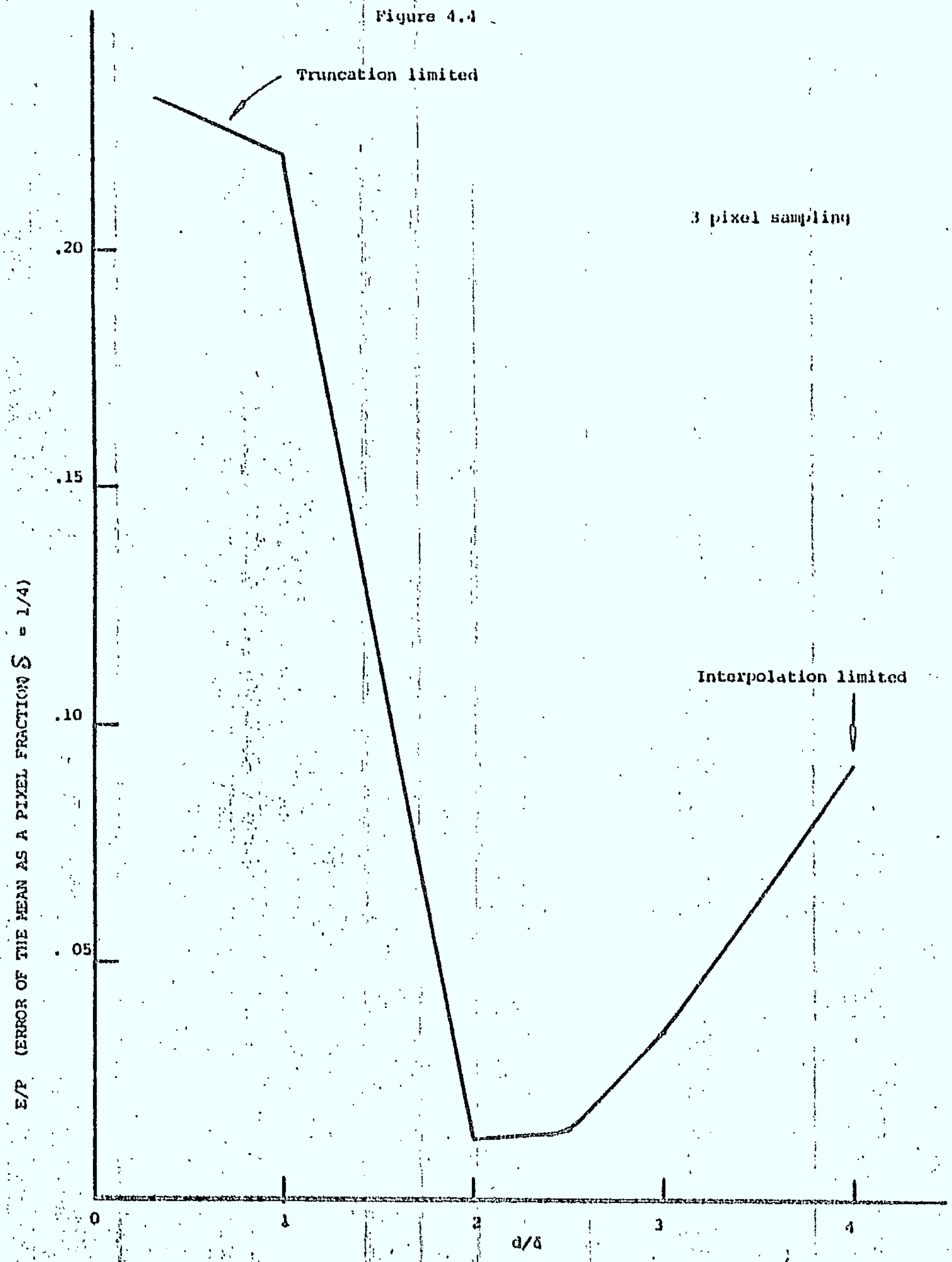
Truncation limited
3 pixel sampling
Interpolation limited
E/P (ERROR OF THE MEAN AS A PIXEL FRACTION δ = 1/4)
.20
.15
.10
.05
0
1
2
3
4
d/δ

limited regions. Furthermore, the approximate linearity of the error (Fig.4.3) for values of $2.0 < d/\sigma < 2.5$ suggests that the interpolation/truncation error can be reduced even further by applying a simple bias corrector to the computed point spread centre.

o Blur Spot Motion

The problem of blur spot motion due to attitude changes can be simply formulated as a change in the standard deviation of the point spread function. Consider the case of a symmetric point spread function moving with velocity V in some direction on the x,y plane. Let the x,y coordinate system be translated and rotated to an x',y' system whose origin is at the centre of symmetry at t=o and whose x' axis points in the direction of motion. Then the charge collected in area element dxdy over time dt is given by

$$dQ = Q\dot{w}(x'-vt, y')\,dt\,dx\,dy$$

where the integration of $\dot{w}$ over space and time is unity. The contribution per unit area at a given point over an integration time T (i.e. the cumulative point spread function) is

$$P(x', y') = Q\int_0^T \dot{w}(x'-vt, y')\,dt$$

$$= \frac{Q}{V}\int_{x'-VT}^{x'} \dot{w}(X', y')\,dX' \quad (4.11)$$

where $X' = x'-vt$. This expression (which represents a convolution of the instantaneous point spread function with a flat pillbox extending from $-VT/2$ to $VT/2$; see Figure 4.5) is symmetric about $x' = VT/2$ as can be seen if we reformulate the limits in terms of $X' = x'-VT/2$ viz.

$$P(X', y') = \frac{Q}{V}\int_{X'-\frac{VT}{2}}^{X'+\frac{VT}{2}} \dot{w}(X', y')\,dX' \quad (4.12)$$

$$= P(-X', y')$$

where the symmetry condition is of course dependent on $w(X'', y')$ being symmetric.

Figure 4.5 Blur Spot Motion

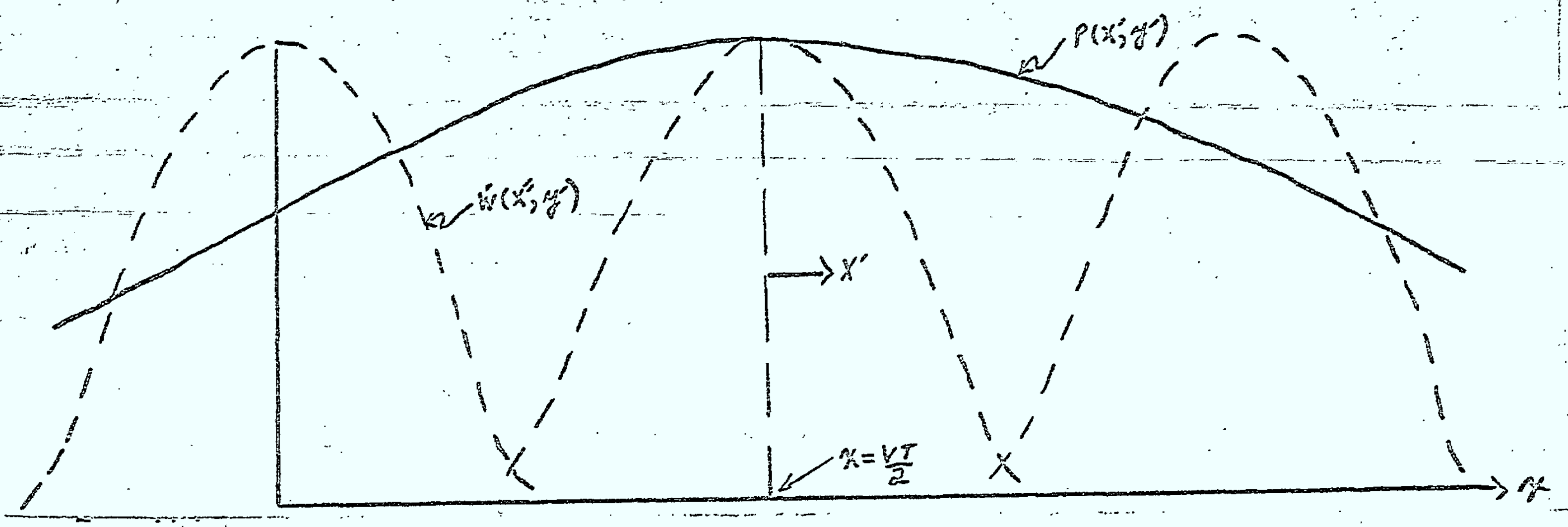

For this expression one can show that in the X′ direction

$$\sigma_p^2 = \sigma_{\dot{v}}^2 + (VT)^2/12 \qquad (4.13)$$

where σ_p is the standard deviation of the velocity dependent point spread function, $\sigma_{\dot{v}}$ is the standard deviation of the instantaneous point spread function and $VT/\sqrt{12}$ is simply the standard deviation of a flat pillbox extending from $-VT/2$ to $VT/2$. The impact of equation 4.13 is that it enables us to utilize the results of the previous section provided the velocity induced changes in the standard deviation are accounted for.

The largest change in standard deviation (with respect to the x coordinate) occurs if the velocity vector is aligned with the original CCD x axis. If we examine Figure 4.4 we note that the minimum in E/d is located in the range of d/σ between 2 and 2.5. For this range we have from equation 4.13

$$\frac{VT}{d} \cong \frac{\sqrt{24\Delta\sigma/\sigma}}{(d/\sigma)} \cong \frac{\sqrt{24\,\Delta(d/\sigma)/(d/\sigma)}}{(d/\sigma)}$$

Thus for d/σ ~ 2.5, this implies that motion blur should be limited to .88 pixels between updates.

4.3 Development of a Noise Model

There are two components in a noise model of a startracker. The first component describes the startracker performance and relates the noise equivalent angle to the performance characteristics of the imager. The second component extracts those characteristics of the array to allow calculation of the detector signal-to-noise ratio.

Star tracker performance can be characterized by the random error in the image locator. Our modelling has been confined to the mean locator for the reasons described above.

Dark current affects the measurements of star position by moving the apparent centroid away from the true position toward the centre of the track window. If the average dark current is measured and subtracted only spatial variations affect the centroid. To avoid errors of measurement the temporal noise on any pixel should be reduced by increasing the integration time to bring the dark signal up to approximately 1/2 full well. The average dark current per pixel can then be computed. Alternatively the dark current for each pixel can be stored and used to correct the star data. This is feasible for well defined areas of the array(e.g. the track window) provided these areas do not change frequently. A tabulation of noisy pixels should be made thus allowing defects to be identified and ignored. Dark current contributes shot noise and the spatial variation of the dark current causes a random error in the centroid.

Table 3.1 above is a comparison of the general characteristics of CTD's. Of the indicated parameters, the random noise model is most sensitive to pattern noise. Fixed pattern noise usually refers to the spatial variation of the video signal when the CTD is in the dark. Occasionally some authors will refer to the fixed pattern noise in the highlight portion of the image. We have referred to this noise term as responsivity variation to distinguish the two terms.

Our model assumes measurement and subtraction of the average dark current; this scenario is realistic because it requires a modest video buffer. A discrete model is assumed, viz,

$$\bar{P}_x = \frac{\sum_{n,p} p(I_{p,n} - \bar{i}\tau)}{\sum_{n,p} (I_{p,n} - \bar{i}\tau)}$$

where $\bar{P}_x$ is the centroid in the x-direction corresponding to the summation over p; n corresponds to summation over the y-direction; $I_{p,n}$ represents the measured charge at each photosite; $\bar{i}$ is the average dark current and τ is the integration time.

The measured charge at the photosite can be written,

$$I_{p,n} = G_{p,n} \omega_{p,n} Q + i_{p,n} \tau + R(t)$$

where R(t) describes the sampled read noise (temporal noise such as amplifier, clocking noise etc.) and has zero mean, $i_{p,n}$ represents the dark current at a given photosite with mean $\bar{i}$, $G_{p,n}$ represents the variation in responsivity and without loss of generality is assumed to have a mean of 1. Q represents the total photocharge associated with a given star and $w_{p,n}$ describes the fraction of the point spread function w(x,y) which is collected by pixel p,n

i.e.

$$w_{p,n} = \int_{(p-1/2)d}^{(p+1/2)d} \int_{(n-1/2)d}^{(n+1/2)d} w(x-x_0, y-y_0)\, dx\, dy$$

where x_0, y_0 define the centre of the star image.

Assuming uncorrelated random variables we can evaluate the r.m.s. error $\sigma(P)$ in the pixel position and relate it to

$\sigma(G)$ the r.m.s. variation in responsivity

f the fractional spatial variation in the dark current

$\sigma(R)$ the r.m.s. read noise

We further assume there is a Poisson statistic for sensing charge which causes shot noise in both the signal and dark current.

We obtain the following results:

$$\sigma^2(P) = A\,\sigma^2(G) + \frac{B}{Q} + \frac{C}{Q^2}\left\{ f^2 \bar{i}^2 \tau^2 + \sigma^2(R) + \bar{i}\tau \right\}$$

The quantities A, B and C are given by

$$A = \sum_{p,n} (p - \bar{P}_x)^2 \omega_{p,n}^2 / K^2$$

$$B = \sum_{p,n} (p - \bar{P}_x)^2 \omega_{p,n} / K^2$$

$$C = \sum_{p,n} (p - \bar{P}_x)^2 / K^2$$

and

$$K = \sum \omega_{p,n}$$

The first three terms describe the respective contribution of the spatial variation in responsivity, the shot noise in the signal and the combined contribution of dark current shot noise, spatial noise due to dark current variation and read noise. Since the mean dark current is an average over all pixels its measurement error is negligible compared to all other terms.

Note that all summations are over a track window of N x N pixels centred about an estimate ($\hat{P}_x$, $\hat{P}_y$) of the centroid ($\bar{P}_x$, $\bar{P}_y$). This means that the coefficients A, B, C are only functions of $\delta_x = \bar{P}_x - \hat{P}_x$

and $\delta_y = \bar{P}_y - \hat{P}_y$

The quantity, K, describes the fraction of the point spread function that is collected within the track window.

The quantities A,B,C have been evaluated for a Gaussian point spread. Furthermore, we have assumed that $|\delta| \leq 0.5$ This latter requirement has been addressed in the discussion of systematic error. From a mathematical point of view a two dimensional Gaussian,

$\exp(-(x^2 + y^2)/2\ \ )$, has the advantage of being both circularly symmetric (as one expects from the optical system) and separable along two perpendicular directions. The value of A,B vary considerably and are best described by an upper bound. C can be evaluated directly.

$$C = \left\{ 2N \sum_{1}^{[\frac{N}{2}+1]} p^2 + N\delta^2 \right\} / K^2$$

where $[\frac{N}{2}+1]$ is the integral part of N/2 +1. For a well defined spot and a matched track window, we can ensure that K is greater than 0.8; C therefore increases rather dramatically with N taking the following minimum values 1, 6, 20, 50 for N = 2,3,4,5.

Of the three quantities the last term dominates all noise processes since A and B are less than 1. While a track window 2 pixels wide gives a smaller random error than a 3 pixel window, the systematic error is rather larger. Consequently, a three pixel window has been used. The upper values for A,B and C are 0.11, 0.16 and 8.6 respectively.

4.4 Application of the Noise Model

A noise model has been applied to three devices: the GE Electric CID, the RCA CCD and the TI virtual phase CCD. These devices have been selected because they represent three technological classes - the random access charge injection device, a thinned backside illuminated three phase charge coupled device and a front side illuminated virtual phase device. Figure 4.6 estimates the random error (fraction of a pixel) versus dark current for the three devices at infinite integration time ($\tau = \infty$). While the RCA device has the

Figure 4.6 Device Comparison

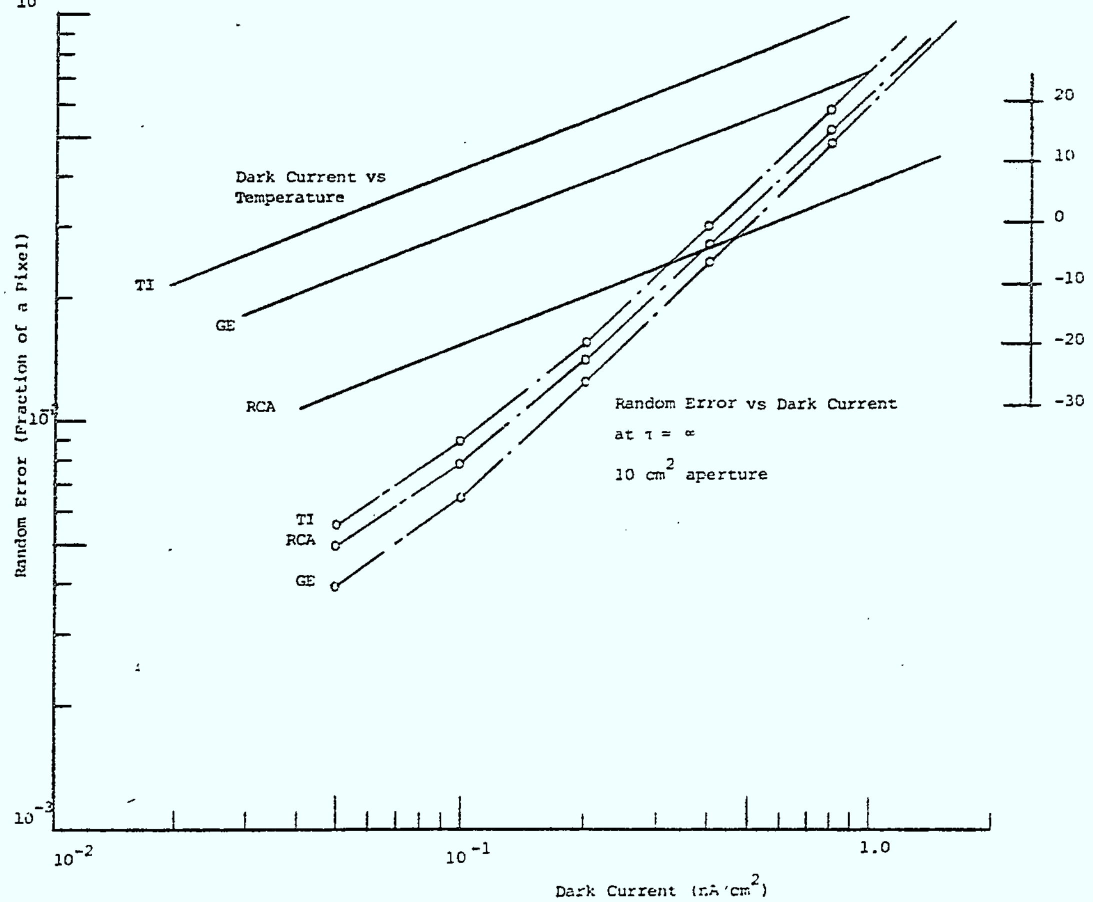

largest responsivity, the large pixel area (30 x 30 microns) implies a greater dark current contribution than the other devices. In addition, the RCA device requires lower operating temperature to achieve this result. The responsivity, pixel size and dark current for the GE and TI devices are comparable - apperently CID's have been manufactured with room temperature (25C) dark currents in the range of 0.4 - 4 nA/cm**2 while the TI device is reported to operate at 0.4 nA/cm**2 .However, the GE CID exhibits smaller variations in the responsivity which accounts for its improved performance.

Further comparison of devices has been confined to the GE CID and TI virtual phase device since the RCA device is generally poorer than the other two because of the larger dark current at a given operating temperature. As noted above, apart from the responsivity variations, the GE and TI devices are similar; consequently, the GE device shows an improvement of approximately 1.4 in the noise equivalent angle when the two devices are operated at high signal to noise ratio where responsivity variations dominate the noise equivalent angle.

The fixed pattern noise has been modelled as if there are two dominant components clocking noise and variations in the dark current. The model parameters that have been assumed are given in Table 4.1 .

Table 4.1 Model Parameters

Dark Current		4 E03 e/sec
Fractional Variation in Dark Current		1%
Residual Clocking Noise		70 e's
Amplifier Noise		20 e's
Star Signal (Magnitude 6)		1.5 E03 electrons/sec- cm^2
Local Responsivity Variation	TI	1%
	GE	0.5%

Many of these parameters cannot be determined from available data. In particular, the CCD systems indicated that the clocking noise is approximately 7000 e's before any attempt at suppression. We have assumed that the use of a correlated double sampler can reduce this to 70 e's. There is data for the GE device, however, this data is obtained after digital signal processing (Double read non-destructive readout). This technique has yielded similar values of combined temporal and fixed pattern noise.

The GE reports indicated that below 0 degrees C the Johnson noise term dominates the dark current. However, our model is not very sensitive to the noise source but only to the total noise.

Figure 4.7 illustrates the variation of signal-to-noise ratio with lens area for two different focal length lenses. The calculations for a magnitude 6 star shows that for a given dark current there is a maximum integration time beyond which there are no practical increases in signal-to-noise ratio. These graphs illustrate that a design which calls for a 1 arc second noise equivalent angle requires a signal-to-noise ratio of 280 for a 50 mm lens; this signal-to-noise implies an integration time of approximately 10 sec and an aperture of f/1.4. To make use of the difference between the TI and GE devices requires a reduction in the dark current by a factor of approximately 2.3 for the f/1.4 lens.

Figure 4.8 illustrates the noise equivalent angle versus integration time for a magnitude 6 star for both 25 and 50 mm lenses. The asymptotic behaviour at long integration times is clearly shown. With the additional use of large aperture lenses the GE device shows superiority. Note that the systematic errors at the 1 and 2% level indicated at the left of the graphs imply an equal distribution of the systematic and random errors for f/1.4 lenses.

Figure 4.9 illustrates the integration required to yield noise equivalent angles of 0.5 and 1 arc seconds using different lenses and apertures. The results are plotted for stars of different magnitude. Note that decreasing the temperature of the CTD allows operation at longer integration time. For all integration times less than 50 seconds, dark current does not cause saturation of the array at either temperature.

Figure 4.7

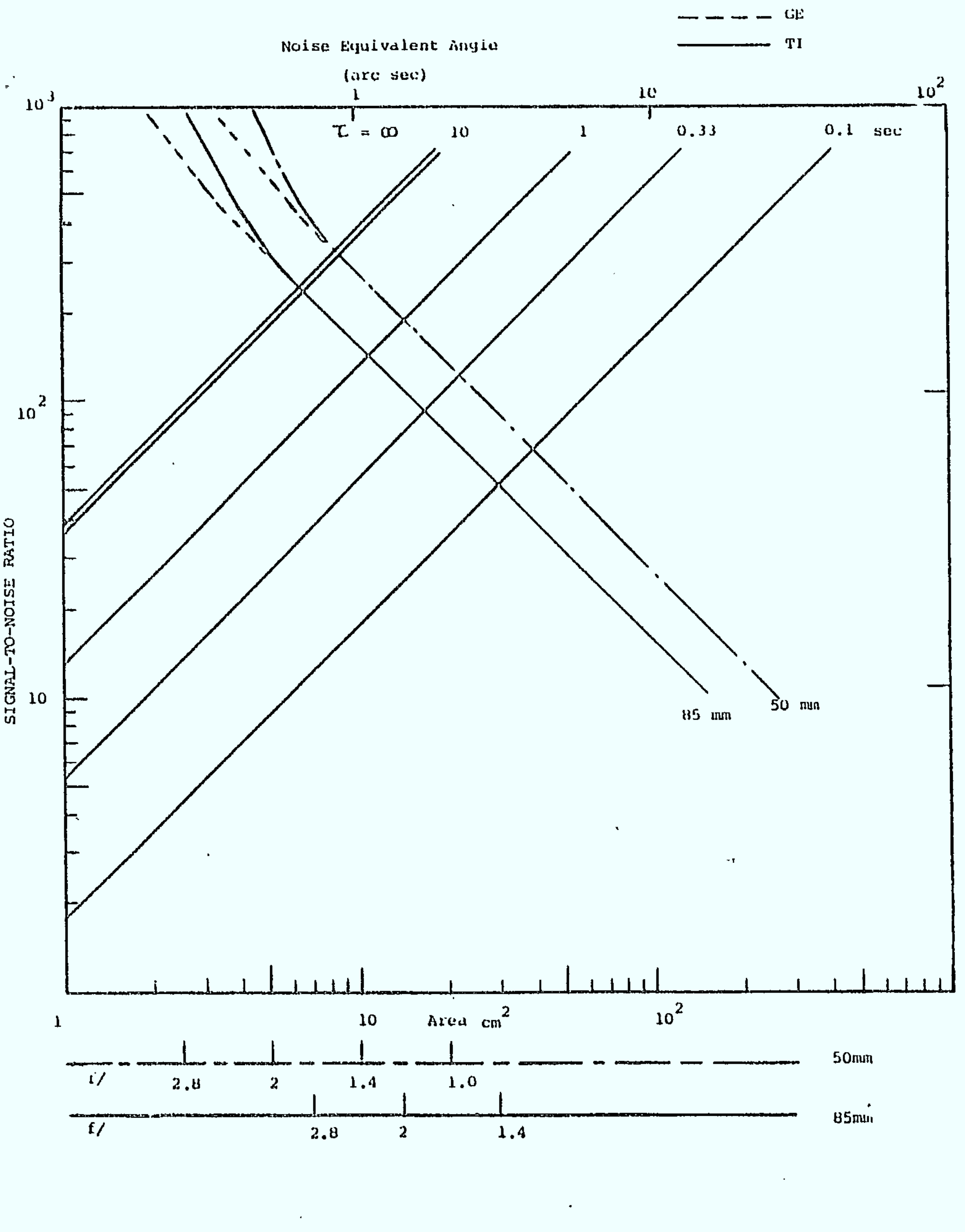
GE
TI
Noise Equivalent Angle
(arc sec)
1
10
10^2
10^3
$\tau = \infty$
10
1
0.33
0.1 sec
10^2
10
SIGNAL-TO-NOISE RATIO
85 mm
50 mm
1
10
Area cm^2
10^2
f/
2.8
2
1.4
1.0
50mm
f/
2.8
2
1.4
85mm

FIGURE 4.8 NOISE EQUIVALENT ANGLE vs INTEGRATION TIME

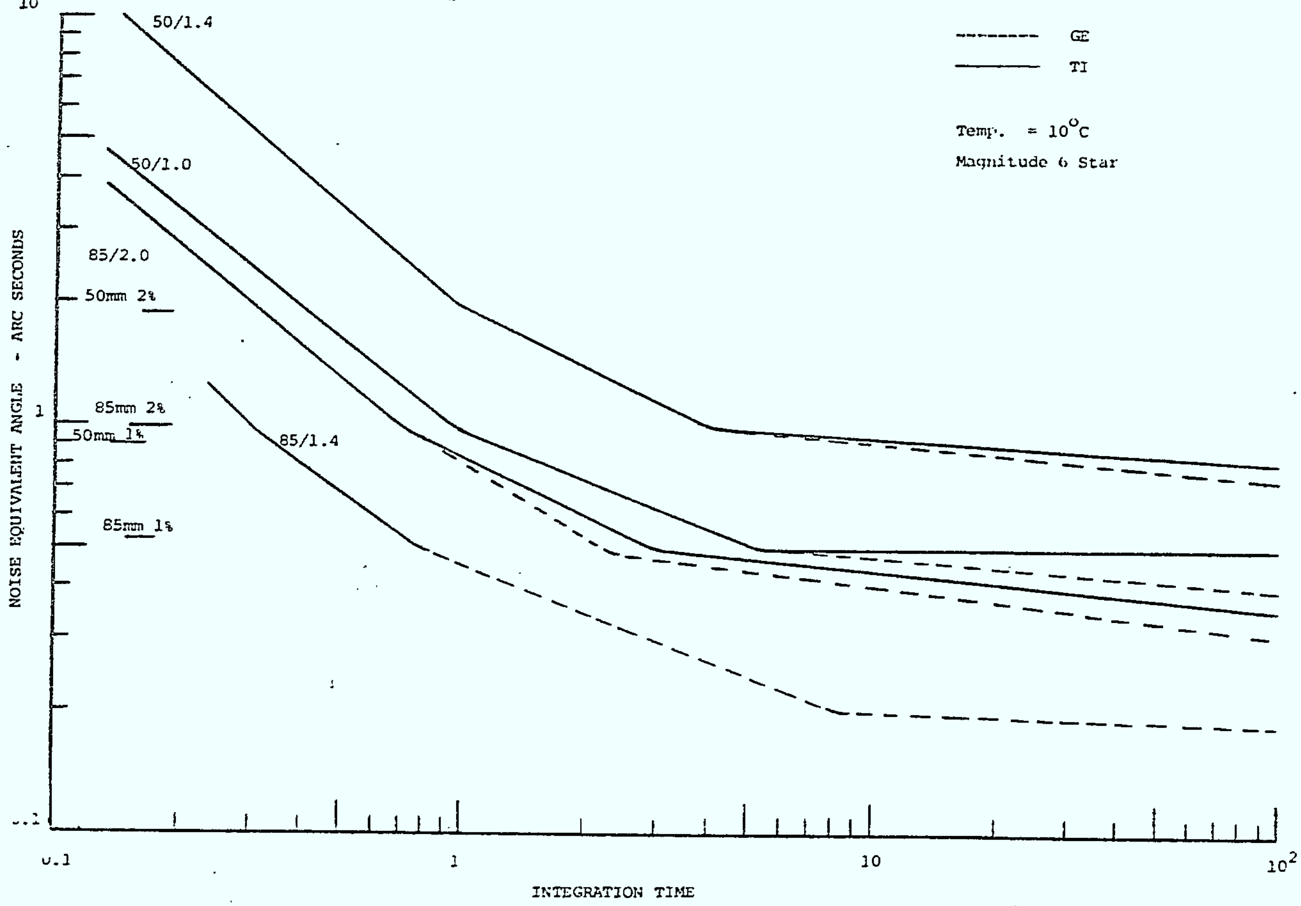

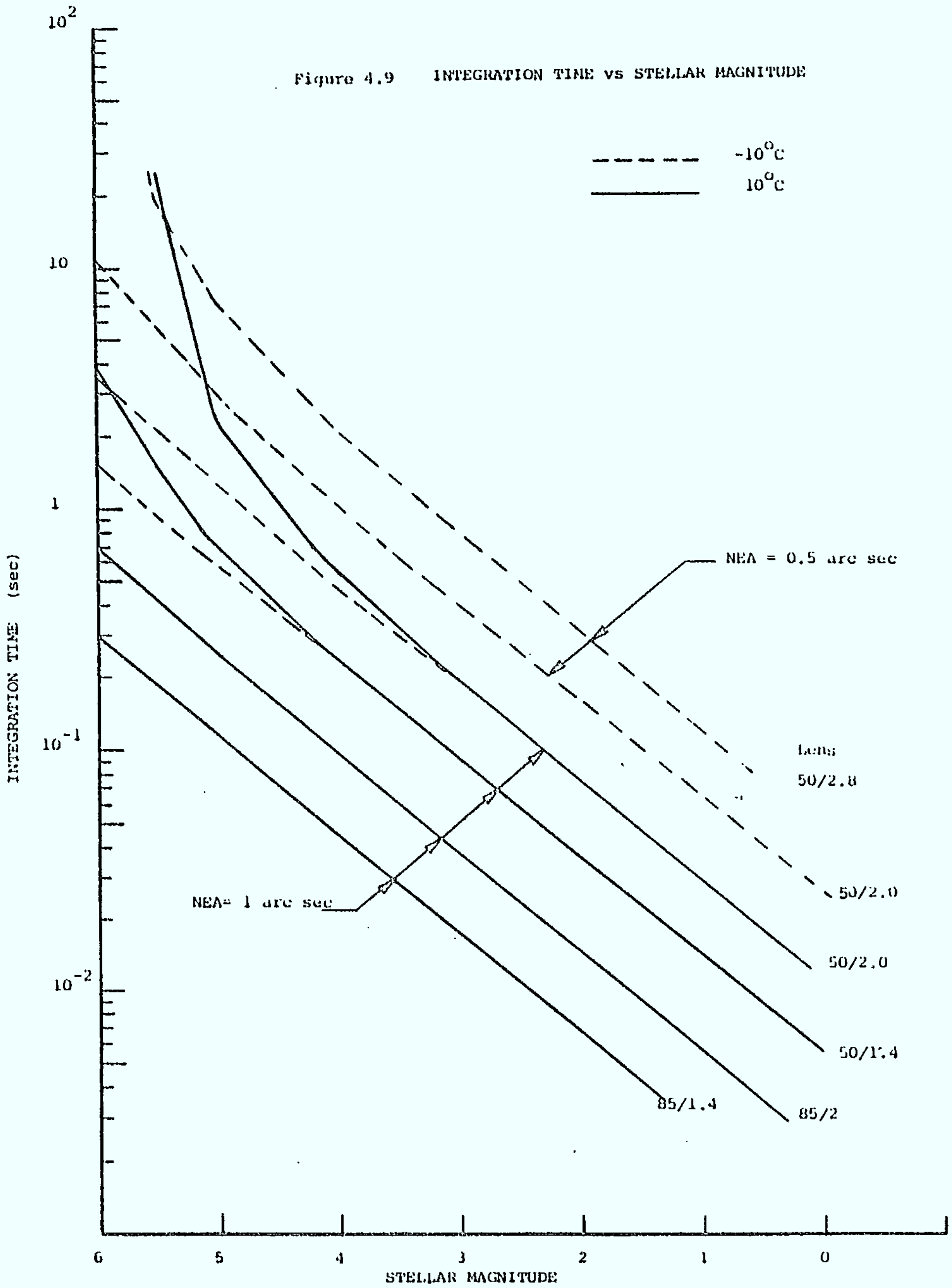

Figure 4.9 INTEGRATION TIME vs STELLAR MAGNITUDE
-10°C
10°C
NEA = 0.5 arc sec
NEA= 1 arc sec
Lens
50/2.8
50/2.0
50/2.0
50/1.4
85/1.4
85/2
INTEGRATION TIME (sec)
STELLAR MAGNITUDE
10^2
10
1
10^-1
10^-2
6
5
4
3
2
1
0

6   Update Time Strategies

We can consolidate the discussion of systematic and random error to evolve an update strategy. The minimum noise equivalent angle should not exceed residual systematic error. This limitation of 1 - 2 % interpolation error sets the lower limit on the noise equivalent angle, and therefore the maximum integration time for a given lens.

Since 1 - 2 % interpolation error corresponds to signal-to-noise ratios of 293 and 147 respectively, we note that attempting to achieve large signal-to-noise ratios, S/N, is not fruitful. As indicated above, the low signal-to-noise ratios that are required essentially imply that

$$A\,\phi^2(\theta),\ B/Q \ll C/(S/N)$$

so that the latter term is dominant. Furthermore, having noted that the signal-to-noise ratio tends to a limit

$$(S/N)_{inf} = eA/fi$$

where
- e is the photocurrent/area from a given star
- A is the lens area
- i is the average dark current
- f is the fractional variation in dark current due to spatial variation

We can adopt an update strategy by settling for

$$S/N = (S/N)_{inf}/M$$

where M is approximately 2; this value determines the maximum useful integration time. The result of this computation is

$$\tau = \frac{1}{2f^2(M^2-1)}\left\{1 + \sqrt{1 + 4f^2(M^2-1)\,\sigma^2(f,x)}\right\}$$

where $\sigma^2(f,x)$ represents all noise terms which do not vary with integration time, i.e., reset, clocking, amplifier, and system noise

For our model calculation with M = 2, f = 0.01, i - 4E03 electrons/sec, $\sigma^2(f,x)$ = 5300; τ = 1.5 seconds. Note that halving the dark current, i, doubles the integration time; this corresponds to T = -8 C. The signal to noise ratio

$$(eA/Mfi)$$

and the rms interpolation error is

$$\sigma(P) \sim \sqrt{C}\left(\frac{Mfi}{eA}\right)$$

For 1 %, 2 % interpolation error the required lens areas are 14.5 and 7.25 cm^2 respectively.

The lens focal length then determines the required NEA

$$\sigma(P)\,\Theta_p$$

where Θ_p is the angular subtense of 1 pixel. Note that this analysis indicates that eA/fi (cf. Fig.4.6) is the appropriate parameter for selecting CTD's. A tradeoff of power versus weight is required to assess the cost penalty incurred by cooling and by increasing the lens area. For fixed noise equivalent angle and focal length, the ratio of area to dark current is fixed so that the tradeoff is clear.

o Effect of Motion Blur

When orbital rates are large, we attempt to control the systematic errors by decreasing the update time and incur the penalty in noise equivalent angle for a given reading. Repeated measurement allows estimation of a straight line which describes stellar position either by extrapolation or interpolation and which corrects for the inherent lead or lag.

We examine two cases; large orbital rates of 240 arc sec/sec corresponding to a 90 minute low orbit and small rates of 15 arc sec/sec corresponding to a geosynchronous orbit. Table 4.2 indicates the performance of two different system designs operated with the update times that would be required for a stationary star field. Note that the star field is essentially stationary in geosynchronous orbit. The tolerable movement of 0.88 pixels requires a larger number of readings with a minimum measurement time for the low orbit case. This results in a large NEA for each measurement. However, the large number of measurements, N, reduces the effective value by the square root of N giving the indicated NEA. Note that this mode is effective whenever the clocking and amplifier noise dominate the CTD noise characteristic since in this case there is no difference between on chip/off chip summation. By further increasing the integration time and the number of readings the desired NEA can be achieved.

Table 4.2 Effect of Orbital Rate on the Update Time and the Noise Equivalent Angle

	Low Orbit	Geosynchronous Orbit
Star Magnitude	6	6
Period	90 min	24 hr
Orbital Rate	240 arc se/sec	15 arc sec/sec
Lens Aperture	1.4	1.4
Lens Focal Length	50/85	50/85
Pixel Angular Subtense (arc seconds)	91/53	91/53
Star Rate Pixel/sec	2.64/4.53	0.165/0.283
NEA No Movement	1 arc sec	1 arc sec
Integration Time	4 sec/0.3 sec	4 sec/0.3 sec
Star Movement Pixels in 1 Update	10.6/1.36	0.66/.085
Maximum Tolerable Movement (pixels)	0.88	0.88
Number of Reading/Meas	12/2	1/1

Table 4.2 Continued

Measurement Time (sec)	0.33/1.5	equivalent to
NEA/Measurement(arcsec)	5.8/1.9	stationary case
Effective NEA (arcsec)	1.67/1.34	
Integration Time (seconds) to achieve 1 arc sec	11.2/0.54	

5.0 OPTOMECHANICAL DESIGN

The optomechanical design addresses four areas: optical configurations, choice of lens, stray light suppression and an assessment of thermal load at the charge transfer device.

The discussion in the chapters above has assumed that multiple cameras are present. However the design choices were restricted to one CTD per camera since this describes the essence of the conceptual design choices. In this section we discuss the need for multiple CTD's per camera, and the number of cameras that are required.

Lens focal length determines both the field of view and the angular subtense of a single pixel given the mechanical dimensions of the array. There are a number of options available as summarized in Table 5.1. The ratio of dark current to lens area determines weight and power, so that decreased light levels (smaller lens area, or decreased throughput) can be compensated by cooling the array. Improvement of system performance by a factor of 7, allows stars weaker than magnitude 6 to be tracked; a narrower field of view can be used and higher resolution is obtained. However, the size of the star catalogue increases substantially.

Figure 5.1 illustrates the mounting of the lens, array and printed circuit board. This structure is chosen to minimize thermal conduction from the spacecraft heat sink.

5.1 Choice of Lens

In choosing suitable lenses, the following criterion were considered:

1) The blur size ofthe lens should be slightly bigger than the pixel size of the array.

2) Distortion of the far field must be characterized and correction made for angular distance of the image from the optical axis.

Table 5.1. Optical Design Choices

Design Option	Advantages	Disadvantages
Short focal length lens	Larger Field of View and short time period between empty starfields	Decreased angular resolution
Long focal length lens	Increased angular resolution	Small field of view and longer period between empty starfields
Increased lens Diameter	More light on the array	Greater weight
Greater numbers of pixels in focal plane	Larger field of view	Lens distortion more critical
Multiple arrays	Better than multiple cameras	Arrays are not buttable
Larger Array		Custom Design Yield
Multiple Cameras (minimum of 2)	High Light level	Weight Power
	Two orthogonal lines of sight define, pitch, roll & yaw	Mechanical alignment
Single Camera with Beamsplitter	Decreased weight and Power	Half the light level

Figure 5.1 LENS & CTD CONFIGURATION

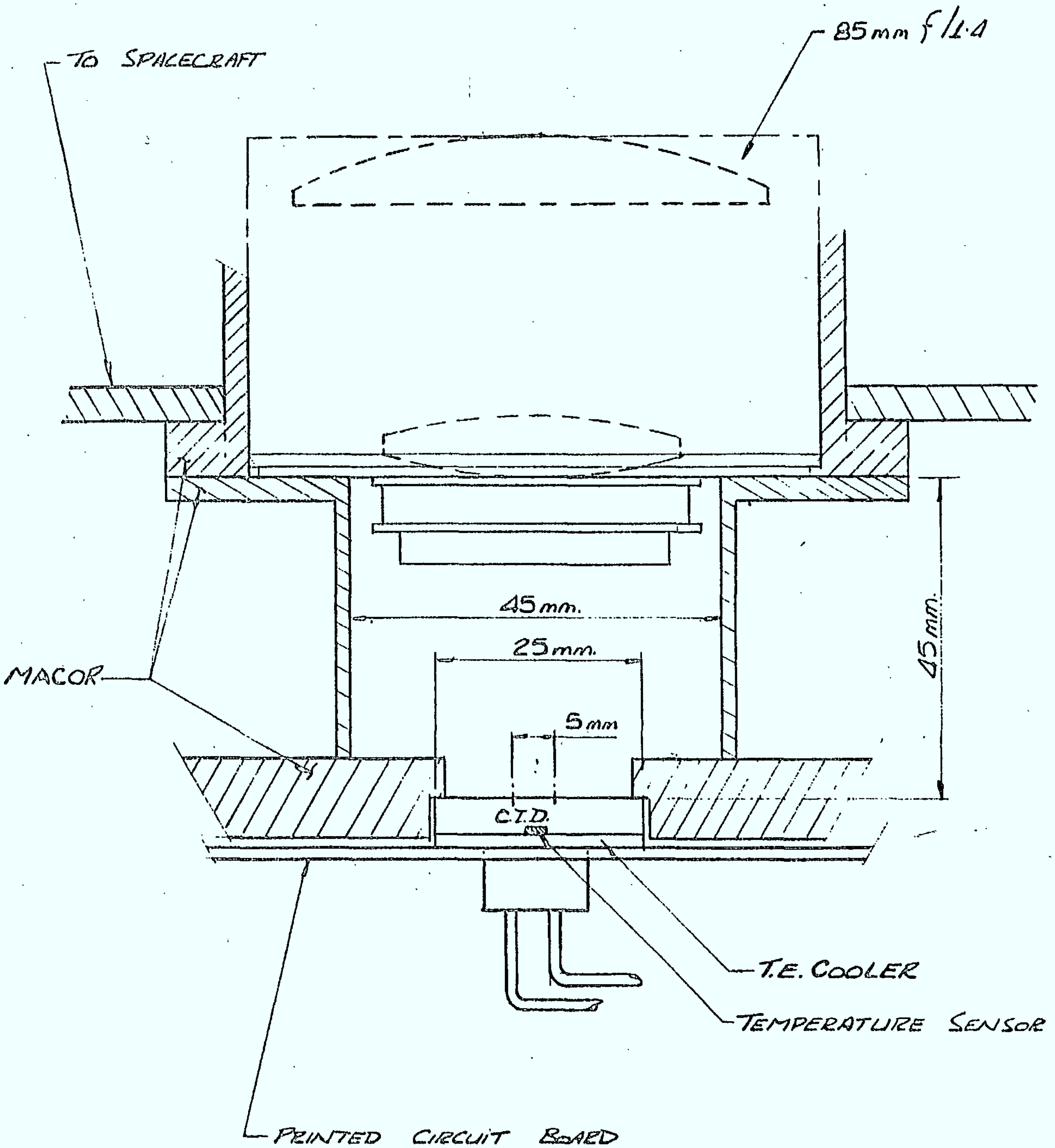

Lenses which satisfy the first criterion were selected and thereafter the distortion of that particular lens was investigated.

CTD's have pixels which range from 20 to 30 microns. Assuming that this optical point spread is Gaussian, then it gives the result that the modulation transfer function, M, is

$$M(f) = e^{-(2\pi f \sigma)^2/2}$$

where f is the spatial frequency and σ is the standard deviation corresponding to the Gaussian spot.

Since we have established that ratio of pixel size to standard deviation varies between 2 and 2.5, then σ should range from 8 to 15 microns. Figure 5.2 gives 3 different curves of M(f) against spatial frequency for different blur sizes. A comparison of these curves with the MTF information provided by lens manufacturers is also shown. The f/1.4 - 85mm was chosen as the trial candidate for further test since other lenses show much higher resolution. In fact, even the 85/1.4 lens requires defocussing. The distortion at the periphery of the CTD is estimated to be 1.5 microns so that further correction is necessary to reduce this value to 0.01 pixel.

Lens weight versus diameter of the lens is given in Figure 5.3 . It represents data for photographic objectives.

5.2 Stray Light Suppression

For most optical instruments off-axis stray light illumination introduces measurement error. This occurs even when the source is outside the field of view because of lens imperfections and reflections within the optics. In spacecraft, this off-axis illumination is usually from the sun, moon or sunlit earth. If the minimum allowable angle between the limb of these

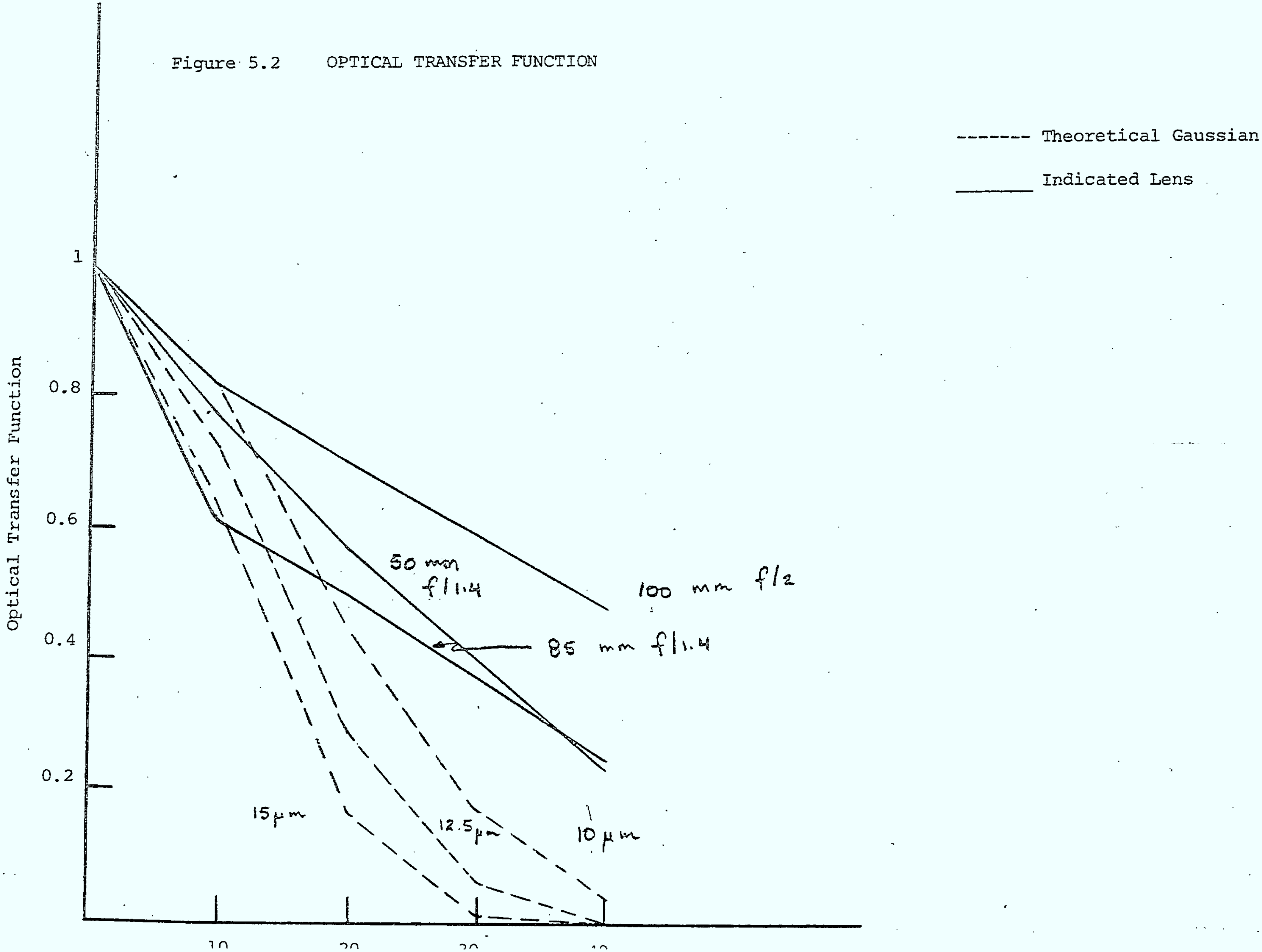

Figure 5.2 OPTICAL TRANSFER FUNCTION

Figure 5.3 LENS DIAMETER vs MASS FOR ALL LENSES

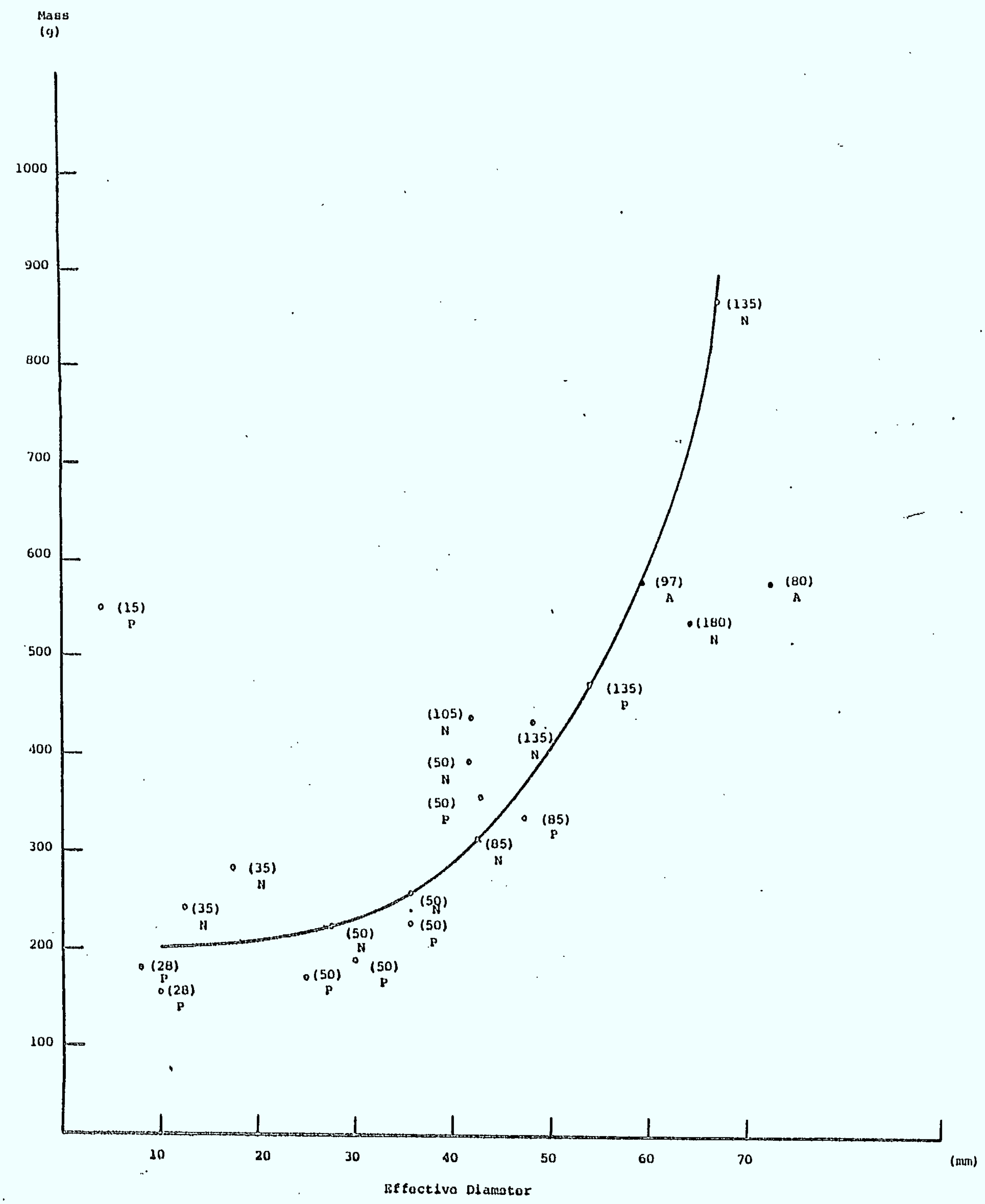

sources and the optical axis of the instrument is known, a two stage shade can be constructed to provide optimum rejection. In our case, since the sun is the brightest object only the stray light from the sun is considered. The design goal of a two stage shade is to eliminate first bounce reflections. Specular or diffuse light cannot impinge on the lens aperture until the critical angle is reached. Thus, the baffle edges in the outer stage are not "seen" by the optics. Given the optical aperture, field of view and sun angle, a minimum length shade can be designed. Figure 5.4 shows the length of the sunshade length for a 50 and 85mm f/1.4 lens. Large sun angles are ineffective since the sun is often within the star tracker field of view.

The placement of baffles in a sunshade is determined so that the camera lens is prevented from "seeing" any directly illuminated walls. The residual light arriving at the detector has therefore been attenuated by wall reflection, by diffraction and by reflection at a knife edge or by several of these attenuating processes. If the attenuation coefficients due to reflection and diffraction are known, for a given path down the baffle system the fraction of the incoming light reading the bottom of the baffle can be determined. The sum over all such paths is the attenuation given of the baffle system. Baffle attenuation has been estimated for a f/1.4 85mm lens and a 20 degrees sun angle sunshade design; the effective lens area is shown in Figure 5.5.

The intensity distribution after multiple reflections is assumed to be Lambertian, so that the array only collects light for a solid angle defined by its angular subtense. The total solid angle of the array is 8.3E-03 sr and this represents only 2.7E-03 collection efficiency. The overall attenuation is also shown in the figure.

The signal levels per pixel for the sun, moon and earth are given in Table 5.2 when these objects are imaged on the array. The effect of the baffle is shown in Table 5.3, As a function of angle of the object out of the field of view. There is the remote possibility that stellar images can be seen with the moon on the periphery of the field of view, since signals of 2E10 e/sec correspond to 2E4 full wells for a 1 sec integration time. If a CID is used blooming suppression, will minimize errors in the measurement.

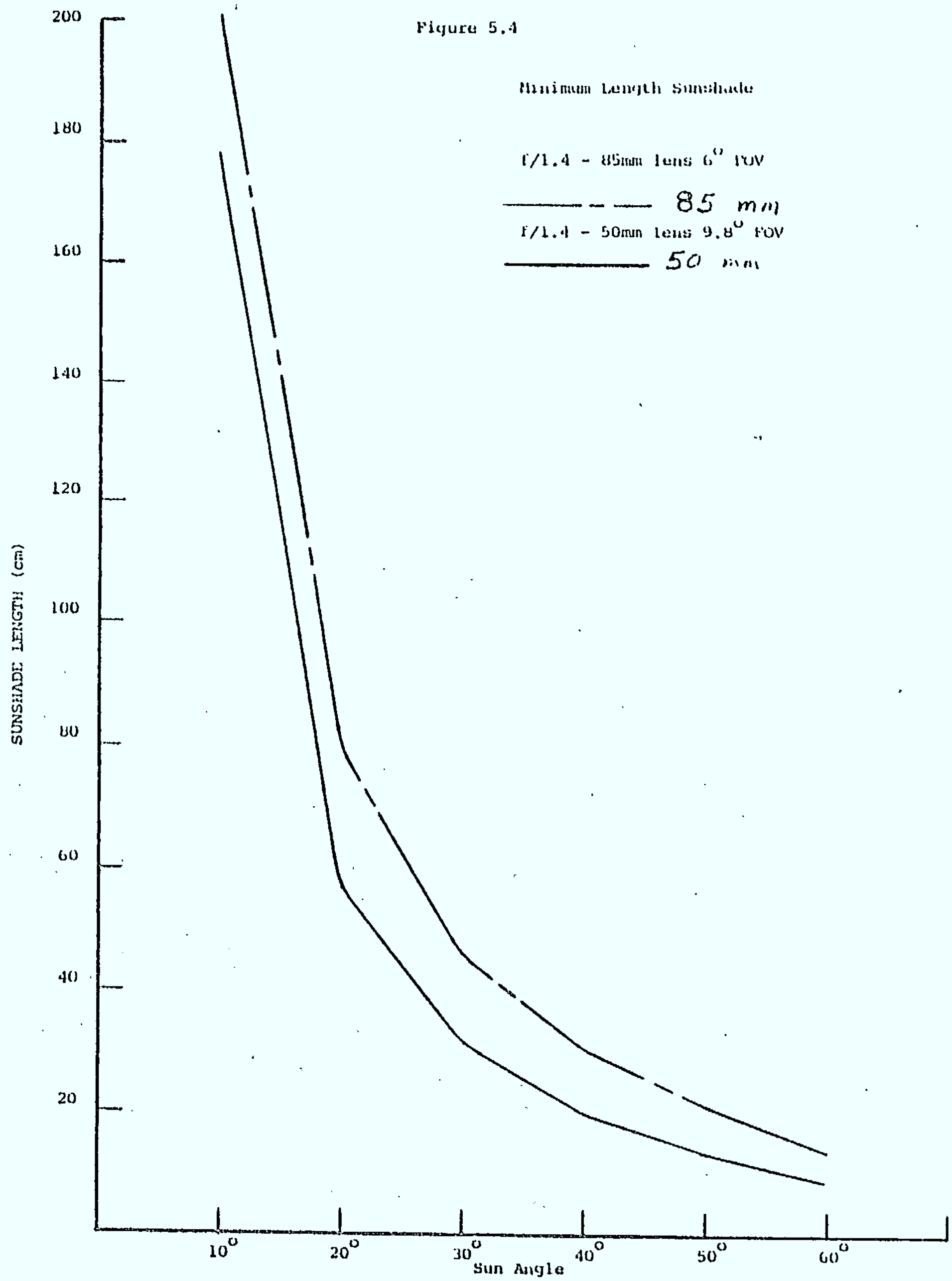
Figure 5.4
Minimum Length Sunshade
f/1.4 - 85mm lens 6° FOV
85 mm
f/1.4 - 50mm lens 9.8° FOV
50 mm
SUNSHADE LENGTH (cm)
200
180
160
140
120
100
80
60
40
20
10°
20°
30°
40°
50°
60°
Sun Angle

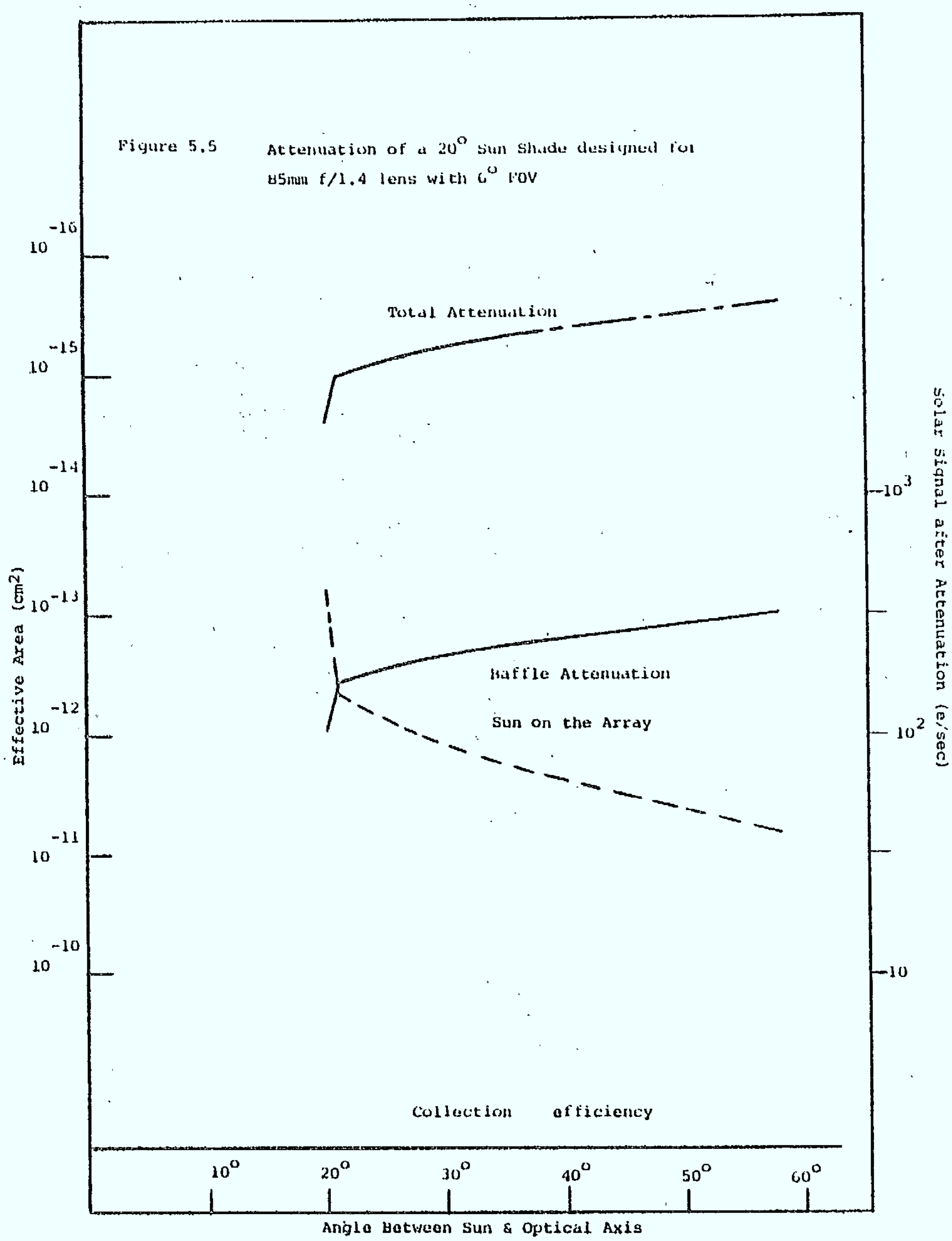
Figure 5.5 Attenuation of a 20° Sun Shade designed for
85mm f/1.4 lens with 6° FOV
Total Attenuation
Baffle Attenuation
Sun on the Array
Collection efficiency
Effective Area (cm2)
Solar Signal after Attenuation (e/sec)
10^-16
10^-15
10^-14
10^-13
10^-12
10^-11
10^-10
10^3
10^2
10
10°
20°
30°
40°
50°
60°
Angle Between Sun & Optical Axis

Table 5.2 Signal Levels of Various Sources on the Array f/1.4 Lens of Indicated Focal Length

Body	Angular Subtense at Satellite	Irradiance W/cm^2	Radiance $W/cm^2 sr$	Image Diameter (Pixels) Focal Length (mm) 50	85	Signal (e/sec) Focal Length (mm) 50	85
Sun	0.5	0.135	5.6×10^{2}	21	36	9.5×10^{14}	9.5×10^{14}
Earth	fills field of view	40×10^{-3}	12.7×10^{-3}	1	1	2.0×10^{10}	2.0×10^{10}
Moon	0.5	40×10^{-3}	12.7×10^{-3}	21	36	2.0×10^{10}	2.0×10^{10}
Star	negligible	1.3×10^{-15}		1	1	1.5×10^{4}	4.3×10^{4}

Etendue = 1.46×10^{-6} $cm^2 sr$

Table 5.3 Signals with the Baffle in Place as a Function of the Angle Between the Source and the Optical Axis

Angle	Effective Lens Area cm^2	Sun Power (W)	Sun Electron/sec	Earth Power (W)	Earth Electron/sec
20^{o}	$2.58x10^{-15}$	$3.48x10^{-16}$	$4.02x10^{2}$	$1.03x10^{-16}$	$1.19x10^{2}$
21^{o}	$9.87x10^{-16}$	$1.33x10^{-16}$	$1.54x10^{2}$	$3.95x10^{-17}$	45.7
27^{o}	$6.69x10^{-16}$	$9.03x10^{-17}$	$1.04x10^{2}$	$2.68x10^{-17}$	31
37^{o}	$4.56x10^{-16}$	$6.16x10^{-17}$	71.2	$1.82x10^{-17}$	21
58^{o}	$2.54x10^{-16}$	$3.43x10^{-17}$	39.7	$1.02x10^{-17}$	11.8

5.3 Thermal Considerations

o Temperature Control of the Image Sensor

To reduce temperature sensitive dark current and transistor noise it is important to control the temperature of the sensor. The easiest way to achieve this is by means of a thermoelectric cooler, which pumps heat from its cold side to its hot side. The direction of the heat transfer can be reversed by reversing the control current. Very careful consideration has to be given to the choice of the cooler. A multistage design is most likely because the efficiency of the cooler is highly dependent on the temperature difference it has to maintain and the amount of heat that has to be transferred. These factors will determine the amount of control power that is necessary.

The cooler controller consists of a power amplifier that will generate the necessary control power for the thermoelectric cooler. A temperature to voltage converter senses the temperature of the (preferably) image area or the surface between the sensor package and the thermoelectric cooler and the microprocessor will execute a control algorithm that stabilizes the image sensor temperature.

o Heat Load at the Charge Transfer Device

We have assumed that the CID might operate as low as -5 degrees C and that the sink varies in temperature from -40 to +65 degrees C. Table 5.4 summarizes the thermal transfer coefficients in vacuum and the heat load at temperature differences of 70C. We assume that the cooling is provided by a two stage Thermo Electric Cooler which is optimized. Optimization requires increasing the number of thermo-couples in the second stage to maximize the coefficient of performance and match the heat load. Figure 5.6 illustrates the estimated power consumption as the cold side temperature is varied. The calculation assumes a hot side temperature of 65C(338K). For comparison, the performance of a single stage cooler is also indicated. Values for two Borg-Warner coolers have been estimated as well. Unfortunately, data is not available to simulate the system performance at intermediate temperatures.

Table 5.4 Thermal Load

Part	Dimensions	Heat Transfer C/W	Power (W)
Ceramic Flange	4.5 cm ID 0.2 cm wall thickness 4.5 cm long X sectional area approx. 3 cm	114	0.60
30 Leads	Copper 2.5 x 0.08 x .013 cm	23	
	Constantin .014 dia. x 0.5 cm	476	
	Series combination	500	0.14
Scene			Negligible
Radiation	Emissivity 1 wall approx. 65 degrees C chip approx. - 5 degrees C		0.24
Power Dissipation			0.1

Figure 5.6 WORST CASE ESTIMATED ELECTRICAL POWER CONSUMPTION VERSUS DETECTOR TEMPERATURE

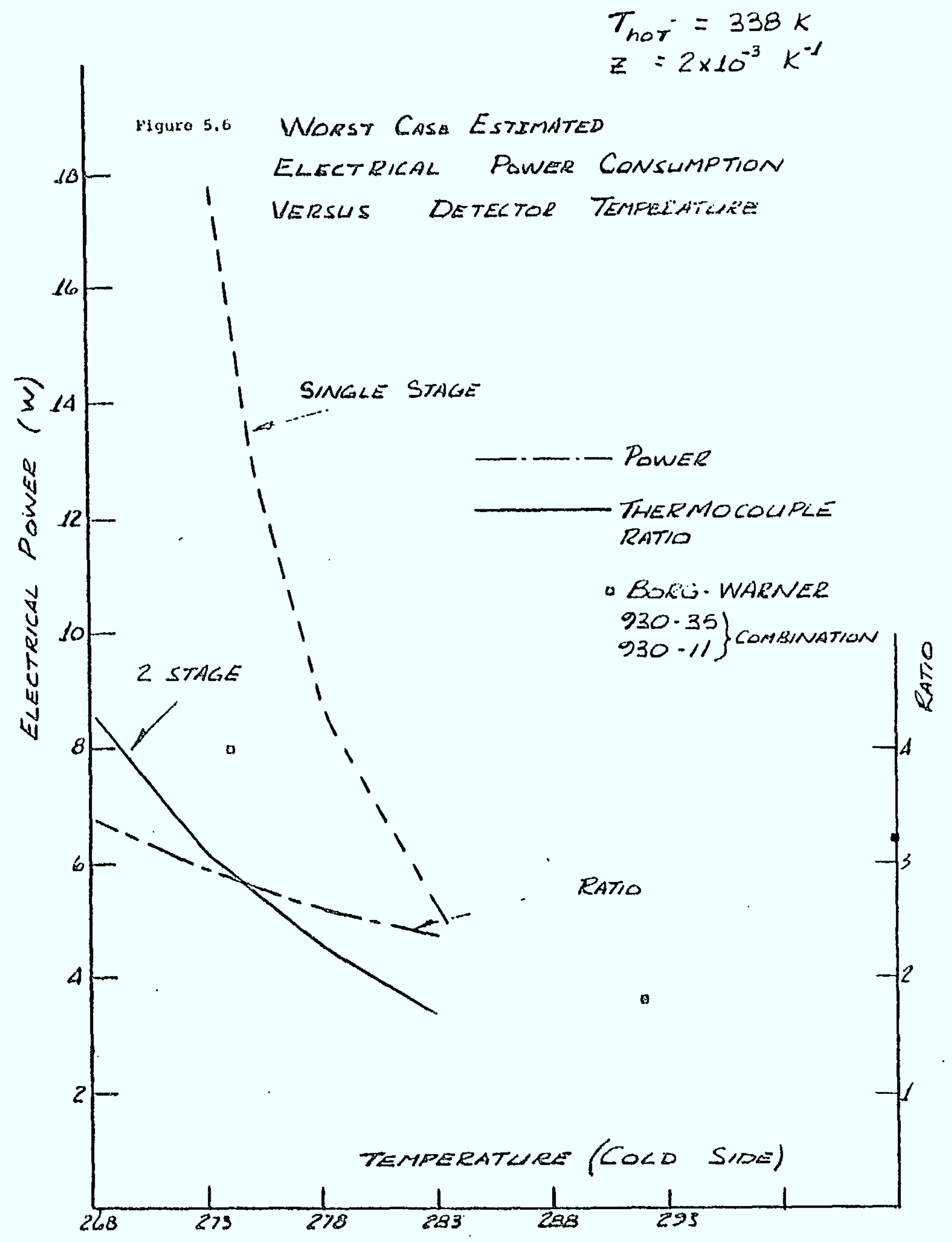

6.0 COMPUTATIONAL REQUIREMENTS

6.1 Pattern Recognition Algorithm

A rudimentary flow chart which combines the search and track algorithm with a view to minimizing the star catalogue search times has been produced (Figure 6.1). The principle feature of this approach is the concept of a link list connecting neighbouring stars. By numbering the links from a given star to its nearest neighbours and cross indexing this list with the star catalogue a considerable decrease in search time is achieved at the expense of some increased storage requirements.

o Creating the Star Catalogue Organization

The stars of the sky may be considered as points on a sphere. The locations of these points are known. Consider that these points are inside a balloon and are rigid with respect to their positions. Now shrink the balloon so that it tightly wraps these points. The result is a polyhedron which obeys Euler's theorem, namely,

$$V - E + F = 2$$

where Vis the number of vertices (stars), E is the number of edges (connections between stars), and F is the number of faces of the polyhedron.

In the worst case, each face is a triangle, then the relationship becomes

$$E = 3V - 6$$

From the point of view of storage, 3V - 6 links must be stored. However, since the representation must be star centred, that is, each star must "know" all of its connections, each link will be stored twice. The data structure that is necessary for this is a linked list, since no upper bound can be determined for the numbers of links per star. The data structure is illustrated in Figure 6.2.

The major problem remaining is the construction of this polyhedron or 'convex hull'. An algorithm for this exists in the literature and is due to Preparata and

Figure 6.1 Search and Track Algorithm

```
     /* note that comments are enclosed in
                  /* ... */ delimiters.   */

Repeat forever:

     Take star field snapshot:
     if guidance - error not set then
          /* only a position refinement is required*/

     /* the flag "guidance-error" can be set either by
          the inertial system on actual breakdown, or by
          the code below (signalling an ambiguous
          situation) */

          if startup cycle then

                  perform a linear search of star catalogue
                  for all stars in the field of view
                  predicted by the inertial
                  system's position information
          else
                  we have past position of specific stars in
                  image and in catalogue, as well as as
                  spacecraft speed and trajectory. Using this
                  information, we can predict new
                  field of view location.  For each star in
                  past FOV, search links for stars in new FOV
                  and thus create a list of stars expected in
                  FOV

          create image - specific search windows for each
          star in list; create coarse image from real
          image, threshold and use to remove noise in
          original. For each predicted search window,
          verify star presence and magnitude if all "stars"
          in original image are not accounted for then

                  if have 2 or more stars verified
                  then ignore the rest if have 1 or
                  fewer stars verified then
                  set guidance errors /* this
                  is just a flag for the next section

              if guidance error not set then

                  return true star positions from
                  catalogue to guidance system
```

Figure 6.1 Continued

```
if guidance - error then
      /* now a "blind search" is
      necessary particularly if the
      system has not been operating for
      some period of time */reset
      guidance-error; /* assume if true
      inertial system error, this will be
      set again */
if breakdown occurred less
than X time units ago then

      using most recent position and
      motion information create a large
      subsection of sky within which FOV
      must be present

else full sky search

create coarse image from real image, threshold
to remove noise in original, find candidate stars
in this image;

create a list of candidate stars
from catalogue using position
information, so that stars are in
subsection of sky to be searched;
find star candidates in image;
hypothesize matches
combinatorially; reduce number of
possible matches using expected
magnitudes; begin  matching with
least ambiguous star match*

      repeat until 2 or more stars of a
      pattern are matched or
      possibilities exhausted for each
      star in a link list; compute image
      separation distances

check image for stars at each
expected distance; goal is to find
star's neighbourhood pattern in
image if at least 2 connected stars
found then return true star
positions from catalogue to
guidance system /* If no proper
matches found, return to top of
loop, take a new picture and try
again */
```

N.B. Least ambiguous here means some combination of brightness and smallest number of hypothesized matches.

Figure 6.2 Link List Organization of the Star Catalogue

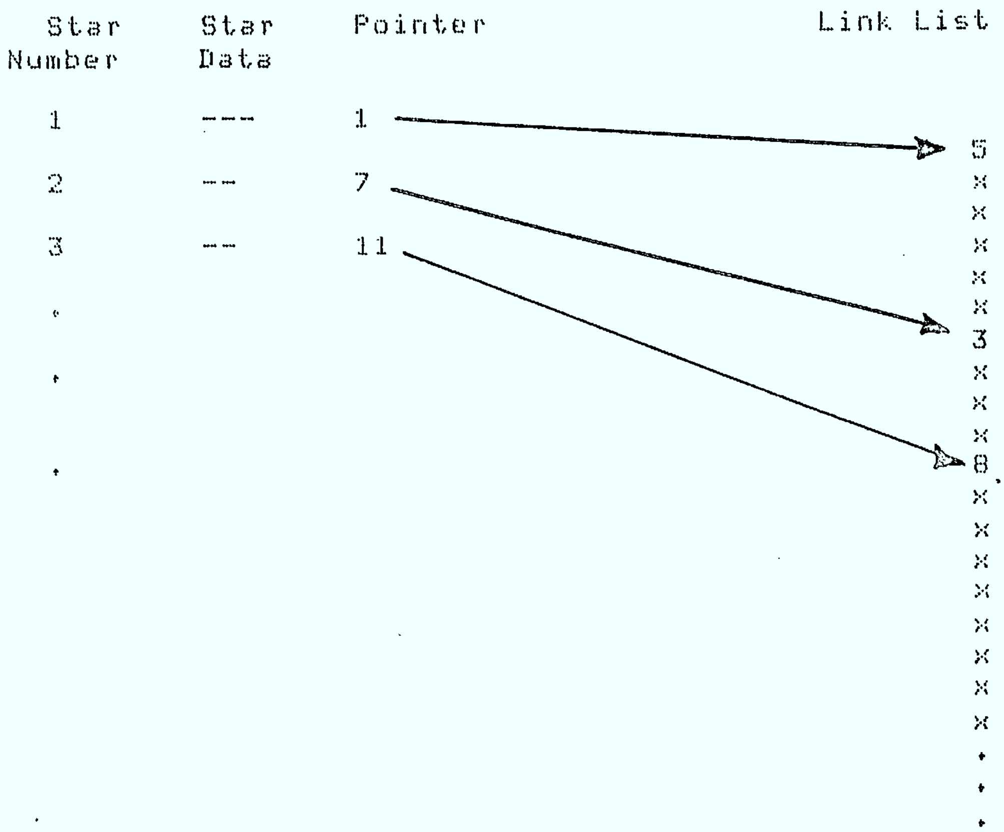

For each star there is a pointer to the list of edges. In the figure these are given the values 5,3,8. This indicates that stars 1,2,3 have 5,3,8 neighbours. The star number for each of these neighbors is indicated by the x's in the figure. For V stars in the catalogue there is a maximum of 3V-6 connections which must be stored bidirectionally. Each star also requires a pointer and an edge. In total, then, one requires 8V-6 integers. For maximum compression, this means that $\log_2 V$ bits are required for each integer.

Hong.(Ref.8). It requires O(n log(n)) steps, that is, the amount of computation units is

$$K * n * \log(n) + C$$

where K and C are constants and n is the number of vertices. The expense really doesn't matter since the algorithm will only be executed for star catalogue creation. Additional work on convex hulls was done by O'Rourke (references). There are some problems that were encountered by O'Rourke in the implementation of the 'merge' operation but they were overcome. There needs to be consideration of at least 1 special case, that of the merge of 1 point with a polyhedron. The solution creates links to all points on a closed surface.

The merge operation (i.e. the joining of previously constructed subsurfaces to create the final overall linked surface) is clearly where all the problems arise. A general solution is to create a band of jointed, flexible triangles that can wrap around the surfaces to be joined. The details of these operations plus some explicit geometrical examples can be found in the aforementioned references.

u Tradeoff: Space Vs. Time

The point of creating a star catalogue using this organization is to minimize the time required to search the catalogue for candidate stars for the next snapshot matching. As an example of the efficiency of the link list we assume the following upper limits; 5 stars in the current field of view, and rapid changes in this field of view so that say 45 new candidate stars must be considered for star catalog identification (i.e. the orbital rate is high so that the startracker image changes rapidly). With 40 new candidate stars (3*45-6) - (3*5-6) = 120 links are required to trace a path through the star catalogue. In contrast an unlinked catalogue of say 3000 stars would require 3000 checks for every star comparison made. Note also that this example is somewhat extreme; at realistic orbital rates and update times, the new field of view is displaced by less than one degree which means that there are typically no more than three new candidates for the link list organization.

6.2 Attitude Determination from Startracker Measurements

The nomenclature and geometrical transformations introduced in this section are similar to the "High Altitude Reference System Development Study" (Ref. 10) which was used as a basic reference.

To transform from stellar coordinates to the local startracker coordinates one utilizes four cartesian coordinate systems. Star positions are given in terms of right ascension (azimuth angle) and declination (elevation angle) in the inertial or celestial reference system whose z axis is aligned with the earth's axis of rotation. For a specific orbit orientation, vectors in this coordinate system are transformed to the orbital coordinate system shown in Figure 6.3

The orbit plane is completely specified in terms of its inclination i relative to the equatorial plane and the azimuthal angle, Ω, between the direction of a specific star (the first point of Aries) and the intersection point of the ascending orbit track with the equatorial plane (ascending node). For the sake of convenience when referring to body centred coordinates (see below) the axes are labelled so that the Z axis points radially inward along the direction of the ascending node axis, the Y axis is perpendicular to the orbit plane (opposite in direction to the obital angular momentum), and the X axis completes a right hand set. The body centred coordinate system (shown at the top of the orbital plane in Figure 6.3) is fixed on the orbiting satellite and oriented such that its nominal position is characterized by the Z (yaw) axis being perpendicular to the orbit plane (again opposite to the orbital angular momentum vector), and the X (roll) axis completes the right hand set (in the direction of motion for a circular orbit). Note that with this definition the nominal position of the body centred coordinate system is coincident with the orbital coordinate system at the time of ascending node crossing.

Figure 6.4 shows the geometrical relationship between the body centred coordinates and the sensor coordinate system whose Z axis is aligned with the optical axis of the system (or some appropriate

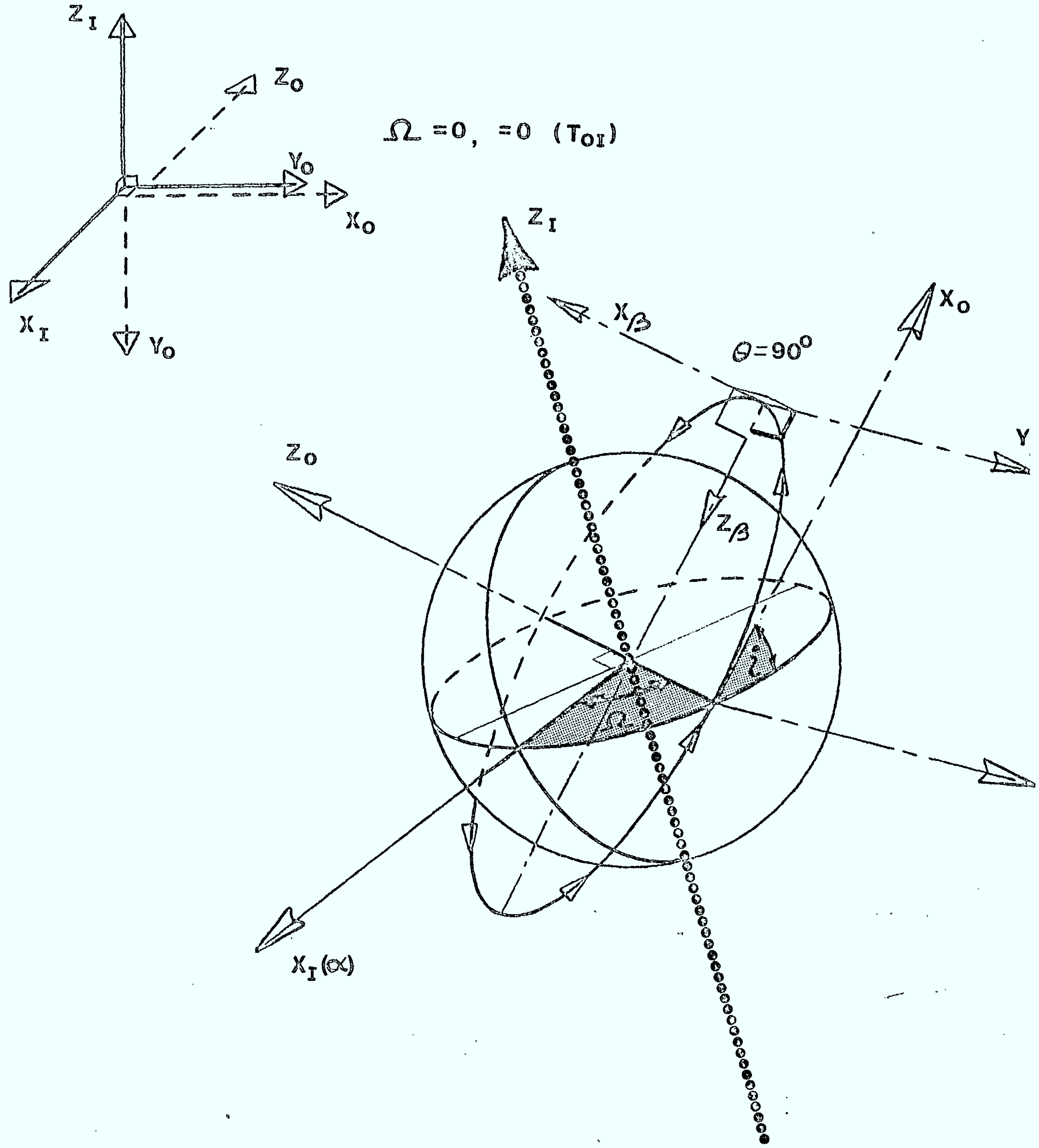

Figure 6.3 Inertial, Orbital and body centred co-ordinate systems (subscripts I, O, and B respectively)

Figure 6.4 The body centred and sensor co-ordinate system (subscripts B ans S respectively)

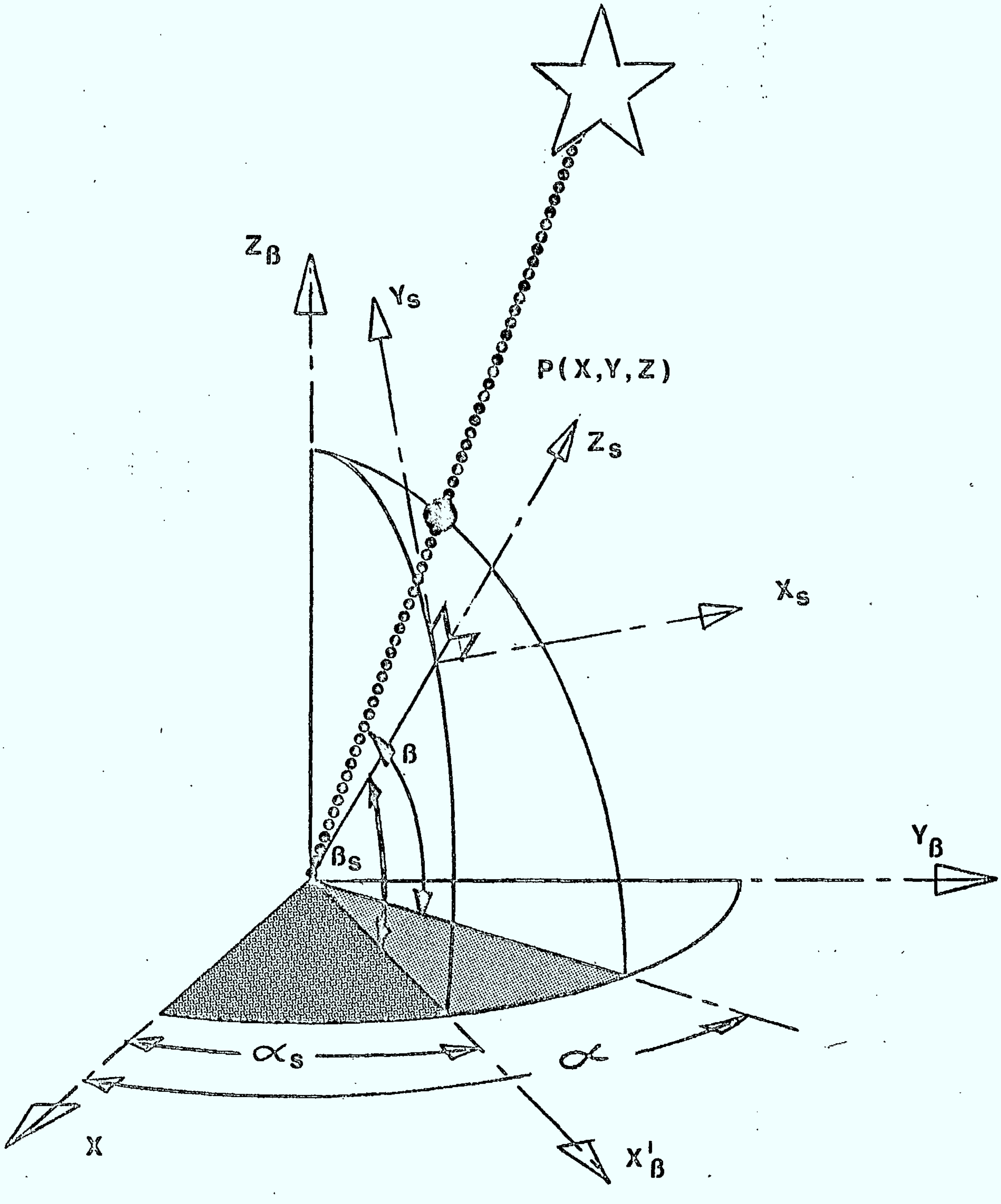

reference in the field of view of the instrument). Since the sensor measurements are essentially angular measurements relative to the optical axis and because these angles are small, displacements in the sensor (cartesian) coordinate system are approximated by angular quantities (see below).

All transformations between cartesian coordinate systems can be expressed as a product of three matrices representing three Euler rotations. This geometrical sequence can be envisaged in terms of three separate rotations of a rigid body about its x, y, and z coordinate axis.

In going from inertial to orbit coordinates a rotation about the Z_I axis (Ω) and subsequently the X_I axis (inclination angle i) yields the transformation

$$\begin{pmatrix} X_o \\ Y_o \\ Z_o \end{pmatrix} = \begin{pmatrix} \cos i & -\sin i & 0 \\ \sin i & \cos i & 0 \\ 0 & 0 & 1 \end{pmatrix} \begin{pmatrix} -\sin\Omega & \cos\Omega & 0 \\ 0 & 0 & -1 \\ -\cos\Omega & -\sin\Omega & 0 \end{pmatrix} \begin{pmatrix} X_I \\ Y_I \\ Z_I \end{pmatrix}$$

$$= \begin{pmatrix} -\cos i \cos\Omega & \cos i \cos\Omega & \sin i \\ -\sin i \sin\Omega & \sin i \cos\Omega & -\cos i \\ -\cos\Omega & -\sin\Omega & 0 \end{pmatrix} \begin{pmatrix} X_I \\ Y_I \\ Z_I \end{pmatrix}$$

$$= \tilde{T}_{OI} \begin{pmatrix} X_I \\ Y_I \\ Z_I \end{pmatrix} \qquad (6.1)$$

where the axis orientations prior to the rotations were X_o with Y_I, Y_o with $-Z_I$ and Z_o with $-X_I$ (chosen for convenience in reference to body centred-coordinates). A similar procedure for the transformatin from orbital to body centred coordinates yields

$$\tilde{T}_{BO} = \begin{pmatrix} \cos\psi\cos\theta + \sin\psi\sin\phi\sin\theta & \sin\psi\cos\phi & -\cos\psi\sin\theta + \sin\psi\sin\phi\cos\theta \\ -\sin\psi\cos\theta + \cos\psi\sin\phi\sin\theta & \cos\psi\cos\phi & \sin\psi\sin\theta + \cos\psi\sin\phi\cos\theta \\ \cos\phi\sin\theta & -\sin\phi & \cos\phi\cos\theta \end{pmatrix}$$

(6.2)

represents a rotation about the pitch (Y_o) axis, a rotation about the roll (X_o) axis and a rotation about the yaw (Z_o) axis. All rotations are in a direction such that a right hand thumb rule points in the direction of the associated axis. The nominal body centred orientation referred to above is taken here to mean the case $\psi = \phi = 0°$; and $\theta = -\Theta$ where Θ is the azimuth angle of the satellite position vector in the plane of the orbit (Θ = 90 degrees in Figure 6.4 above).

The last transformation from body centred to sensor coordinates is given by

$$\tilde{T}_{SB} = \begin{pmatrix} -\sin\alpha_s & \cos\alpha_s & 0 \\ -\cos\alpha_s \sin\beta_s & -\sin\alpha_s \sin\beta_s & \cos\beta_s \\ \cos\alpha_s \cos\beta_s & \sin\alpha_s & \sin\beta_s \end{pmatrix} \qquad (6.3)$$

where α_s, and β_s are the azimuth and elevation angle of the sensor optical axis (Figure 6.4).

Since these transformations must preserve vector lengths all transformation matrices $\tilde{T}$ are unitary or equivalently

$$\tilde{T}^{-1} = \tilde{T}^{t}$$

where the superscript t refers to the transpose of $\tilde{T}$.

The coordinate transformation of a fixed vector pointing in the direction of a given celestial reference point (star) is given by

$$\hat{\rho}_s = \tilde{T}_{SB}(\alpha_s, \beta_s)\, \tilde{T}_{BO}(\theta, \phi, \psi)\, \tilde{T}_{OI}(i, \Omega)\, \hat{\rho}(DEC, RA) \qquad (6.4a)$$

where $\hat{\rho}_s$ is in terms of the sensor coordinate system (the circumflex indicates a unit vector). $\hat{\rho}$ in terms of the inertial coordinate system is given by

$$\hat{\rho} = \cos RA \cos DEC\ \hat{i}_I + \sin RA \cos DEC\ \hat{j}_I + \sin DEC\ \hat{k}_I \qquad (6.4b)$$

RA represents the right ascension of the star (azimuthal angle), DEC the declination (elevation angle) and $\hat{i}_I$, $\hat{j}_I$, $\hat{k}_I$ are axial unit vectors in the directin of the X_I, Y_I, and Z_I axis respectively.

If α and β represent the azimuthal and elevation angles of the unit vector in the body centred coordinate system (see Figure 6.4), then the transformation to the sensor system is given by

$$\begin{pmatrix} X \\ Y \\ Z \end{pmatrix} = \tilde{T}_{S\theta} \begin{pmatrix} \cos\alpha \cos\beta \\ \sin\alpha \cos\beta \\ \sin\beta \end{pmatrix} \cong \begin{pmatrix} (\alpha - \alpha_s)\cos\beta \\ \beta - \beta_S \\ 1 \end{pmatrix} \qquad (6.5)$$

where only terms of first order relative to unity are retained. The X and Y components represent the angles actually measured by the startracker relative to the optical axis.

Given the X and Y components as input one can attempt to extract θ, ϕ, and ψ from equation 6.4. However it is clear that for small off axis angles the attitude is very insensitive to the Z component of $\hat{P}_S$. (i.e. Z ~ 1 for all measurements). Thus an inversion of (6.4) using data from a single star sensor can realistically provide only two pieces of information (two angles) regarding attitude. A good illustration of this concept is the case where the optical axis is close to say the pitch axis and a large change in pitch angle θ is required before the displacement of a star on the star sensor image plane is comparable to the displacements caused by relatively small changes in roll and yaw angle.

If estimates of attitude are available from the inertial navigation system or from previous star tracker measurements then the retrieval problem can be reduced to extracting changes in attitude given changes in stellar positions on the startracker image plane. Such an approach is advantageous in the sense that it eliminates the need to repeat redundant information concerning absolute angular position when angular changes from estimated positions are small. Accordingly for a star of given declination and right ascension we consider a nominal or reference position to be given by

$$\hat{P}_{s,r} = \tilde{T}_{S\theta}(\alpha_s, \beta_s)\, \tilde{T}_{\theta o}(\theta_r, \phi_r, \psi_r)\, \tilde{T}_{oI}(i, \Omega)\, \hat{p}(DEC, RA) \qquad (6.6)$$

and its actual position to be given by equation (6.4). Since the celestial coordinates and orbital parameters are the same for both star sensor vectors we can combine equations (6.4) and (6.6) to obtain the difference equation

$$\tilde{T}_{BO}^{t}(\theta,\phi,\psi)\,\tilde{T}_{SB}^{t}\,\hat{\rho}_s - \tilde{T}_{BO}^{t}(\theta_r,\phi_r,\psi_r)\,\tilde{T}_{SB}^{t}\,\hat{\rho}_{s,r} = 0 \qquad (6.7)$$

or $$\hat{\rho}_s = \tilde{T}_{SB}\,\tilde{T}_{BO}(\theta,\phi,\psi)\,\tilde{T}_{BO}^{t}(\theta_r,\phi_r,\psi_r)\,\tilde{T}_{SB}^{t}\,\hat{\rho}_{s,r}$$

where the unitary property of the transformation matrices has been utilized to replace inverses by their transpose. If the reference position is sufficiently close to the true positin we can make use of the small angle approxmations.

$$\cos\theta = \cos(\theta_r + \Delta\theta) \cong \cos\theta_r - \sin\theta_r\,\Delta\theta \qquad (6.8a)$$

$$\sin\theta \cong \sin\theta_r + \cos\theta_r\,\Delta\theta \qquad (6.8b)$$

with similar expressions for ϕ and ψ. Equation (6.7) is then reducable to the form

$$\hat{\rho}_s - \hat{\rho}_{s,r} = \tilde{T}_{SB}\{\tilde{A} + \tilde{B}\}\,\tilde{T}_{SB}^{t}\,\hat{\rho}_r \qquad (6.9)$$

where $\tilde{A}$ is an antisymmetric matrix which is first order in angular differences while $\tilde{B}$ is second order in angular differences. The pertinent components of $\tilde{A}$ and $\tilde{B}$ are

$$a_{12} = \Delta\psi - \sin\phi_r\,\Delta\theta \qquad (6.10)$$
$$a_{13} = \sin\psi_r \cdot \Delta\phi - \Delta\theta\cos\phi_r\cos\psi_r$$
$$a_{23} = \Delta\theta\cos\phi_r\sin\psi_r + \Delta\phi\cos\psi_r$$

$$b_{12} = -\Delta\theta\Delta\phi\,\sin^2\psi_r\cos\phi_r \qquad (6.11)$$
$$b_{13} = \Delta\theta\Delta\psi\cos\phi_r\sin\psi_r + \Delta\phi\Delta\psi\cos\psi_r$$
$$b_{21} = \Delta\theta\Delta\phi\cos^2\psi_r\cos\phi_r$$
$$b_{23} = \Delta\theta\Delta\psi\cos\phi_r\cos\psi_r - \Delta\phi\Delta\psi\sin\psi_r$$
$$b_{31} = -\Delta\theta\Delta\phi\cos\psi_r\sin\phi_r$$
$$b_{32} = \Delta\theta\Delta\phi\sin\psi_r\sin\phi_r$$
$$b_{ii} = 0$$

In deducing these expressions terms of third order were neglected in comparison to terms of first order. The reader will note that all components are independent of the pitch angle.

Consider as a relevant example a star sensor whose coordinate axes are aligned with the body centred axes (i.e. a camera pointing close to the direction of he orbit radial vector)($\alpha_s = -90°$, $\beta_s = +90°$). Letting $\phi_r = 0$, $\psi_r = 0$, ~~θ, = 0,~~ the X and Y components of equation 6.9 reduce to

$$X = X_r - \Delta\theta + (Y_r + \Delta\phi)\Delta\psi \qquad (6.12a)$$

$$Y = -(X_r - \Delta\theta) + Y_r + \Delta\phi \qquad (6.12b)$$

or

$$\Delta X = Y_r \Delta\psi - \Delta\theta + \Delta\phi\Delta\psi \qquad (6.13a)$$

$$\Delta Y = -X_r \Delta\psi + \Delta\phi + \Delta\theta\Delta\psi \qquad (6.13b)$$

where third order terms have been neglected relative to first order (note also that Z_r has been taken as unity as per equation 6.5). For small angles equations 6.12a and 6.12b represent a rotation by $\Delta\psi$ of a coordinate system $X_r - \Delta\theta$, $Y_r + \Delta\phi$ with respect to the star sensor system X, Y (Figure 6.5).

Accordingly the reverse transformation yields (ignoring 3rd order terms relative to first order)

$$-\Delta\theta = \Delta X + Y\Delta\psi \qquad (6.14a)$$

$$\Delta\phi = -\Delta\psi X + \Delta Y \qquad (6.14b)$$

Clearly the ΔX measurement is optimal for information regarding $\Delta\theta$, ΔY for information concerning $\Delta\phi$ while $\Delta\psi$ is only weakly related to the star sensor measurements through a second order product.

In the case of a pitch camera ($\alpha_s = 90^\circ$, $\beta_s = 0^\circ$) with the same values for the reference coordinates) equation 6.9 yields

$$\Delta X = Y_r \Delta\theta - \Delta\psi \qquad (6.15a)$$

$$\Delta Y = -X_r \Delta\theta - \Delta\phi \qquad (6.15b)$$

which is second order in terms containing $\Delta\theta$ while ΔX and ΔY are strongly correlated with $\Delta\psi$ and $\Delta\phi$ respectively.

We can thus infer from these examples that image data from two star sensors at right angles will provide sufficient information to accurately extract attitude change information. The inversions for $\Delta\theta$, $\Delta\phi$, and $\Delta\psi$ using the small angle approximation will be accurate (in comparison to more generalized inversion

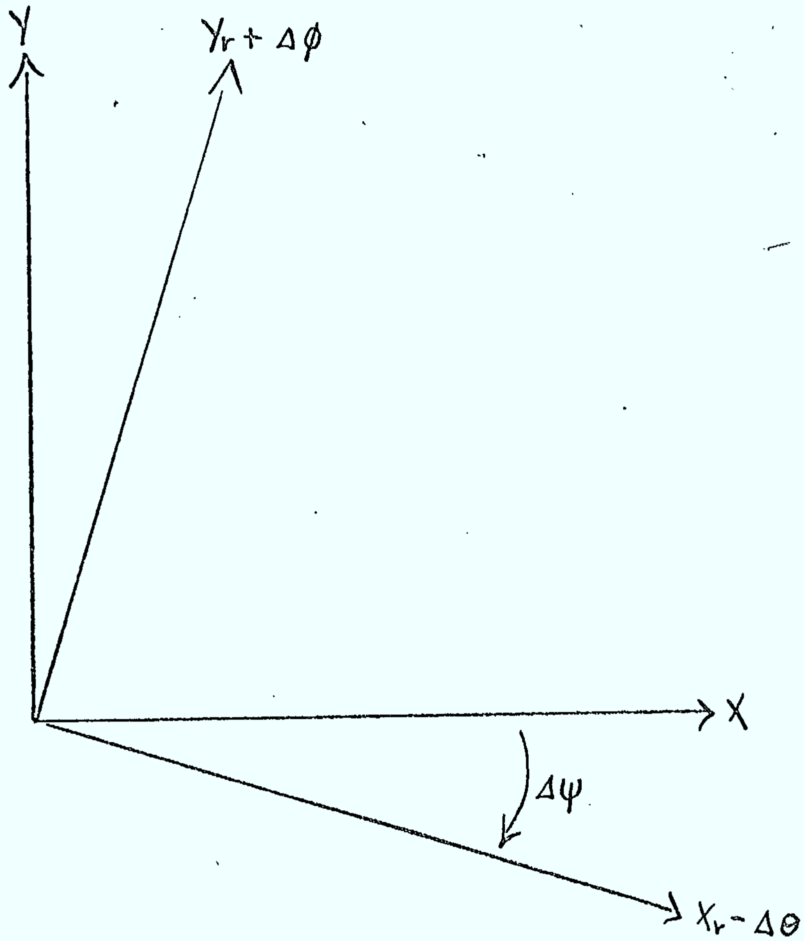

Figure 6.5 Geometrical Representation of Equation 6.13

techniques) to the order of unity compared to a second order angular term (about 1 arc sec for an angular range of 1 degree).

7.0 SYSTEM RECOMMENDATION

We recommend a system designed around an 85mm f/1.4 lens. The use of this lens allows the flexibility to see stars weaker than magnitude 6, as well as providing increased angular resolution. This lens also allows the use of a single camera with two fields of view.

The CID, ST-256, is the recommended device since it has demonstrated startracker performance. Although the JPL star tracker uses the RCA device we believe that the TI CCD would be superior; however, the TI device has not been used in a startracker.

Estimates of power are summarized according to subsystem in Table 7.1. A multiple output switch mode DC to DC converter can run at an approximate efficiency of 80%. Mass estimates are given in Table 7.2 and the system design performance is given in Table 7.3.

Because one camera can be obscured at any given time (e.g. by the sun), a redundant system should consist of two cameras and at least two attitude image monitors should be available. The tables indicate the power and weight constraints for both a redundant and non-redundant systems.

Table 7.1 Power Consumption for a Single Camera

PROGRAMMABLE IMAGE CONTROLLER		
Preamplifier	.10	W
Max Flat passband Elliptic Filter	.30	W
Correlated double sampler	.50	W
Analog to digital converter (12-bit, 25 microsec) (including multiplexer, instrumentation amplifier and sample and hold	.75	W
Drivers	.10	W
Timing Generator	.10	W
Synchronization Generator	.10	W
Microprocessor (NSC 800 CPU and serial and parallel interfaces	.80	
RAM (4k bytes at 1 MHz)	.10	W
PROM (6k bytes at 1 MHz)	.20	W
Video buffer (2k bytes at 1 MHz)	.05	W
TE cooler Controller	2.00	W
TE cooler	10.00	W
Shutter control	.10	W
TOTAL	15.50	W

ATTITUDE IMAGE MONITOR

Microprocessor (80C86 + Serial Interface)	1.50	W
RAM (8k bytes at 1 MHz)	.20	W
PROM (12k bytes a 1 MHz)	.40	W
Video Buffer (2k bytes at 1 MHz)	.05	W
Star Catalogue (70k bytes standby power)	.02	W
Camera timing generator	.10	W
Watchdog Timer	.10	W
TOTAL	2.37	W

Table 7.2 Mass Estimates for a Single Camera

Item	Mass (gms)
Lens (85 mm f/1.4)	600
Low thermal expansion Ceramic Structures	370
CTD	10
Two Stage Cooler	100
Printed Circuit Board	10
DC-DC Converter	700
Two Baffle	2500
Beamsplitter	100
Two Shutter	1200
Cooling Structures	500
	6000

Table 7.3 System Design Performance

Lens	85 mm f/1.4
CTD Readout	GE ST-256 Non-destructive double read
Operating Temperature	0 degrees C
Pixel Size	20 microns square
Angular Subtense of 1 pixel	48.5 arc sec.
Field of View	3.45 x 3.45 degrees
Interpolation Accuracy	approx. 1% 0.5 arc sec.
Random Error	less than 1% less than 0.5 arc sec.
Required Signal to noise ratio Magnitude 6 star	approx. 250
Maximum useful integration time	10 sec.
Design integration time (stationary star)	approx. 2 sec.
Minimum integration time Magnitude 2 star	10 ms
Maximum tolerable motion blur	43 arc sec/update

Table 7.3 (continued)

Maximum design update time	approx. 4 sec.
Stationary star	
Mass(including shutters and baffles)	
Non-Redundant	6 Kg
Fully Redundant	12 Kg
Power Dissipation	
Non-Redundant	23 W
Fully Redundant	46 W
Operating Temp.	-40 to + 65 C

The star catalogue is estimated to hold approximately 3000 magnitude 6 stars (70 kilobytes).

REFERENCES

1) A. Hirshfeld and R.W. Sinnot, Sky Catalogue 2000.

2) Pannekoek, Publ. Astrom. Institute of Amerstdam, 1924.

3) LHS Catalogue, W.J. Luyten, 1979, Univ. of Minnesota Press, (2nd edition).

4) E. Woolward and G. Clemence, Spherical Astronomy Academic Press, 1966.

5) T. Sterne, Introduction to Celestial Mechanics Inter-Science, 1960.

6) W.M. Kaula, Publ. No. 944, Inst. of Geophysics and Planetary Physics, UCLA, 1968.

7) L. Blitzer, J. Geophysical Research, 70, 3987, 1965.

8) F.P. Preparata and S.J. Hong, Communications of the ACM, 20, 87, 1977.

9) J. O'Rourke, Proceedings of the International Joint Conference on Artificial Intelligence, Vancouver, B.C., 1981.

10) High Altitude Attitude Reference System, AFAL-TR-1111, Vol. 2, Rockwell International Corp., 1970.